UNIVERSITY OF MANITOBA

Biomimetic Vibroprobes for Lunar and Terrestrial Subsurface Exploration

By

MAHDI ALAEI
VARNOSFADERANI

A thesis submitted to the Faculty of Graduate Studies of
The University of Manitoba
in fulfillment of the requirements for the degree of

Doctor of Philosophy

Department of Civil Engineering
University of Manitoba
Winnipeg, Manitoba, Canada

Declaration of Authorship

I, MAHDI ALAEI VARNOSFADERANI, declare that this thesis titled, "Biomimetic Vibroprobes for Lunar and Terrestrial Subsurface Exploration" and the work presented in it are my own. I confirm that:

- This work was done wholly or mainly while in candidature for a research degree at this University.
- Where any part of this thesis has previously been submitted for a degree or any other qualification at this University or any other institution, this has been clearly stated.
- Where I have consulted the published work of others, this is always clearly attributed.
- Where I have quoted from the work of others, the source is always given. With the exception of such quotations, this thesis is entirely my own work.
- I have acknowledged all main sources of help.
- Where the thesis is based on work done by myself jointly with others, I have made clear exactly what was done by others and what I have contributed myself.

Abstract

MAHDI ALAEI VARNOSFADERANI

Biomimetic Vibroprobes for Lunar and Terrestrial Subsurface Exploration

Space exploration presents challenges, particularly in adapting soil drilling tools for efficient subsurface investigation of the Moon and other extraterrestrial bodies. Traditional tools used on Earth are impractical due to payload restrictions in space missions. To address this issue, the development of light and compact probes is essential for overcoming payload barriers. This research focuses on the development of two concepts for subsurface investigation tools: 1) the utilization of subsonic projectile probes, which can be launched from a lunar orbiter or lander to the surface of the Moon, and 2) bio-inspired vibroprobes, which can be mounted on a lunar rover. As such, in the first part of this thesis, an analytical model is developed to predict the deceleration rate and final penetration depth of a rigid projectile probe under perpendicular subsonic impact. The analytical model, developed based on the spherical cavity expansion theory, considers plastic and elastic stress fields by incorporating the Mohr–Coulomb failure criterion. The proposed solutions in the subsonic range have been validated using field ground-based experimental data found in the literature. This validation confirms the model's reliability in estimating the dynamic motion of the penetrator and highlights its potential as a benchmark for more complex, sophisticated numerical calculations.

The second part of this thesis involves the development of a biomimetic vibro-based probe, which deploys energy-efficient high-power vibrations to enhance penetration into granular materials. This is carried out by drawing inspiration from observed bending vibrations in biological mechanisms such as snakes, horned lizards, and sandfish. First, the influence of vibration frequency, amplitude, and probe head on penetration resistance is assessed computationally using the discrete element method. The simulation outcomes suggest that high-frequency lateral vibrations hold promise in decreasing the required

overhead load for the penetration of probes into granular media. Then, the impact of lateral vibration is physically investigated by developing proof-of-concept bio-inspired vibroprobes in the laboratory. The probes are equipped with thin piezo patches to induce lateral vibration, manifesting as bending vibrations in the structure of the probes. Through experimental testing, the capability of the vibroprobes to reduce penetration force and enhance the penetration process into granular materials is assessed. The experimental results demonstrated a significant reduction in penetration force, reaching up to 42%, when employing bi-directional bending vibrations in the circular cross-section probe. This highlights the effectiveness of bending vibration in developing compact subsurface drilling tools.

These two concepts provide a promising strategy for overcoming soil drilling challenges in remote subsurface investigations.

Keywords:

Cavity expansion; Subsurface investigation; Projectile probe; Impact; Penetration; Lunar regolith; In-Situ Resource Utilization; Soil Drilling; Subsurface Investigation; Lateral Vibrations; Resonance Frequencies; penetration; Granular Material; Extraterrestrial Bodies.

Acknowledgements

I want to express my sincere thanks to my supervisors, Dr. Pooneh Maghoul and Dr. Nan Wu, for their consistent guidance, feedback, and support during my research. Their extensive knowledge of the subject and thoughtful feedback greatly contributed to the overall quality of this work. Their significant contributions were crucial in achieving a higher level of completion for this thesis. In addition to their technical assistance, I am grateful for their financial support, award nominations, reference letters, and valuable input on proposals for awards and grants, such as Mitac, NSERC lab2Market, and Research Manitoba, which have been instrumental in supporting my research endeavors.

In addition to my advisors, I owe a special debt of gratitude to the members of my Advisory Committee, namely Professor Igor Telichev and Hongwei Liu. Their constructive comments, encouragement, and professional guidance have been invaluable throughout this process. I would also like to express my heartfelt thanks to Dr. Kshama Roy, who served on my committee for the first three years. His valuable insights, compassionate assistance, and passionate involvement have been crucial, and I greatly appreciate his contributions.

I extend my sincere gratitude to my colleagues and friends at the Vibration and Acoustics Lab—Dr. Vahid Rabbani, Dr. Mohammad Hodaei, Ramin Hamzehei, Xinxiang Zong, Yu Xiao, and Mostafa Esmaeilzadeh. Special appreciation goes to Dr. Hodaei and Dr. Hongwei Liu for their invaluable assistance in formatting the thesis. I want to express my deep thanks once again to Dr. Vahid Rabbani and Dr. Miad Jarrahi for their support upon my arrival in Canada and during my studies.

I also want to acknowledge Ramin Hamzehei, a supportive friend who stood by me during challenging times while conducting experiments. A big thank you to Dana Amini and all former and current members of the Sustainable Infrastructure and Geomechanics Research Lab (SIGLab) for fostering an excellent collaborative environment within the team.

I appreciate the scholarships and awards I received during my Ph.D. program, such

as the Mathematics of Information Technology and Complex Systems (Mitacs) Accelerate program, University of Manitoba Graduate Fellowship (UMGF), Lab2Market NSERC program, and Research Manitoba.

Last but not least, I want to express heartfelt gratitude to my incredible wife and best friend, Neda, whose unwavering love and support have turned this academic journey into something truly extraordinary. Additionally, I extend warm thanks to my dear brother, Hamid, for his steadfast support during challenging times and to my parents for their unconditional love and encouragement.

Publication

The chapters of this thesis are reproduced, with modifications, from the following publications:

Chapter 2: Alaei Varnosfaderani, M., Maghoul, P., Wu, N. (2022). "Modelling the penetration of subsonic rigid projectile probes into granular materials using the cavity expansion theory." *Computers and Geotechnics*, 141, 104546.
https://doi.org/10.1016/j.compgeo.2021.104546

Chapter 3: Alaei Varnosfaderani, M., Maghoul, P., Wu, N. (2023). "Penetration analysis of high-frequency vibro-based probes in granular materials using the Discrete Element Method." *ASCE, Earth and Space 2022*, 176-183.
https://doi.org/10.1061/9780784484470.016

Chapter 4: Alaei Varnosfaderani, M., Maghoul, P., Wu, N. (2024). "The effect of bending vibration Modes on penetration of bio-inspired drilling tool in granular materials: an experimental study." *ASCE, Earth and Space 2024*.
https://doi.org/10.1061/9780784485736.033

Chapter 5: Alaei Varnosfaderani, M., Wu, N. and Maghoul, P. (2024). "Experimental investigations of the effects of bending vibrations resonance modes on penetration into granular materials." *Smart Materials and Structures*, 33(6), 065019.
https://doi.org/10.1088/1361-665X/ad4758

Code License: Alaei Varnosfaderani, Mahdi, Maghoul, Pooneh, & Wu, Nan. (2021). "PESCE: Penetration Estimation of subsonic rigid projectile probes into granular materials using the Spherical Cavity Expansion theory."
https://doi.org/10.5281/zenodo.5202859

Patents: "Vibratory burrowing probe for investigating subsurface regions of granular media in 1g and low/microgravity conditions." *US Provisional Patent No: 63332775*, Filed in April 2022.
Status: Filed and protected, status is pending

Contributions of Authors

Chapter 2: Alaei Varnosfaderani, M., Maghoul, P., Wu, N. (2022).

i. Alaei: project conceptualization, analytical derivation and validation, algorithm implementation, results interpretation, original drafting, and revising the paper.

ii. Maghoul: project conceptualization, criticized methodology, supervision of the numerical modeling, review, and edit.

iii. Wu: project conceptualization, criticized methodology, supervision of the numerical modeling, review, and edit.

Chapter 3: Alaei Varnosfaderani, M., Maghoul, P., Wu, N. (2023).

i. Alaei: project conceptualization, numerical simulations, results interpretation, original drafting, and revising the paper.

ii. Maghoul: project conceptualization, criticized methodology, review, and edit.

iii. Wu: project conceptualization, criticized methodology, review, and edit.

Chapter 4: Alaei Varnosfaderani, M., Maghoul, P., Wu, N. (2024).

i. Alaei: project conceptualization, designing the set-up and components, experimental tests, results interpretation, original drafting, and revising the papers.

ii. Maghoul: project conceptualization, criticized methodology, review, and edit.

iii. Wu: project conceptualization, criticized methodology, review, and edit.

Chapter 5: Alaei Varnosfaderani, M., Maghoul, P., Wu, N. (2024).

i. Alaei: project conceptualization, designing the set-up and components, experimental tests, results interpretation, original drafting, and revising the papers.

ii. Maghoul: project conceptualization, criticized methodology, review, and edit.

iii. Wu: project conceptualization, criticized methodology, review, and edit.

Contents

Declaration of Authorship ii

Abstract iii

Acknowledgements v

1 Introduction 1
- 1.1 The Big Picture . . . 1
- 1.2 Lunar Regolith . . . 2
- 1.3 Background . . . 4
  - 1.3.1 Early Planetary Soil Drilling . . . 4
  - 1.3.2 Upcoming Planetary Soil Drilling . . . 5
- 1.4 Advancements in Planetary Drilling Technology . . . 6
  - 1.4.1 High Speed Penetrometer . . . 7
  - 1.4.2 Bio-inspired Penetrometer . . . 8
  - 1.4.3 Mole Penetrometer . . . 14
  - 1.4.4 Ultrasonic/Sonic Drilling Rigs . . . 16
- 1.5 Gaps in knowledge . . . 20
- 1.6 Goals and objectives . . . 22
- 1.7 Validation . . . 23
- 1.8 Thesis structure . . . 24

2 Modelling the Penetration of Subsonic Rigid Projectile Probes into Granular Materials Using the Cavity Expansion Theory 26
- 2.1 Introduction . . . 27
- 2.2 Mathematical Developments . . . 32
  - 2.2.1 Cavity Expansion Model . . . 32
    - 2.2.1.1 Elastic Region . . . 34
    - 2.2.1.2 Plastic Region . . . 36
  - 2.2.2 Geometry of the Projectile Probe Nose . . . 43
- 2.3 Computational Procedure . . . 44
- 2.4 Results and Discussion . . . 45
  - 2.4.1 Radial stress in a three-layered soil medium . . . 45
  - 2.4.2 Radial stress in a volcanic ash . . . 49

2.4.3 LUNAR-A penetration in JSC-1 simulant . . . 52
2.5 Conclusions . . . 54

3 Penetration Analysis of High-Frequency Vibro-based Probes in Granular Media Using the Discrete Element Method 56
3.1 Introduction . . . 56
3.2 Model Descriptions . . . 60
3.3 Results and Discussion . . . 60
3.4 Conclusions . . . 64

4 The Effect of Bending Vibration Modes on Penetration of Bio-Inspired Drilling Tool in Granular Materials: An Experimental Study 66
4.1 Introduction . . . 67
4.2 Experimental Set-up . . . 69
4.3 Results and Discussions . . . 72
4.4 Conclusions . . . 76

5 Experimental Investigations of the Effects of Bending Vibrations Resonance Modes on Penetration into Granular Materials 77
5.1 Introduction . . . 78
5.2 Experimental Apparatus . . . 82
5.2.1 Main Components . . . 83
5.2.2 Rigs Configuration . . . 84
5.2.3 Signal Generator and Data Acquisition System . . . 86
5.2.4 Soil Properties . . . 87
5.3 Experimental Procedure and Results . . . 88
5.3.1 Non-Vibrating Probe Penetration Tests . . . 89
5.3.2 Modal Analysis . . . 90
5.3.3 Preliminary Penetration Tests . . . 93
5.3.4 Finite Element Analysis . . . 94
5.3.5 Main Penetration Tests . . . 96
5.3.5.1 Uni-direction Bending Vibration . . . 96
5.3.5.2 Bi-direction Bending Vibration . . . 100
5.4 Conclusions . . . 103

6 Conclusions, Future Directions, and Practical Applications 105
6.1 Conclusions . . . 105
6.2 Future Directions . . . 108
6.2.1 Sensitivity Analysis and Validation of the Analytical Model . . . 108
6.2.2 Systematic Experimental Planning and Calibration Approaches . . . 108
6.2.3 Repeatability and Statistical Validation . . . 109
6.2.4 Moon Environment Simulation Tests . . . 110
6.2.5 Enhanced Regolith Simulants . . . 110

6.2.6 Field Testing on Earth 110
6.2.7 Auger Drilling Techniques 110
6.2.8 Integration of Advanced Robotics and Sensing Technologies 111
6.3 Practical Applications 114

Bibliography **117**

A probe-coupling-actuators configuration used in Chapter 4 **130**

Appendix **130**

B probe-coupling-actuators configuration used in Chapter 5 **131**

List of Tables

2.1 Estimated penetration depth in a three-layered soil medium using different models. 48
2.2 Estimated penetration depth in antelope tuff using different models by neglecting friction. 51
2.3 Estimation of the penetration depth and time. 52
2.4 Expected LUNAR-A penetration in JSC-1 compacted simulant 53

3.1 DEM model parameters. 61

4.1 Penetration forces in one-directional excitation (hex probe) 75

5.1 Bending Mode Shapes Used for Penetration Tests 95
5.2 Comparison of Average Bending Frequencies 96
5.3 Penetration forces in one-directional excitation 99
5.4 Penetration forces in bi-directional excitation 103

List of Figures

1.1 Soil circulating system. Note: From (Nakatake, Konno, Mizushina, Yamada, Nakamura, and Kubota, 2016), p.409. © 2016, *IEEE.* 9
1.2 Conceptual design and drilling procedure of the ID. Note: From (Zhang, Li, Jiang, Ji, and Deng, 2019), p.839. © 2020, *IEEE.* 10
1.3 Wood wasp reciprocating piercing process. Note: From (Gao, Ellery, Jaddou, Vincent, and Eckersley, 2007), p.878. © 2007, *IEEE.* 12
1.4 The DROD design. Note: From (Pitcher, Alkalla, Pang, and Gao, 2020), p.16. CC-BY. 14
1.5 The USDC coring with minimum axial force and its schematic design. Note: From (Bao, Bar-Cohen, Chang, Dolgin, Sherrit, Pal, Du, and Peterson, 2003), p.1148. © 2003, *IEEE.* 17
1.6 Rapid burying of an adult sandfish with a sinusoidal lateral vibration. Note: From (Baumgartner, Fidler, Weth, Habbecke, Jakob, Butenweg, and Böhme, 2008), OPEN ACCESS. 22

2.1 Response regions. 33
2.2 Modification of η^* for partially locked hydrostat plastic region. 40
2.3 Nose geometry 43
2.4 Non-linear solution flowchart for linear pressure-volumetric strain assumption. 45
2.5 Radial stress at the cavity wall for a three-layered soil medium 47
2.6 Deceleration of the projectile 49
2.7 Radial stress at the cavity wall 50

3.1 Probe's dimensions and model in EDEM. 60
3.2 Total vertical force in different vibration amplitude at frequency 500 Hz. . . 61
3.3 Total vertical force in different frequencies with amplitude of 0.05 mm. . . . 62
3.4 Total vertical force in longitudinal and lateral vibration with amplitude of 0.05 mm. 63
3.5 Vibration impact at the frequency of 10500 Hz on the penetration rate for the conical nose ($\alpha = 10.4°$). 63
3.6 Vibration impact at the frequency of 10500 Hz on the penetration rate for ogival nose ($CRH = 3$). 64

4.1 Probe configuration . . . 70
4.2 Set-up configuration . . . 71
4.3 Directing a laser beam toward the probe tip . . . 72
4.4 Single-sided probe tip amplitude spectrum . . . 73
4.5 Penetration force with inefficient vibration modes . . . 74
4.6 Penetration tests with efficient modes . . . 76

5.1 Configuration of the penetration test set-up . . . 83
5.2 Probe Configuration . . . 85
5.3 Applying voltage and exciting bending vibrations in different directions . . . 86
5.4 Modal test setup . . . 87
5.5 particle size distribution . . . 87
5.6 Hands-Off Approach to Pouring Sand into the Pail . . . 88
5.7 Penetration Force of Non-Vibrating probe . . . 90
5.8 Single-sided amplitude spectrum of the input voltage . . . 90
5.9 Bending vibration and laser beam direction . . . 91
5.10 Single-sided Amplitude Spectrum of Probe Tip Velocity . . . 92
5.11 Single-sided Amplitude Spectrum of Probe Tip . . . 93
5.12 Penetration force with inefficient modes of vibration . . . 97
5.13 Penetration force at efficient bending Modes . . . 99
5.14 Trajectories of the probe tip's whirling motion for three effective resonance modes. . . . 100
5.15 Trajectories of the probe tip's chaotic motion. . . . 101
5.16 Penetration force with bi-directional modes of vibration . . . 102

6.1 Phases of Soil Penetration Enhanced by Bending Resonance Vibrations . . . 112
6.2 Illustration of the drilling rig's instrumentation. . . . 114

A.1 Hex probe detail drawing (all dimensions are in mm) . . . 130

B.1 Circular probe detail drawing (all dimensions are in mm) . . . 131

List of Abbreviations

AC	**A**lternating **C**urrent
ALSD	**A**pollo **L**unar **S**urface **D**rill
AVG	**A**verage
BNSC	**B**ritish **N**ational **S**pace **C**entre
BPM	**B**lows **P**er **M**inute
CRD	**C**hip **R**emoval **D**evice
DA	**D**ischarging **A**nchor
DC	**D**irect **C**urrent
DCMM	**D**ual **C**omplex **M**otion **M**echanism
DEM	**D**iscrete **E**lement **M**ethod
DLR	**D**eutsches **Z**entrum für **L**uft- und **R**aumfahrt (German Aerospace Center)
DM	**D**ischarging **M**odule
DRD	**D**ual-**R**eciprocating **D**rilling method
DROD	**D**ual **R**eciprocation **O**scillation **D**rill
EA	**E**xcavation **A**nchor
EM	**E**xcavation **M**odule
ESA	**E**uropean **S**pace **A**gency
FE	**F**inite **E**lement
FEA	**F**inite **E**lement **A**nalysis
FFT	**F**ast **F**ourier **T**ransform
HP^3	**H**eat **F**low and **P**hysical **P**roperties **P**ackage
IBR	**I**nchworm-like **B**urrowing **R**obot
ID	**I**nchworm **D**rill
InSight	**I**nterior **E**xploration using **S**eismic **I**nvestigations, **G**eodesy, and **H**eat **T**ransport
ISRU	**I**n-situ **R**esource **U**tilization
MMUM	**M**oon **M**ars **U**nderground **M**ole
MSM	**M**ole with **S**ampling **M**echanism
NASA	**N**ational **A**eronautics and **S**pace **A**dministration
PARoD	**P**ercussive **A**ugmenter of **R**otary **D**rills
PESCE	**P**enetration **E**stimation using the **S**pherical **C**avity **E**xpansion theory
PLUTO	**P**Lanetary **U**nderground **TO**ol
PM	**P**ropulsion **M**odule

PRIME-1	**P**olar **R**esources **I**ce **M**ining **E**xperiment-**1**
RK4	**R**unge–**K**utta method (**4**th order)
RPUD	**R**otary-**P**ercussive **U**ltrasonic **D**rill
SCADAS	**S**ignal **C**onditioning and **D**ata **A**cquisition **S**ystem
sec	**sec**onds
SPaRH	**S**ingle **P**iezo-**A**ctuator **R**otary-**H**ammering
TEM-P	**T**hermal **E**xcitation **M**easurement-**P**assive
TRIDENT	**T**he **R**egolith and **I**ce **D**rill for **E**xploring **N**ew
TRL	**T**echnology **R**eadiness **L**evel
USDC	**U**ltrasonic/**S**onic **D**riller/**C**orer
VIPER	**V**olatiles **I**nvestigating **P**olar **E**xploration **R**over
VNIITransmash	**V**ehicle **N**ational **I**nstitute for **T**ransportation **M**obile **E**ngineering (Russian)

List of Symbols

D_r	Relative density
e	Void ratio
σ_I	Major principal stresses
σ_{III}	Minor principal stresses
C_{oh}	Cohesion
ϕ_f	Angle of internal friction
V_{p_0}	Initial projectile velocity
V_p	Projectile velocity
c_p	The elastic-plastic interface speed
t	Time
r	Radial spherical coordinate
c_e	The elastic wave speed
ν	Poisson's ratio
ρ_0	Initial density of the granular medium
E	Young's modulus
v	Radial particle velocity
σ_r	Radial stress in spherical coordinates
σ_θ	Azimuthal stress component in spherical coordinates
$\vec{V}$	Particle velocity field
p	Hydrostatic pressure
Y	$\sigma_r - \sigma_\theta$
ϵ_r	Radial strain component
ϵ_θ	Azimuthal strain component
ϵ_ϕ	Angular strain component
u_r	Radial displacement
ζ	Dimensionless parameter ($r/c_p t$)
$\tilde{u}(\zeta)$	Dimensionless variable ($u_r/c_p t$)
$S(\zeta)$	Dimensionless radial stress
η^*	Locked volumetric strain
ρ^*	Locked density
U	Dimensionless radial particle velocity variable
β	Dimensionless parameter (c_p/α)

α	Sound speed ($\sqrt{E/\rho_0}$)
V_c	Uniform velocity for cavity development
ψ	Non-dimensional cavity wall speed
K	Bulk modulus
κ	Constant ($0 \leq \kappa \leq 0.5$)
CRH	Caliber-Radius-Head
ϕ	Probe nose angle parameter
γ	Cone angle of the probe
F_p	Retarding axial force
a_p	Acceleration of probe
M	Mass of probe
z	Penetration depth
V_z	Penetration rate
F	Penetration force
f	Excitation frequency (Hz)
ω	Excitation frequency (rad/sec)
A	Amplitude of Vibration
g	Gravity
R	Percentage of maximum force reduction
t_r	Release time in seconds

Chapter 1

Introduction

1.1 The Big Picture

Numerous space agencies and private companies are actively planning missions to explore the Moon and Mars. NASA's Artemis program, for example, aims to establish sustainable lunar exploration by 2028. This involves setting up a human base camp, developing technologies for using local resources (In-situ Resource Utilization (ISRU)), and addressing challenges related to energy, water, oxygen, and material resources (Ellery, 2020). The ultimate goal is to prepare for crewed missions to Mars in the 2030s (NASA, 2020).

To plan future construction and mining activities on the Moon, Mars, and beyond, it's essential to comprehend the conditions beneath their surfaces. This understanding is critical for designing structures that can support human settlement on celestial bodies. A crucial aspect of this design process is studying the behavior of the soil beneath the surface. This includes collecting information about subsurface conditions, evaluating soil properties for foundation design, categorizing soil types, identifying geotechnical risks, and evaluating environmental impact.

Moreover, establishing permanent human colonies on the Moon requires identifying and using local resources to reduce dependence on Earth-based resources for financial feasibility. ISRU technologies play a crucial role in this mission by extracting and processing local materials into essential resources such as fuel, water, metals, and oxygen. This intentional reduction in reliance on Earth-based resources is essential for sustainable and self-sufficient exploration beyond our planet.

To accomplish the aforementioned objectives, it is crucial to employ advanced soil drilling techniques capable of accessing various soil layers and supporting mining operations. These drilling methods must be customized to meet the specific demands and challenges of space exploration. One significant challenge involves the constraints on mass and volume transportation (payload) restrictions in space missions. For example, the Mars 2020 rover, weighing 2260 pounds, incurred a substantial cost of $243 million (Wikipedia contributors, 2022). To put this into perspective, traditional geological soil drilling rigs used on Earth—essential for penetrating soil and assessing its properties—are comparable to or even larger in size than the Mars 2020 rover. Consequently, the exorbitant cost of

launching heavy rigs like conventional subsurface investigation tools poses a significant barrier to their application in space missions.

Moreover, performing soil drilling on dusty planetary bodies or the lunar surface introduces additional challenges attributed to the low (or micro-) gravity conditions prevailing in these environments. On Earth, the weight of a drilling rig's structure plays an important role in stabilizing the rig and providing necessary support as the drill bit penetrates the soil. However, in low-gravity conditions, the diminished weight of the rig's structure impedes its capacity to effectively support the rig. The deficiency in stabilizing force elevates the risk of the rig wobbling or tipping over, particularly when drilling in hard soil. This instability poses a significant risk and threat to the mission's success.

Furthermore, both the Moon and Mars undergo significant temperature changes between day and night, with Mars experiencing fluctuations of up to approximately 100°C (Munguira, Hueso, Sánchez-Lavega, Torre-Juarez, Martínez, Newman, Sebastian, Lepinette, Vicente-Retortillo, Chide, et al., 2023), and the Moon exhibiting even more substantial temperature variations. For instance, during Moon daytime, temperatures reach radiative equilibrium, ranging from about 387–397 K at the equator, and then drop to around 95 K just before sunrise (Williams, Paige, Greenhagen, and Sefton-Nash, 2017). These notable temperature fluctuations present substantial hurdles in designing drilling rigs intended to penetrate the soil on these celestial bodies. While hydraulic systems are commonly used on Earth for such purposes, they prove ineffective or nonfunctional in the face of these extreme temperature fluctuations and insignificant atmospheric pressure. For instance, the susceptibility of rubber seals and gaskets to brittleness in low temperatures, combined with the failure of sealing materials in high temperatures, renders hydraulic systems ineffective. Additionally, the hydraulic fluid itself encounters temperature-related challenges, thickening in cold conditions and thinning out in high temperatures, compromising overall efficiency. It is crucial to address these challenges in the design of drilling equipment for lunar and Martian exploration for the success of future missions.

Therefore, it is essential to develop innovative soil drilling technologies to advance our capabilities in space exploration. We require tools that are not only compact and highly maneuverable but also capable of functioning effectively in the challenging and harsh conditions of extraterrestrial soil. This endeavor is crucial for pushing the boundaries of our space exploration capabilities on the Moon and beyond.

1.2 Lunar Regolith

The surface of the Moon is covered with fine unconsolidated material called regolith. Lunar regoliths in mare areas are typically estimated to be 4–5 meters thick, while they can reach 10–15 meters thick in highland regions (Heiken, Vaniman, and French, 1991). The regolith particles are primarily formed by the repeated shower of meteorites and micrometeorites over millions of years, which resulted in a heterogeneous and well-graded (poorly-sorted) soil where its particle size distribution is wide, with a high fine-grained (dust) content (Heiken, Vaniman, and French, 1991). This constant bombardment of the

surface by micrometeoroids creates tiny broken dust and particles with very sharp and jagged edges that remain abrasive due to lack of weathering (Kobrick, 2010). As a result of its sharp jagged shape, the soil particles become more interlocked, which affects its bulk modulus and increases cohesion (Gale, Buettner, Mehta, Liever, and Curtis, 2017; Benaroya, 2017).

Lunar soil is composed of very fine-grained clastic grey particles that result from the mechanical breakdown of basaltic and anorthositic rock. The median particle size for the analyzed samples is reported to be from 40 to 130 μm, with an average of 70 μm. Approximately 10% to 20% of the soil on the surface is finer than 20 μm, which easily sticks electrostatically to everything nearby (Heiken, Vaniman, and French, 1991). At lunar sunrise and sunset, the high photo-induced variation in electrical conductivity will charge surface soil particles to the point where they can levitate and move. This fine-grained sticky abrasive lunar dust is a big concern for the safety of astronauts and the operation of equipment (Kobrick, 2010; Benaroya, 2017). Such charged soils and dusty particles may quickly cover surfaces, decrease the equipment's visibility and functionality and create challenges for lunar investigation during the lunar night. Furthermore, this highly abrasive regolith on the Moon contains nanophase pieces of iron, or pure iron, which can easily be affected by a magnetic field (Curious Droid, 2017). Besides, low gravity and extreme temperature fluctuation make equipment operation more problematic on the Moon's surface. On the other hand, previous studies on the returned lunar regolith showed that the lunar regolith, collected from very limited areas, is not a homogeneous material considering its bearing resistance and relative density. Relative density quantifies the compactness of granular materials and is expressed as:

$$D_r = \frac{e_{\max} - e}{e_{\max} - e_{\min}} \times 100(\%)$$

where $e_{\max}$ is the void ratio in the loosest state, $e_{\min}$ is the void ratio in the densest state, and e is the current void ratio. The void ratio represents the volume of voids relative to the volume of solid particles within the material. A relative density of 0% corresponds to the loosest particle packing, while 100% corresponds to the densest packing. Granular materials with relative densities between 0–15% are classified as very loose, 15–35% as loose, 35–65% as medium-dense, 65–85% as dense, and 85–100% as very dense (Holtz, Kovacs, and Sheahan, 1981). As relative density increases, particle interlocking, friction, and resistance to excavation also rise. Lunar regolith exhibits low to medium relative density in shallow layers while it reaches a high relative density just 20 cm below the surface. As a result, at shallow depths (<30 cm), excavation or displacement of regolith is not problematic; however, by increasing the depth, the interlocking of particles, friction, and cohesion increases. Therefore, digging and penetration become more challenging, as indicated during the Apollo 15 mission when Astronaut Irwin reached a hard layer at 30–35 cm (Colwell, Batiste, Horányi, Robertson, and Sture, 2007).

1.3 Background

In the following, we first review the previous successful planetary soil drilling missions, and then review the most promising upcoming ones.

1.3.1 Early Planetary Soil Drilling

The Apollo 15–17 missions (1970–1972) stand out as the initial phase in lunar subsurface exploration, introducing the groundbreaking Apollo Lunar Surface Drill (ALSD). These missions utilized a rotary-percussive drill named ALSD, which remains unparalleled for its extraterrestrial drilling depth of 3.05 meters (Zhang, Zhang, Wei, Liu, Wang, Yuan, Pang, Guan, Hou, and Xu, 2022). During each Apollo 15-17 mission, three holes were drilled, two for heat flow probes and one for a regolith core. During the Apollo 15 mission, operational challenges emerged due to the absence of auger flutes for hole cleaning and the lack of a mechanism to remove the drill, resulting in operator arm strain. Subsequent Apollo 16 and 17 missions addressed these issues by redesigning the stems to include a continuous auger for clearing dense soil. Additionally, a solution was found in later missions by integrating a jack mechanism, effectively overcoming the drill extraction challenge (Zacny, 2012). The maximum depth of the drill stem was 236 cm, 224 cm, and 305 cm, and the total return sample was 1343.5, 1007.6, and 1772.5 grams in Apollo 15, 16, and 17, respectively (Carrier III, 1974).

On the other hand, the Soviet Union utilized automated probes for the retrieval of lunar regolith in the Luna 16, 20, and 24 missions conducted in 1970, 1972, and 1976, respectively. These missions successfully drilled into the lunar subsurface, retrieved regolith cores, and returned them to Earth. Luna 16 and 20 landers, which landed on a lunar night and a lunar day respectively, utilized a similar shallow rotary drill capable of reaching a depth of 35 cm, with an interior hard core tube (Slyuta, 2021). However, Luna 20 faced challenges when its drill encountered a hard rock, leading to termination at a depth of around 25 cm (Zhang, Zhang, Wei, Liu, Wang, Yuan, Pang, Guan, Hou, and Xu, 2022). Luna 16's drill reached 35 cm, collecting 101 grams of material sealed and returned in 1970, while Luna 20, in 1972, managed to return 55 grams (Slyuta, 2021). The Luna 24 mission introduced significant improvements, using two sliding rails to guide penetration and an everted soft tube for the first time in sample collection (Zhang, Zhang, Wei, Liu, Wang, Yuan, Pang, Guan, Hou, and Xu, 2022). The lander had a mass of nearly 6 tons, on Earth (60 kN) and 10 kN on the Moon, ensuring sufficient reaction thrust for the drill (Zacny, Bar-Cohen, Brennan, Briggs, Cooper, Davis, Dolgin, Glaser, Glass, Gorevan, et al., 2008). In the final mission of the series in 1976, Luna 24 achieved a maximum drill head depth of 225 cm, corresponding to 200 cm vertically. The sample holder began filling up at a depth of 58 cm, leading to a material column measuring 160 cm in length and weighing 170.1 g (Basilevsky, Ivanov, Ivanov, and Head, 2013). The collected samples were successfully returned to Earth on August 22, 1976 (Zacny, Bar-Cohen, Brennan, Briggs, Cooper, Davis, Dolgin, Glaser, Glass, Gorevan, et al., 2008).

Following a substantial pause in soil drilling in space exploration until the 21st century, subsequent missions primarily focused on shallow drilling or were not successful in penetrating the regolith like the Apollo and Luna missions. In 2008, the Mars Phoenix mission played a significant role. Landing on Mars, its mission included investigating water and signs of past or present microbial life. The robotic arm of Phoenix was equipped with the ISAD drill, designed to dig up to half a meter into the loose and moderately dense Martian surface, depending on the soil thickness above the icy soil deposits (Bonitz, Shiraishi, Robinson, Arvidson, Chu, Wilson, Davis, Paulsen, Kusack, Archer, et al., 2008). Phoenix not only confirmed the presence of water ice beneath the Martian surface but also detected traces of other minerals like carbonates and perchlorate salts (William and Jim, 2021). Despite being a solar-powered mission initially planned for three months in Mars' polar regions, Phoenix exceeded expectations, lasting five months, and it is considered a successful part of the low-cost Mars Scout program (William and Jim, 2021; Prince, Desai, Queen, and Grover, 2011).

However, when it comes to successful soil drilling, China's Chang'E 5 lander mission stands out as a counterpart to early missions such as Apollo 17 and Luna 24. Utilizing a 2-meter spiral drill on the Moon, it achieved a penetration depth of approximately 1 meter and collected 259.72 grams of regolith samples. The robotic drill of Chang'E 5 was designed with an automatically adjusted drilling principle, employing a low rotational speed of 40 rpm for loose lunar regolith and a high speed of 120 rpm for denser subsurface regolith. When the drill encountered a large rock at a depth of 1 meter, the percussion motor initiated a 30-second impact, but the rock remained partially penetrated. As a precaution for subsequent tasks, the drilling operation was terminated (Yong, ZHANG, Hongyu, Ting, ZHANG, Guidong, Kun, Shen, Guoxin, ZHANG, et al., 2023).

1.3.2 Upcoming Planetary Soil Drilling

In the upcoming planetary exploration, TRIDENT (The Regolith and Ice Drill for Exploring New Terrains) stands out as a cutting-edge lunar drilling subsystem explicitly designed for excavating regoliths up to 1 meter deep in the upcoming missions named Polar Resources Ice Mining Experiment-1 (PRIME-1) and Volatiles Investigating Polar Exploration Rover (VIPER) (Stoker, Glass, Stucky, Dave, Kobayashi, Quinn, Moreno-Paz, Sánchez-García, Mora, Kehl, et al., 2023; Paulsen, Mank, Wang, Chow, Hyman, Thomas, Lee, Zacny, Smith, Quinn, et al., 2018). TRIDENT is a 16-kg rotary percussive drill and deployment system designed with a 25.4 mm bit diameter, an auger with an average output torque of 5.5 N.m, a nominal speed of 12 rpm, and an average power consumption of 87 W. Its main goal is to penetrate the lunar subsurface up to a depth of one meter, collecting regolith cuttings for the evaluation of water and volatile content by MSolo (Mass Spectrometer observing lunar operations) in the PRIME-1 mission. (Paulsen, Mank, Wang, Chow, Hyman, Thomas, Lee, Zacny, Smith, Quinn, et al., 2018; Quinn, Captain, Eichenbaum, Aguilar-Ayala, Kleinhenz, Zacny, Chu, and Vendiola, 2023). Additionally, TRIDENT is equipped with advanced instrumentation to measure forces and displacements, allowing for meticulous evaluation of critical bulk properties of lunar regolith. This assessment yields valuable insights for

the future development of regolith mining equipment. Furthermore, MSolo in PRIME-1 is designed to analyze the composition of gases in its observational range, detecting emanations in proximity to the TRIDENT drill before, during, and after drilling operations (Quinn, Captain, Eichenbaum, Aguilar-Ayala, Kleinhenz, Zacny, Chu, and Vendiola, 2023). The drill utilizes a percussion mechanism powered by a motorized helical cam. This cam compresses a spring, storing an energy of 2 J. As a result, the hammer, with a mass of 0.626 kg, is expected to achieve a velocity of 2.53 m/s upon impact (Goldman, Flashner, and Yang, 2022). The nominal Percussion Rate is 972 blows per minute (BPM) (Quinn, Captain, Eichenbaum, Aguilar-Ayala, Kleinhenz, Zacny, Chu, and Vendiola, 2023), a significantly lower rate compared to ultrasonic and sonic drills driven by electrical components.

Another mission on the horizon is the highly anticipated ExoMars rover which will be landed on Oxia Planum, an ancient site on Mars. Oxia Planum is considered a promising location for uncovering evidence of past habitability and preserving biosignatures and organics (Vago, Westall, Coates, Jaumann, Korablev, Ciarletti, Mitrofanov, Josset, De Sanctis, Bibring, et al., 2017). The launch of the rover has experienced multiple delays and is expected to occur after 2028 (Wikipedia contributors, 2024). The mission comprises a lander and a rover equipped with an innovative 2.0 cm diameter rotary drill, including the Mars Multispectral Imager for Subsurface Studies (Ma_MISS). Ma_MISS, a miniaturized spectrometer, acquires crucial spectral data from borehole walls, aiding in understanding subsurface rock composition, properties, and potential biomarkers. This drill facilitates sampling from depths up to 2 meters, enhancing access to subsurface biosignatures shielded from surface hazards (Vago, Westall, Coates, Jaumann, Korablev, Ciarletti, Mitrofanov, Josset, De Sanctis, Bibring, et al., 2017; Ferrari, De Angelis, De Sanctis, Frigeri, Altieri, Ammannito, Formisano, and Vinogradoff, 2023). During travel, the drill box lies horizontally, adopting a vertical stance for drilling. Key drill components include a 70 cm long tool with a sample acquisition device, three 50 cm extension rods with optical and electrical contacts, a rotation–translation group, and a backup drill tool. The drill's penetration rate varies based on soil consistency, aiming for daily progress of approximately 50 cm (Altieri, Frigeri, Lavagna, Le Gall, Nikiforov, Stoker, Ciarletti, De Sanctis, Josset, Mitrofanov, et al., 2023). The drill achieves a penetration rate of up to 60 rotations per minute, contingent on soil consistency. In sandy or clay materials, the digging speed may range from 0.3 to 30 mm per minute (European Space Agency, 2021).

1.4 Advancements in Planetary Drilling Technology

Aside from the previous successful soil drilling missions, numerous investigations and design efforts have been undertaken to develop innovative probes capable of efficiently penetrating various soil layers on the Moon and other celestial bodies. The primary objective is to design probes that are compact and lightweight, addressing challenges associated with limitations in mass and volume transportation. In the following, several of these types of rigs are reviewed.

1.4.1 High Speed Penetrometer

The LUNAR-A Japanese Penetrator Mission, as outlined by Shiraishi, Tanaka, Fujimura, and Hayakawa (2008), aimed to explore the lunar interior through seismic and heat-flow experiments. The mission's profile included inserting the spacecraft into an elliptical lunar orbit, followed by the separation of the two penetrator modules near perilune at the 25 km altitude. Subsequently, small solid propellant motors de-orbited the penetrators, causing them to impact the lunar surface at a velocity of approximately 285 m/s. It was expected that each penetrator would go 1-3 m beneath the moon's surface, depending on the toughness of the terrain, providing enough insulation from harsh Moon surface temperature fluctuation. Each LUNAR-A penetrator, weighing about 14 kg and shaped like a missile, housed a two-component seismometer and a heat-flow probe alongside electronics, batteries, a tiltmeter, an accelerometer, and a radio communication system. The seismometer, employing a short-period electromagnetic type, demonstrated both high sensitivity and shock durability. The heat-flow probe, equipped with temperature sensors and thermal conductivity sensors, aimed to determine lunar heat-flow values through temperature gradient measurements. The mission was canceled due to cost considerations, with an estimated project cost of $135 million (NASA, 2023).

Similarly, Gao, Phipps, Taylor, Crawford, Ball, Wilson, Parker, Sweeting, Silva Curiel, Davies, et al. (2008) proposed a conceptual design known as the moonLITE spacecraft, inspired by GIOVE-A but featuring a simplified design with only one solar array. The moonLITE spacecraft was designed to carry four moonLITE penetrators. Each penetrator has a total mass of 36 kg, comprising 23 kg dedicated to propulsion and 13 kg for the actual penetrator, which carries a science payload weighing 2 kg. The science payload includes a three-axis micro-seismometer and a heat flow package. The design aims for the penetrator to impact the lunar surface at a speed of approximately 300 m/s, allowing it to penetrate beneath the lunar regolith and transmit valuable data. In 2007, NASA expressed interest in the project through the efforts of a BNSC/NASA Joint Working Group on lunar exploration. NASA had the potential to contribute different components to the mission. However, no advancements in the project were reported (Wikipedia contributors, 2023b), and a search on the UK Space Agency's official website yielded no results for the "MoonLITE" keyword.

More recently, the Canadian Space Agency recently supported a study and technology development project led by Magellan Aerospace to enhance a lunar penetrator concept named MAPLE (Multipurpose Autonomous Penetrator for Lunar Exploration). MAPLE is a cost-effective lunar exploration platform engineered for the velocity of impact up to 180 m/s to explore challenging lunar areas, both surface and subsurface. It integrates various sensors for on-site resource detection and utilization, featuring a partially shielded enclosure to mitigate impact shock. Magellan's effective prototype testing under the Canadian Space Agency's LEAP program establishes MAPLE as a valuable asset for future lunar exploration endeavors (Paul, Balaban, Parker, Spray, Ellery, and Megill, 2021).

However, the proposed systems lacked any mechanism to adjust the penetration depth after the initial impact. The depth of penetration is solely determined by the soil hardness

and impact speed, making it challenging to predict the penetration depth precisely. The range of penetration depth can be estimated, but exact values remain uncertain.

1.4.2 Bio-inspired Penetrometer

Numerous investigations have been done to replicate functional principles from organisms such as earthworms, caecilians, and razor clam locomotion to provide sufficient penetration for a probe. Omori, Murakami, Nagai, Nakamura, and Kubota (2012) designed a novel subsurface robot equipped with excavation and propulsion units for penetration into soils. The excavation unit, modeled after an earth auger and operating independently of the propulsion unit, demonstrated its effectiveness by successfully digging a hole. It reached a depth of 219 mm solely under the influence of gravity. The propulsion unit, inspired by the peristaltic crawling of earthworms, was designed to maintain the probe's vertical orientation, minimize deviation, and optimize friction for effective penetration. The integration of the propulsion unit was effective in supporting the excavation process. This integration reduced motor torque requirements and effectively prevented motor stalling by transferring excavated material from the front to the rear of the device. Subsequent experiments conducted with the robot operating at both its full weight and 1/6 of its weight highlighted the prototype's satisfactory performance up to a depth of 430 mm, where the discharged ports reached ground level, necessitating a halt in excavation. To overcome this limitation, the researchers used a dust collector, which facilitated the robot's impressive capability to reach a depth of 650 mm without any loss of speed. Therefore, with a properly refined and enhanced discharging unit, the potential for achieving even greater depths becomes likely. Subsequently, Mizushina, Omori, Kitamoto, Nakamura, Osumi, and Kubota (2013) addressed the challenge of efficiently removing soil debris from a drilled hole by introducing a mobile bucket mechanism to the system. As the robot digs, it gathers the excavated soil through a spout, guiding it into the mobile bucket. The filled bucket is then lifted back up above the starting point using a winder. This bucket mechanism enabled them to dig to a depth of 595 mm. However, a problem emerged during the removal process, where the falling soil debris disrupted the robot's digging efficiency. Additionally, the winder mechanism, consisting of a motor and pulley, increased the complexity of the system. Nakatake, Konno, Mizushina, Yamada, Nakamura, and Kubota (2016) proposed a solution for the problem of dropped soil by designing a regolith circulation system (Figure 1.1). They modified the auger by increasing the tip diameter, ensuring that the borehole diameter was larger than that of the casing pipe. This modification causes the dropped soil to move towards the front of the robot. Therefore, the soil that drops from the bucket and edge and wall surface of the borehole is redirected to the mobile bucket, preventing any disturbance to the crawl and avoiding excavation halts. The study reported an increase in burrowing depth to 938 mm.

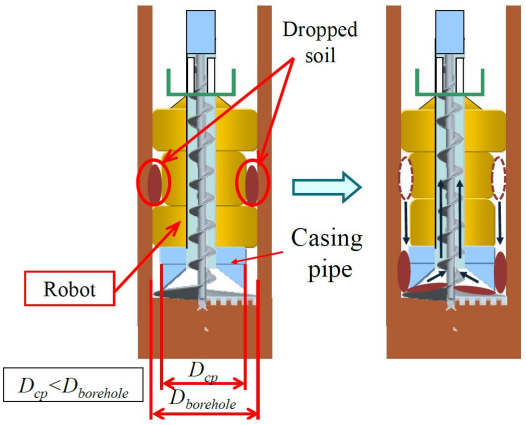

FIGURE 1.1: Soil circulating system.
Note: From (Nakatake, Konno, Mizushina, Yamada, Nakamura, and Kubota, 2016), p.409. © 2016, *IEEE*.

Subsequently, Tadami, Nagai, Nakatake, Fujiwara, Yamada, Nakamura, Yoshida, Sawada, and Kubota (2017) designed a specialized underwater robot called SEAVO to explore beneath the seafloor. The main distinctive feature of this robot was its ability to change direction. Like their previous prototypes, the robot consists of two main parts: one for excavating and one for propulsion. The excavating part has a flexible auger that can excavate while bent and an active bending joint that determines the direction of excavation. The propulsion part includes three propulsion subunits and two passive bending joints. Propulsion subunits use artificial muscles that expand and contract radially to grip the borehole wall, while axial expansion and contraction propel the robot forward. The team tested SEAVO's capabilities in digging in a curved borehole with a diameter of 160 mm, a turning radius of 1670 mm, and a depth of 613 mm. In 2019, an upgraded version of the robot, SEAVO II, was introduced (Isaka, Tsumura, Watanabe, Toyama, Sugesawa, Yamada, Yoshida, and Nakamura, 2019). This advanced model features a cone-shaped auger and a propulsion subunit with attached setae for improved performance. SEAVO II employs three independent propulsion subunits that expand and contract sequentially to propel the robot forward. During locomotion, two sub-units consistently grip the inner wall of the borehole, enhancing the robot's resistance to regolith pressure. This enhancement resulted in a 1.7 times improvement in gripping torque with the attached setae. Furthermore, the cone-tip-type earth auger reduced the required drilling torque. However, due to the confined dimensions of the experimental setup, SEAVO II achieved a limited burrowing depth of 430 mm within a period of 3231 seconds.

Similarly, Liu, Ozkan-Aydin, Goldman, and Hammond (2019) designed an earthworm-inspired burrowing robot with three pneumatic actuators. The robot consists of head and tail segments that expand radially as anchors and a middle segment that elongates the body. To mimic earthworm anchoring mechanisms, the robot incorporates origami skin and radially expanding pneumatic actuators. The origami structure unfolds into bristle-like spikes during radial expansion and folds down, creating a smoother skin structure during contraction. Compared with actuators lacking Kirigami skins, it was reported that robots

equipped with origami skin demonstrated enhanced anchoring force in cohesive regolith, increased forward displacement per gait cycle, and improved traction (Liu, Ozkan-Aydin, Goldman, and Hammond, 2019).

Moreover, Dewei, Weiwei, Shengyuan, Yi, and Huazhi (2015) developed an inchworm-like burrowing robot (IBR) for planetary underground exploration (Dewei, Weiwei, Shengyuan, Yi, and Huazhi, 2015). In 2020, the system was upgraded to connect to the planetary surface base via a flexible tether, autonomously exploring the planetary regolith (Zhang, Li, Jiang, Ji, and Deng, 2019). The upgraded system is called the inchworm drill (ID). Figure 1.2 shows the schematic design and drilling process of the ID. The ID comprises three modules: excavation (EM), discharging (DM), and propulsion (PM), with excavation anchor (EA) and discharging anchor (DA) at the EM and DM ends. A chip removal device (CRD) is attached to the ID to transfer soil debris from the borehole to the planetary surface, and it activates as required. The burrowing strategy unfolds as follows: (i) The DA is anchored to the borehole wall; (ii) The EM advances by drilling forward, rotating, and penetrating with the auger, while the DM rotates reversely; (iii) The EA is secured to the borehole wall, allowing the DA to detach and enabling the DM to proceed forward through rotation and penetration. This iterative process allows the IBR to burrow into the soil layer gradually. During lunar regolith simulant experiments, the ID achieved a drilling depth of 850 mm in 106 minutes (Zhang, Li, Jiang, Ji, and Deng, 2019).

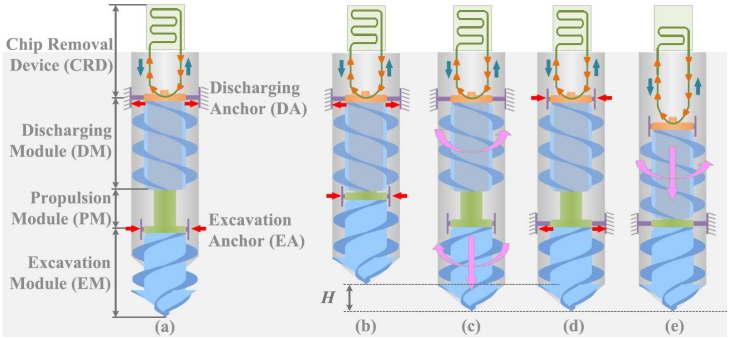

FIGURE 1.2: Conceptual design and drilling procedure of the ID.
Note: From (Zhang, Li, Jiang, Ji, and Deng, 2019), p.839. © 2020, *IEEE*.

In the analytical design approach, Khosravi, Martinez, DeJong, and Wilson (2018) investigated the penetration ability of limbless organisms, the penetration process and stresses, and its application for the development of self-penetrator rigs. Moreover, Martinez, DeJong, Jaeger, and Khosravi (2020) employed the cavity expansion analysis code ASCEND based on the model presented in (Chen and Abousleiman, 2013; Chen and Abousleiman, 2012) for quasi-static equilibrium condition to obtain the required dimensions and self-burrowing potential in different soil types for an idealized bio-inspired penetrometer with a radially expanding shaft and a penetrating tip.

The earthworm-inspired burrowing robot faces challenges due to its slow excavation speed. Its complex structure and intricate movement contribute to overall operational complexity and potential difficulties. Furthermore, the robot encounters obstacles when

trying to burrow into hard regolith, underscoring limitations in penetrating dense or solid surfaces.

The burrowing robot developed by Naclerio, Karsai, Murray-Cooper, Ozkan-Aydin, Aydin, Goldman, and Hawkes (2021) leverages multiple biological mechanisms to address the challenges in subterranean locomotion. **Tip extension**, modeled after plant roots, reduces drag by localizing movement to the robot's tip while keeping the body stationary. **Granular fluidization**, inspired by burrowing organisms like clams, mole crabs, and octopuses, uses tip-directed airflow to reduce resistive forces in the surrounding granular media. Finally, **asymmetric tip design**, based on desert-dwelling reptiles such as sandfish lizards and shovel-nosed snakes, allows the robot to modulate lift forces for precise navigation. These innovations enable faster, more efficient burrowing and steering in granular environments.

Alternatively, the dual-reciprocating drilling method (DRD) in wood wasp ovipositors, for example, eliminates the need for a high external axial force or overhead weight and seems to be a great promise for drilling in the extreme environment (low-gravity). The drill mechanism, ovipositors, consists of two valves that can slip longitudinally against each other. The reciprocating drill has backward-pointing teeth that present minimal resistance in penetration, going downwards, but interact with the surrounding substrate to avoid being pulled upwards, moving in the opposite direction (Figure 1.3 (Gao, Ellery, Jaddou, Vincent, and Eckersley, 2007)). The traction force generated by the backward-pointing teeth on the valve resisting being pulled upwards supports the whole mechanism to eliminate the need for an external force. Based on that, Gao, Ellery, Jaddou, Vincent, and Eckersley (2007) designed a bio-inspired micro-penetrator concept, less than 10 kg, consists of an aftbody and forebody. After ground impact, which was expected to occur at approximately 150 m/s, the forebody penetrates below the surface while the aftbody remains on the surface for communication purposes. By employing Young's empirical equation, they roughly estimated that the initial penetration would be around 0.6 and 1.3 m, depending on the regolith characteristics. Then, the self-contained drilling system continues for another meter. However, their mechanism's major drawback was the increase in buckling failure as it goes deeper into the ground.

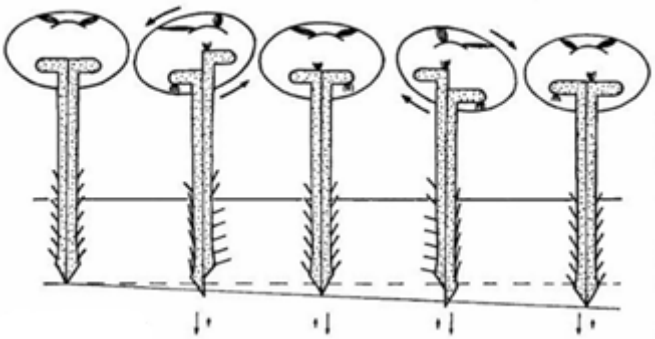

FIGURE 1.3: Wood wasp reciprocating piercing process.
Note: From (Gao, Ellery, Jaddou, Vincent, and Eckersley, 2007), p.878. © 2007, *IEEE*.

Gouache, Gao, Coste, and Gourinat (2011) used a double pin and crank rocker mechanism to realize this drilling motion and tested it for the first time to penetrate into two planetary regolith simulants. Their experiments showed a notable enhancement in the penetration depth with the same amount of overhead weight compared to static penetrations. Moreover, they observed that dropping the reciprocation motion amplitude reduced the forces on the drill bit while it didn't show adverse effects on the final penetration depth. Implementing higher frequency generally resulted in deeper penetration. During the experiments, they observed that the distance the drill progressed after a half cycle was less than the reciprocation movement's amplitude due to slippage. Very high levels of slippage have been reported in all the DRD tests. In their following study, Gouache, Gao, Frame, Coste, and Gourinat (2011) observed that the receding DRD valve traction force was one to two orders of magnitude less than the needed force for penetrating the regolith. Comparing the mono-block drill head (MDH) with DRD, they proposed pushing such a non-axisymmetric drilling tool into the ground would generate an axial resistance with lateral forces. The resulted lateral forces play a pivotal role in the performance of DRD by reducing the compression of regolith in front of the drill tip. The lateral forces' critical function in the DRD was further verified by numerical simulations (DEM). Therefore, the drill head's lateral movement seems to have a more influential role than the traction force to prevent slippage and leads to a more efficient penetration. Pitcher and Gao (2015) used a similar mechanism to Gouache, Gao, Coste, and Gourinat (2011) set-up with sixteen different drill heads to test the effects of drill head on drilling depth and power consumption. The radius of the backwards-facing teeth (teeth height) and the drill cylinder radius (root radius), and then the cone-half-apex angle showed the most noticeable impacts on the final achievable depth. The most interesting observation in their experiment was that when the bending occurred in the drill stem at a certain depth, the bent stem continued to penetrate at a fairly constant rate while the straight stem decelerated and finally stopped, highlighting the importance of lateral forces and sideways movements in the DRD performance improvement.

Pitcher and Gao (2017) experimented more on the effects of the lateral motion by

devising a mechanism that provides various forms of horizontal and vertical motions simultaneously (Dual Complex Motion Mechanism (DCMM)) and compared it with the simple penetration (only vertical motion (DRD)). They observed almost all experiments using a complex motion could achieve a greater depth for any vertical amplitude than the corresponding simple motion. Moreover, executing higher horizontal amplitudes led to increasing final achievable depths, while each horizontal amplitude gain achieved remained roughly constant with shifting only the vertical amplitude. Furthermore, they observed diagonal drillings (at an angle of 15°) that resulted in greater depths than the vertical ones (complex and simple). They proposed that the lower lateral pressure of the soil, compared to the vertical one, plays a role in the diagonal drilling's higher penetration depth.

Alkalla, Gao, and Bouton (2019) designed six new drill bits, concave/convex profile with straight/helical teeth, to test and compare its performance to the early design, cylindrical probe with a conical tip, in drilling into fine and coarse-grain Martian regoliths. With the same amount of overhead mass and power, 3 Kg and 45 watts, respectively, their proposed devices exhibited a notable drilling time reduction (20%–56.5%). Interestingly, they noted an important observation that occurred accidentally during a test when the mechanism-slider was very loose, causing the drill to vibrate during drilling. They observed that the vibrated run took half the time of the normal runs. Even though they disregarded this run, it supports the idea of a vibro-reciprocation drilling tool as a promising solution for drilling in low gravity.

The cam drive system designed for the DCMM by Pitcher and Gao (2017) was not efficiently compact for space exploration. Pitcher, Alkalla, Pang, and Gao (2020) proposed a self-contained compact design to address this problem (Figure 1.4). A cylindrical cam generated the reciprocating motion with dual followers to mimic wood wasp ovipositor. Inspired by a fish's caudal fin, they used a double-faced wedge to incorporate oscillation (lateral vibration) in the tool as well. The reciprocating motion is based on a cylindrical cam with dual followers. In this tool, Dual Reciprocation Oscillation Drill (DROD), the reciprocation motion mainly depends on the cam slope, while the lateral motion (oscillation) depends on both the cam slope and wedge angle. Moreover, they used EDEM software, a commercial DEM package, to compare drill–regolith interactions in a cohesionless model (Hertz-Mindlin) and cohesion model (Hertz-Mindlin with Johnson-Kendall-Roberts (JKR) cohesion). Reasonably, the cohesion model resulted in higher resistance in drilling and also pulling out from the substrate. Although the highly simplified model was able to capture the effect of microscopic parameters on the final macroscopic response, different parameters such as particle shape, size distribution, particle-particle and particle–wall friction forces need to be defined to have a more (quantitatively) realistic simulation. Alkalla, Pang, Pitcher, and Gao (2021) provided the detailed design of the proposed DROD, kinematics and dynamics simulation with ADAMS, and co-simulation environment between ADAMS and EDEM software to simulate the self-burrowing mechanism into soil particle.

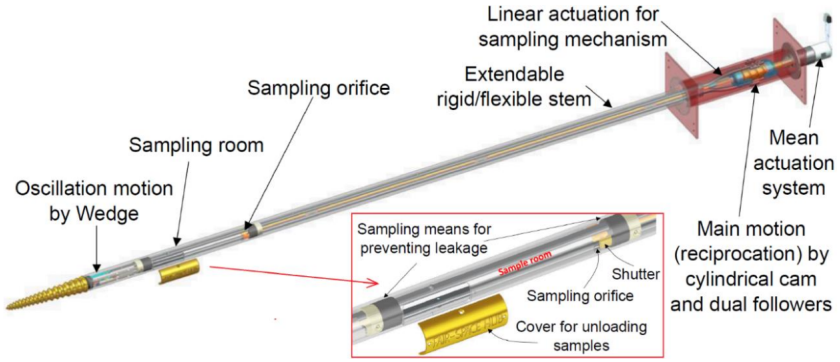

FIGURE 1.4: The DROD design.
Note: From (Pitcher, Alkalla, Pang, and Gao, 2020), p.16. CC-BY.

1.4.3 Mole Penetrometer

The Mole Penetrometer stands out as an innovative self-burrowing probe designed for granular materials. This specialized device incorporates an internal hammering system, allowing it to autonomously navigate and penetrate through various granular substances. The first small prototype, a compact percussive Mole (325 mm length, 19 mm diameter, 400 g mass), known as 'Mobile Penetrometer-1' or MP-1, was developed during 1995-97. It was based on a significantly larger design prototyped by the Russian Mobile Vehicle Engineering Institute (VNIITransmash) in St. Petersburg. VNIITransmash was responsible for scaling down the tool to meet the space exploration requirement in the frame of a European Space Agency (ESA) study led by Tecnospazio, where the German Aerospace Centre (DLR) was responsible for testing (Gromov, Misckevich, Yudkin, Kochan, Coste, and Re, 1997). Friction contact of the tool's housing and regolith diminishes the recoil motion, eliminates the need for external overhead force, and creates the forward motion of order of a few millimetres per strike (Richter, Coste, Gromov, and Grzesik, 2004).

Subsequently, Richter, Kochan, Gromov, and Coste (2000) designed the 'Mole with Sampling Mechanism' (MSM) for the 'Beagle 2,' a British Mars lander intended for repeated subsurface soil sampling. The reverse hammering mechanism facilitated the rig's retrieval through the tether connecting the Mole to the host lander. Later, (Richter, Coste, Gromov, Kochan, Nadalini, Ng, Pinna, Richter, and Yung, 2002) modified the MSM and developed a new robotic Mole prototype known as "PLanetary Underground TOol" or PLUTO. This robotic Mole weighs 900 g, has a length of 380 mm, and is tethered to a winch on the ground surface for power supply and recovery. PLUTO has the capability to move across the surface or burrow into the subsurface, collecting a regolith sample in a cavity at its tip. Tests for the ground penetration and retrieval of the PLUTO Mole were conducted at DLR. The PLUTO successfully penetrated to a depth of approximately 2 meters in a mixture of Flintag and quartz sand in about 3500 seconds. In quartz sand alone, it reached a depth of around 60 centimeters in approximately 3000 seconds (Richter, Kochan, Gromov, and Coste, 2000). Next, PLUTO was added to Beagle 2, and it was designed to be deployed using a robotic arm. Beagle 2 was scheduled to land on the surface of Mars on December

25, 2003. However, communication with the lander was lost, and it was initially declared lost in February 2004. In January 2015, new images from NASA's Mars Reconnaissance Orbiter suggested that Beagle 2 had successfully landed on Mars but had failed to deploy its solar panels fully, hindering its ability to communicate (Wikipedia contributors, 2023a).

Similarly, Stoker, Gonzales, and Zavaleta (2007) developed the Moon Mars Underground Mole (MMUM), a lightweight, low-power subsurface access system designed for lunar and Martian exploration. The system, with a total mass of 2000 g, a diameter of 40 mm, a total length of 600 mm, and a maximum power of 10 W. Derived from the PLUTO mole, the MMUM utilizes a pointed slender cylinder with an internal sliding hammering mass to efficiently penetrate soil, reaching depths of up to 2 meters. With a single motor design, the MMUM can collect 7 grams of soil samples, conduct RAMAN spectroscopic analysis, and measure soil temperature while maintaining low mass and power consumption. The MMUM underwent testing in wet beach sand, intended to represent Lunar regolith, with a density of 1.7 g/cm^2 and a compressive strength of 15 kPa. Operating autonomously for 8 hours without problems, the MMUM experienced a slowdown in penetration during the last hour, and finally, the test ended at around 500 mm depth. Apparently, a large stone was discovered just below the final depth achieved by the MMUM.

After PLUTO, HP^3 on the Martian InSight lander is the second application of the Mole concept in a space mission (Spohn, Grott, Knollenberg, Zoest, Kargl, Smrekar, Banerdt, and Hudson, 2012; Wippermann, Hudson, Spohn, Witte, Scharringhausen, Tsakyridis, Fittock, Krömer, Hense, Grott, et al., 2020). The DLR developed HP^3, a compact probe ($3kg$), consisting of a self-contained spring motor hammering mechanism (Mole). The spring motor mechanism provides repeated impacts to dig into the Mars surface while the pulling tether contains the TEM-P (Thermal Excitation Measurement-Passive). The heat probe, used in NASA's discovery InSight mission (Interior Seismic Investigations, Geodesy and Heat Transport), aims to penetrate 5 meters into Mars's surface and record temperature gradient for one Mars year (nearly two Earth year). Moreover, Mole penetration enables measuring near-surface soil parameters and seismic waves through the hammering process (Golombek, Grott, Kargl, Andrade, Marshall, Warner, Teanby, Ansan, Hauber, Voigt, et al., 2018). During the penetration process, in each 0.5m, it stopes to measure the regolith thermal conductivity (Olaf, Marco, Fittock, Georgios, Torben, Lars, Matthias, Jörg, Tilman, Christian, et al., 2019). Therefore, it would be possible to identify Mars's inner core source of energy, its properties and compare Mars's evolution with the earth (Foust, October 27, 2019). However, after drilling only 30 centimetres, far below five meters, an unexpectedly tough soil held up the Mole's progress. The Engineer team tried to resolve the problem using a scoop to push the Mole on the hole's side, increasing the friction. But it worked temporarily, and again it couldn't make any progress and mostly bounced out of the hole (Foust, October 27, 2019). The HP^3 design was based on the previously reported Martian regolith, which was totally different from the clumpy dirt encountered this time. The friction between the tool and the regolith was not enough for the Mole to go deeper than a half meter. Tilman Spohn, the experiment's lead scientist from the German Space

Agency, said that: "we've given it everything we've got, but Mars and our heroic mole remain incompatible" (Dunn, 2021). After the final attempt, On January 14, 2021, NASA declared the team has given up, and the part of the mission related to the heat probe is over (Wikipedia contributors, 2021).

1.4.4 Ultrasonic/Sonic Drilling Rigs

Percussion is instrumental in fracturing rigid, brittle materials such as concrete, stones and ceramics. In contrast, rotation is more effective in soft and ductile materials such as wood, plastics (Badescu, Bar-Cohen, Sherrit, Bao, Chang, Donnelly, and Aldrich, 2012). One of the proposed designs to overcome the drilling challenges in planetary missions was an ultrasonic/sonic driller/corer (USDC) mechanism for rock drilling (Sherrit, Bao, Chang, Dolgin, Bar-Cohen, Pal, Kroh, and Peterson, 2000). The USDC consists of three main parts: an ultrasonic horn transducer (actuator: piezoelectric stack, backing element, and a horn), a free mass and a drill stem. The piezoelectric stack is confined and remained in compression between the backing and the variable cross-section horn. The horn amplifies the longitudinal vibrations from the piezoelectric stack and vibrates at its resonant frequency of around 21.5 kHz. It results in a free mass vibration between the horn tip and the top of the drill stem with average frequencies between 100 and 1000 Hz. Sonically stress pulses transfer the ultrasonic energy from the transducer to the drill stem and create shock waves at the bit/rock interface. Rock fracture occurs when fatigue strength is finally passed by hammering. The lightweight (450 g) prototype, shown in Figure 1.5 (Bar-Cohen, Sherrit, Dolgin, Bridges, Bao, Chang, Yen, Saunders, Pal, Kroh, et al., 2001), proved to be efficient for drilling different rocks at shallow depth with low preload (less than 5 N) and low driven power (Bao, Bar-Cohen, Chang, Dolgin, Sherrit, Pal, Du, and Peterson, 2003). Subsequently, the device was mounted on several rover configurations (Sojourner Rover and FIDO Rover) (Bar-Cohen, Sherrit, Dolgin, Bridges, Bao, Chang, Yen, Saunders, Pal, Kroh, et al., 2001). However, removing cutting after a certain depth becomes problematic and reduces its efficiency (Wang, Quan, Yu, Bai, Li, and Deng, 2018). Cardoni, Harkness, and Lucas (2010) proposed two new ultrasonic drilling devices where the ultrasonic bits were designed to transform the longitudinal vibrations into longitudinal-torsional vibration. In their preliminary drilling tests, it was observed that composite mode devices could improve drilling/coring efficiency.

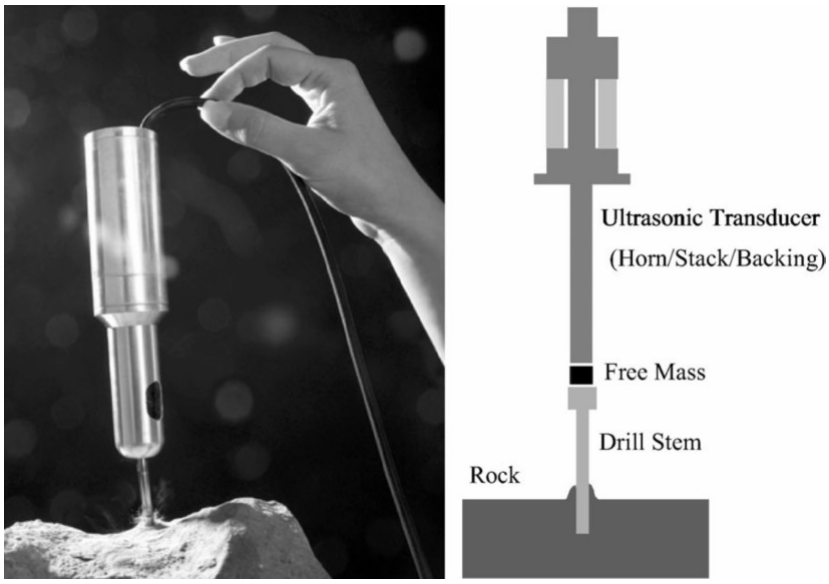

FIGURE 1.5: The USDC coring with minimum axial force and its schematic design.
Note: From (Bao, Bar-Cohen, Chang, Dolgin, Sherrit, Pal, Du, and Peterson, 2003), p.1148. © 2003, *IEEE*.

Bar-Cohen, Badescu, Bao, Sherrit, Zacny, Sadick, and Ji (2010) developed an autonomous wireline rotary-percussive drill called the Auto-Gopher by incorporating the Ultrasonic/Sonic piezoelectric mechanism and a rotary unit. Enhanced hammering by rotation of the bit with flutes provides both efficient cutting and faster drilling. Similarly, Badescu, Bar-Cohen, Sherrit, Bao, Chang, Donnelly, and Aldrich (2012) employed a piezoelectric transducer in a commercial rotary drill to examine the percussive augmenter effects in drilling rocks. The device, Percussive Augmenter of Rotary Drills (PARoD), showed a remarkable improvement in penetration rate by incorporating the ultrasonic hammering action on fluted bits. The advancement was due to the ultrasonic percussive enhancement in breaking the rock combined with the fluted bits' rotation to remove the cutting from the borehole. However, the added electromagnetic motor to provide rotation in the rotary-hammer ultrasonic drills would reduce the operating temperature range and increase the design's complexity and size.

Sherrit, Domm, Bao, Bar-Cohen, Chang, and Badescu (2012) designed a piezo-driven rotary-hammer ultrasonic drill that is more compact and has lower power consumption requirements. A horn with asymmetric groves was designed to transfer the piezoelectric longitudinal vibration into longitudinal-torsional vibration and impart the resulting longitudinal (hammering) and transverse force (rotation) to a keyed free mass. The fabricated prototype, Single Piezo-Actuator Rotary-Hammering (SPaRH) Drill, showed satisfactory drilling into limestone. The optimization of the drill geometry and material needs more investigation, but they observed that decreasing the free mass weight by 25% could result in a four times higher drill rate. Employing 4 lbs preloads (the repulsive magnets loading the drill string and free mass against the horn tip), 3 lbs weight-on-bit, and 100 W input power, resulted in the 8 mm/min drill rate. They suggested that the vibrations also reduce

friction with the auger surface by fluidizing the powdered cuttings inside the flutes.

Wang, Quan, Yu, Bai, Li, and Deng (2018) introduced a Rotary-Percussive Ultrasonic Drill (RPUD) for rock sampling in minor planet exploration. RPUD, unlike the previous studies, was designed to use the longitudinal vibration energy of piezoelectric ceramics on both sides. While a percussive horn amplifies and delivers the longitudinal vibration to the free mass, a V-LT coupler of the rotary unit on the other side of the piezo-ceramics creates an elliptical trajectory on the coupler tip to convert the longitudinal vibrations into longitudinal-torsional vibration. The actuator parameters were selected to have the same operating resonance frequency in the rotary and percussive units. Their experiment showed that reasonably the drilling efficiency has improved in RPUD compared with percussive drilling. Under the driving frequency of 19.95 kHz, voltage of 225 V_{pp}, and a preload of 18 N, the maximum speed was 117.75 rpm, and the maximum torque was 38 mNm. After five minutes of drilling with 7 N weight on bit, RPUD achieved 22 mm drilling depth, and their data showed it could exceed this value by further drilling. In contrast, the percussive drilling showed a more noticeable reduction in its efficiency as it progressed more. It finally reached the drill depth of 15.5 mm in five minutes, while further progress seemed almost unlikely.

Bai, Li, Quan, Tang, and Deng (2023) improved the RPUD by harnessing vibrational energy from one end of a piezoelectric stack to reduce the length and weight of the drill device effectively. The design incorporates a bolt-clamped piezoelectric actuator configuration and a longitudinal-torsional (LT) coupler to convert longitudinal vibrations into longitudinal-torsional vibrations. These transformed vibrations generate elliptical trajectories at the driving tips of the coupler, which leads to the continuous rotation of the drill tool. Simultaneously, the free mass between the percussive horn (stepped horn) and the drill tool transfers longitudinal vibrations to the drill tool. The actuator exhibited resonance frequencies of 18.376 kHz (simulation) and 18.115 kHz (experiment). With a weight of 560 g, the RPUD is well-suited for low-gravity environments, operating efficiently with a minimal load on the drill bit. The prototype demonstrated a no-load rotary speed of 119.2 r/min and a maximum drilling rate of 7 mm/min in sandstone, with the weight on the bit being 5 N.

Similarly, Li and Harkness (2023) compared the performance of Langevin-style ultrasonic drill tools actuated by Mn:PIN-PMN-PT piezocrystals and Pz26 piezoceramics. While piezocrystals demonstrated superior electromechanical properties, including higher coupling coefficients and lower impedance magnitudes at resonance, their performance at high excitation levels was constrained by greater piezoelectric losses. The piezocrystal tool achieved marginally lower cutting forces and power consumption, with significant benefits observed in sandstone and marble but limited impact on softer and more complex rocks. Similar tool wear patterns were noted for both materials. The study suggests exploring alternative excitation modes to fully leverage piezocrystals' potential for ultrasonic drilling in challenging environments. Another study by Wang, Li, Quan, Harkness, and Deng (2024) investigated passive versus active control of weight-on-bit (WOB) for ultrasonic percussive drills in planetary exploration. The study highlights that active control, implemented using

a linear actuator, provides better adaptability to variations in rock compressive strength and WOB compared to passive control with suspended weights. While passive control showed slightly better performance at lower WOB (5 N), active control outperformed it at higher WOB levels (10 N and 15 N). Active-controlled drilling also facilitates cuttings removal due to the backward movement of the drill, though further optimization of the control algorithm is required.

For the case of granular materials, Firstbrook, Harkness, and Gao (2014) conducted a series of experiments to observe high-powered ultrasonic vibration effects on penetration in granular material. An ultrasonic Langevin transducer provided ultrasonic vibration of 20 kHz up to 10 μm amplitude. The horn, penetrator was manufactured from 94Ti/6Al/4V alloy and designed to resonate in the second longitudinal mode at 20 kHz with the resulting amplification ratio (gain) of 3.5. The rig was set to penetrate different Martian regolith simulants with high and low density at slow (3 mm/s) and fast (9 mm/s) rates corresponded to 4.81 V and 12 V, respectively. While slow non-ultrasonic penetration needed a larger overhead force, they observed the opposite was true in ultrasonic penetrations. Moreover, adding ultrasonic vibrations led to a marked reduction of the required peak axial force. It seems that the ultrasonic vibration provides granular fluidization in the immediate surrounding of the drill, reducing the surface friction and assisting sand particles mobilization and the probe penetration. The highest reduction of axial force occurred using the lowest amplitude of 1 μm, which corresponded to the lower total power consumption (actuator and ultrasonic units). After that, the peak penetration force reduction became more gradual and less conspicuous. Interestingly, the high-density regoliths exhibited a more significant reduction in the peak force than the low-density regoliths by implementing the ultrasonic vibrations. Therefore, incorporating the ultrasonic technique in self-burrowing probes seems helpful for penetration into the lunar regolith, which has a high relative density just a few centimetres below the surface.

In their subsequent study (Firstbrook, Worrall, Timoney, Suñol, Gao, and Harkness, 2017), they tried to investigate gravity's effect. They only considered the high-density regoliths with the faster penetration rate (9 mm/s-12 V) with a higher resolution of amplitude in the range of 0-2 μm. The tests were conducted in a centrifuge, a cost-effective method to examine gravity's effects, to observe penetration in higher gravities (1g-10g) and extrapolate results downward. Regardless of gravity, the ultrasonic vibrations assisted penetration. Higher gravities led to implementing higher axial forces. Moreover, in lower gravities, the percentage of reduction in penetration forces was higher. For example, they observed that the force could be reduced by 70% in the gravity of g and 1 μm amplitude of vibration, while the reduction would be just 50% in 10 g for the same vibration's amplitude. Therefore, the trend suggests that these benefits could be advantageous in lower gravity to compensate for axial force and weight on bit. Similarly, Firstbrook, Worrall, Timoney, and Harkness (2018) observed a noticeable enhancement in a percussive probe's drilling efficiency by synchronizing short ultrasonic vibration pulses with the hammer impact. The number of hammer strikes needed to achieve a specified depth (190 mm) at the highest excitation amplitude (1.6 μm) was reduced from 48 to 15 and from 33 to 17 for BP (D_r =48.3%)

and SSC-3 (D_r =43.1%), respectively. In addition, it was noticed that at low penetration depths, implementing only ultrasonic vibration could fluidize the sand to such an extent that the penetrator had a brief moment of near-freefall. This advantage is beneficial for future probe applications on the moon. The probe can exploit the ultrasonic vibration to bury itself into the loose regolith on the moon's surface on its weight. Subsequently, the ultrasonic vibration performs its capacity to assist the primary mechanism in penetrating the dense regolith just a few centimetres below the surface.

Firstbrook, Worrall, Harkness, Flessa, McGookin, and Thomson (2018) investigated the effects of ultrasonic vibration on auger drilling performance. Glass microspheres with a particle size distribution of 150-250 mm were chosen to replicate the penetration in fine-sand. The maximum overhead force was approximately reduced from 600 N to 100 N only by implementing rotary penetration (14.7 RPM) compared to the non-rotary one. On the other hand, ultrasonic vibration was able to reduce it roughly to 350 N in the non-rotary penetration by implementing an amplitude of 10 μm. Therefore, it seems that rotation has much more significant effects on the reduction of required overhead force than the ultrasonic vibrations. Moreover, the required force was independent of any ultrasonic vibration in the rotary penetration, indicating the force had already been adjusted more than ultrasonics could provide. However, the required maximum torque decreased from 120 Nm to 85 Nm (30% reduction) by increasing the ultrasonic vibration amplitude from 0 to 10 μm.

Additionally, Rezich, Harrigan, Thomas, and Ludwiczak (2021) investigated the use of longitudinal ultrasonic vibrations at 20 kHz to reduce penetration forces in granular materials, specifically GRC-3 lunar soil simulant. Using NASA Glenn's Vibratory Excavation (VEX) rig, which limited the penetration depth to approximately 47 mm, they observed up to a 70% reduction in penetration force when vibrations were applied. The study found that factors such as probe geometry and the presence of vibrations had a more significant impact on force reduction than amplitude or penetration velocity, with small amplitude vibrations proving sufficient for substantial improvements. These findings suggest that longitudinal vibrations can enhance the efficiency of excavation tools for off-Earth applications.

1.5 Gaps in knowledge

Regarding the lunar impactors, the development of an analytical solution that explicitly relates various mechanical properties of granular media, such as friction angle and cohesion parameters, to penetration depth is highly advantageous for the design of high-speed probes. Analytical methods, some of which offer closed-form solutions, provide a direct connection between the penetration process and the stresses exerted on the projectile, all linked to the mechanical characteristics of the target medium. What makes these analytical approaches particularly useful is their ability to bypass the need to develop complex contact algorithms for discrete media. This computational convenience makes them highly practical for engineering design and benchmarking purposes. While several closed-form or

semi-analytical solutions have been explored, none have explicitly integrated the dynamic cavity expansion theory in relation to friction angle and cohesion parameters. However, for most geomaterials, including lunar regolith simulants, obtaining the Mohr-Coulomb criterion parameters—represented by friction angle and cohesion— is feasible through conventional geotechnical tests.

Furthermore, regarding the drilling tools, despite the research on high-power longitudinal vibration, animals like snakes, horned lizards (Sherbrooke and Nagle, 1996), and sandfish (Baumgartner, Fidler, Weth, Habbecke, Jakob, Butenweg, and Böhme, 2008) use a different, low-frequency lateral vibration to dig or hide in granular materials (refer to Figure 1.6). For instance, Maladen, Ding, Li, and Goldman (2009) examined the locomotion mechanics of the sandfish lizard (Scincus scincus) as it navigates granular media. Using high-speed X-ray imaging, they observed that once below the surface, the sandfish stops using its limbs for propulsion and instead relies on an undulatory traveling wave along its body to produce thrust and counteract drag. Therefore, an unexplored aspect in the realm of soil drilling tools for space missions is understanding how other types of vibrations or frequencies might impact the process of penetrating granular materials. It is crucial to explore whether bending vibrations or whirling or chaotic motions of the probe structure and nose at ultrasonic or sonic frequencies can be effective in soil fluidization and assisting penetration. Determining the most efficient vibration frequencies and modes is pivotal for designing compact probes for future space missions.

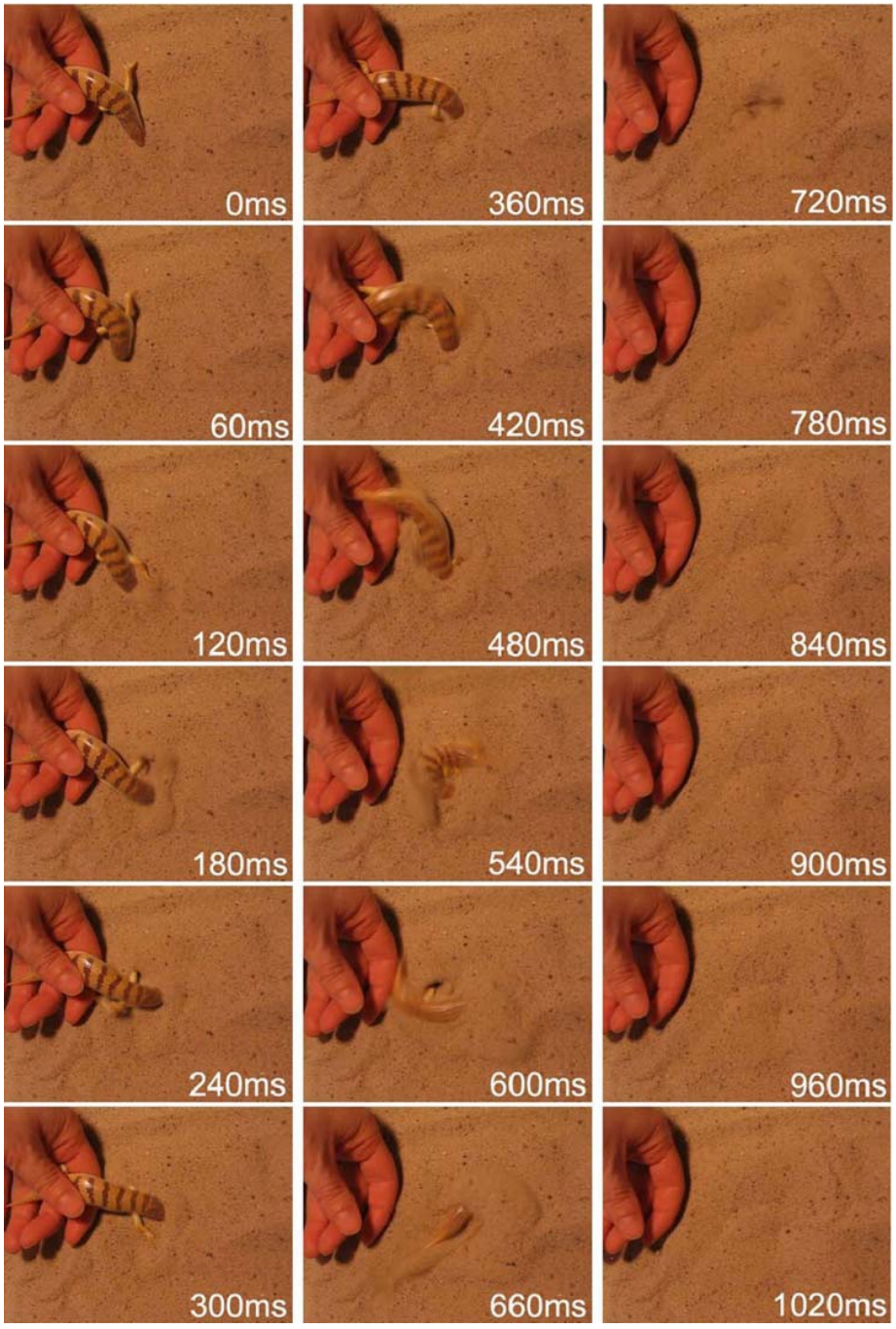

FIGURE 1.6: Rapid burying of an adult sandfish with a sinusoidal lateral vibration.
Note: From (Baumgartner, Fidler, Weth, Habbecke, Jakob, Butenweg, and Böhme, 2008), OPEN ACCESS.

1.6 Goals and objectives

This research has three main goals, each aimed at improving probe technology for space exploration. The objectives are as follows:

- **Objective 1: Development of Analytical Tools for High-Speed Probe Design**
  Our primary objective at this step is to create analytical tools that explicitly link the

friction angle, cohesion parameters, and various mechanical properties of granular media to penetration depth. This would be valuable for designing a subsonic robotic probe where the initial impact buries the tool underground. Subsequently, the robotic system makes adjustments for further penetrations, utilizing the developed analytical tools to estimate stresses and predict the final penetration depth. To achieve this, we will employ the Mohr-Coulomb criterion in a form more readily applicable to lunar regolith and geological materials. Our approach involves representing the plastic region by considering the target material as a compressible medium. Emphasizing subsonic velocity ranges of impact aligns with the likely scenarios in planetary low-gravity conditions. For example, free-fall launch from a lunar orbiter or lander at 25 km to the Moon's surface can achieve impact velocities around or below 285 m/sec. This subsonic impact is essential to prevent high shock wave propagation in the probes, avoiding issues like bulging, structural damage, and deformation. Furthermore, this ensures the safety of the sensors and navigating system onboard. The developed equations will serve as valuable tools for estimating and assessing stresses on compact projectile probes and predicting the final penetration depth.

- **Objective 2: DEM-Based Exploration of High-Frequency Vibro-Probes for Enhanced Penetration in Granular Media**
  In this objective, our aim is to numerically investigate the effects of high-frequency vibrations on minimizing the required force for the penetration of a probe into granular media. Employing the Discrete Element Method (DEM), we will investigate the impact of vibration frequency, mode, and the probe's head on penetration resistance.

- **Objective 3: Experimental Investigation of Bending Vibration-Enhanced Penetration in Granular Media**
  Moving beyond DEM simulations in the previous step, this objective dives into real-world experiments to understand how bending vibrations can make penetrating granular materials easier. Drawing inspiration from biological mechanisms observed in snakes, horned lizards, and sandfish, we will develop a novel vibro probe for our experimental investigations. Employing experimental modal analysis, we will pinpoint resonance frequencies before pushing the probe into granular materials using a linear actuator. The next phase includes a comparative analysis to evaluate how bending vibrations impact the reduction of penetration force across different resonance modes.

1.7 Validation

We utilized two available field experiments to validate the analytical tools developed in Chapter 2 for estimating high-speed probe penetrations within the subsonic range. In Chapter 3, we employed the Discrete Element Method (DEM) simulation to examine the feasibility of using vibrations to reduce penetration forces in granular materials. Building on these simulations, Chapter 4 and Chapter 5 introduce experimental observations to

complement and confirm our findings. This chapter explores the practical impact of bending vibrations on reducing penetration forces through experiments.

1.8 Thesis structure

This thesis is organized into several chapters, each contributing to the overall understanding and achievement of the research goals. The structure is outlined as follows:

- **Chapter 2: Modelling the Penetration of Subsonic Rigid Projectile Probes into Granular Materials Using the Cavity Expansion Theory**
  In this chapter, we propose compact subsonic projectile probes as an alternative to traditional subsurface investigation tools for extraterrestrial exploration. Launched from lunar orbiters or landers, these probes address payload limitations in space missions. Accordingly, aligns with (Objective 1), the chapter focuses on developing analytical tools for high-speed probe design, specifically applying the Mohr-Coulomb criterion and representing the plastic region as a compressible medium. The spherical cavity expansion model is employed to predict probe deceleration and final penetration depth during perpendicular subsonic impact. Validated through available field experiments, the model provides reliable predictions for projectile penetration, final depth, and probe stresses.

- **Chapter 3: Penetration Analysis of High-Frequency Vibro-based Probes in Granular Media Using the Discrete Element Method**
  This is dedicated to the second research (Objective 2), involving a numerical investigation using the Discrete Element Method (DEM). It explores the impact of high-frequency vibrations on reducing penetration resistance in granular media, considering factors such as vibration frequency, mode, and probe head design.

- **Chapter 4: The Effect of Bending Vibration Modes on Penetration of Bio-Inspired Drilling Tool in Granular Materials: An Experimental Study**
  Building upon the DEM simulations, this chapter shifts its focus to practical experiments, aiming to validate the impact of bending vibrations on penetration in granular media (Objective 3). A hex probe is designed given the fact that the hex profile is less demanding in machining for attaching the piezo patches and is also a commonly available profile. Inspired by biological mechanisms observed in nature, a novel vibro probe is developed and tested using experimental modal analysis and penetration tests. The chapter includes a comparative analysis exploring the probe's penetration performance across various resonance modes.

- **Chapter 5: Experimental Investigations of the Effects of Bending Vibrations Resonance Modes on Penetration into Granular Materials**
  Building on previous experimental findings demonstrating the impact of bending resonance modes, our focus shifts to practical experiments aimed at confirming how bending vibrations from multiple directions affect penetration in granular media

(Objective 3). Given the fact that octagonal and higher-edged profiles are less common and the unsuitability of hex probes for two-directional bending excitations, we opt for a circular probe design. This design, with proper machining tools allows to attach piezo-electric patches in the required directions, enabling bending vibrations in multiple directions. Additionally, circular probes are more commonly used for soil penetration. With the new probe configuration, we compare the results of bending vibrations in one and two directions to assess and compare their impact on penetration resistance. Furthermore, we compare these results with those obtained using the hex probe in the previous chapter (Chapter 4) to determine which profile geometry offers greater benefits in reducing penetration force.

- **Chapter 6: Conclusions, Future Directions, and Practical Applications**
  The final chapter summarizes the key findings and contributions of the research. It also outlines potential avenues for future work and advancements in the field of probe technology for both space exploration and terrestrial applications

Chapter 2

Modelling the Penetration of Subsonic Rigid Projectile Probes into Granular Materials Using the Cavity Expansion Theory

Abstract

Typical subsurface investigation tools used on Earth are not applicable for subsurface exploration of the Moon and other extraterrestrial bodies due to payload limitations in space missions. Instead, light and compact subsonic projectile probes can be considered as an alternative subsurface investigation tool in such exploratory missions to overcome a host of challenges. Such probes can be launched from a lunar orbiter or lander to the surface of the Moon to provide the initial effective penetration from the impact. Here, we develop a model based on the spherical cavity expansion theory to predict the deceleration rate and final penetration depth of a rigid projectile probe into geological targets under the perpendicular subsonic impact. Two stress fields are assumed to propagate in the medium, plastic (near field) and elastic (far field), upon the impact. The stresses at the cavity wall are obtained by combining the Mohr-Coulomb failure criterion for the target failure (plastic region) considering two different assumptions for plastic wave propagation. Two field experiments are used to compare and assess the robustness of the proposed solutions in

Alaei Varnosfaderani, M., Maghoul, P., Wu, N. (2022). "Modelling the penetration of subsonic rigid projectile probes into granular materials using the cavity expansion theory." *Computers and Geotechnics*, 141, 104546. https://doi.org/10.1016/j.compgeo.2021.104546.

the subsonic range. Based on the simulation results and the experiments, it is concluded that the cavity expansion model considering the locked hydrostat assumption, with the modification here introduced for the volumetric strain, can provide us with a reasonable prediction of the projectile penetration, final penetration depth and the stresses on the probe. Thus, our proposed solution can be used as a benchmark for sophisticated and computationally-expensive numerical calculations.

2.1 Introduction

Penetration mechanism in different target materials such as metals, ceramics, composites, concrete, and granular materials has been widely studied in the literature. However, the response of granular materials includes some complexities that cannot be seen in other target media. For instance, in a small uniaxial stress-strain, the behaviour of sands is significantly affected by its relative density, which is 0% for the lowest possible packing and 100% for the highest one. For large strains, similar behaviour in loosely and densely packed granular materials is observed (Omidvar, Bless, and Iskander, 2019). Furthermore, for most alloys and engineering materials, sound waves propagate with a speed of 1 to several kilometers per second (km/sec). So, the shock waves cannot easily occur in such media. However, for sand, where the sound speed is typically in the range of a few hundred meters per second (Allen, Mayfield, and Morrison, 1957), supersonic penetration becomes a readily observable behavior at considerably lower velocities compared to alloys, which exhibit sound speeds of several kilometers per second. In addition, the large volume of collapsible pores in granular materials enables particles to rearrange and create significant changes to the voids volumes, consequently absorbing a relatively high amount of projectile energy. In higher confining pressures and more compacted sand, particle crushing and abrasion are increased in a high-velocity impact (Cooper and Breaux, 2010). Furthermore, shear dilatancy is a common phenomenon where densely packed granular material expands in volume under the presence of shear forces. On the other hand, loosely packed granular materials tend to contract under shear forces (Omidvar, Bless, and Iskander, 2019).

Penetration in granular materials is highly dependent on the velocity regime. In quasi-static penetration, e.g. very low penetration velocities, inertial effects do not create perceptible penetration resistance, and penetration happens as a result of exerting an external load. Below the sound speed in granular materials, which is typically in the range of 100 to 600 m/sec for soils (Lo, Yang, Hsu, Chen, Yeh, and Hilpert, 2017), penetration is in

the subsonic regime. In this regime, penetration largely relies on the kinetic energy of the projectile. Sound speed depends on the loading and pressure, porosity and packing, and mineral composition. Penetration velocities exceeding the sound speed in the medium and below 1,500 m/sec is termed supersonic penetration. Above this refers to hypervelocity projectiles such as meteors (Omidvar, Iskander, and Bless, 2014).

In the case of granular material, typically, penetration classifies into transient and deep penetration. Transient penetration mostly concentrates on the formation of the surface crater and high-pressure shock waves in high-velocity impacts, tens of kilometres per second, on Earth or other planets for short projectiles (Ruiz-Suárez, 2013; Turtle, Pierazzo, Collins, Osinski, Melosh, Morgan, and Reimold, 2005). Generally, the energy of a short projectile penetrating into dry sands dissipates as it moves grain particles in the medium at the initial penetration stage (Collins, Addiss, Walley, Promratana, Bobaru, Proud, and Williamson, 2011). On the other hand, significant displacements in deep penetration for long projectiles lead to large shear and compression forces in granular materials. Locally, high stresses can often lead to grain fractures and even full comminution (Omidvar, Iskander, and Bless, 2014). Usually, a penetration depth of around 1-3 projectile diameters plus the nose length is sufficient for an assumption of deep penetration to be held (Omidvar, Iskander, and Bless, 2014). The deep penetration phenomenon is typically studied in many practical engineering problems, such as civil engineering. For example, the development of innovative compact probes to penetrate deeper into the subsurface of remote areas, such as extraterrestrial bodies, has been a challenge for more than a decade.

There are various methods for predicting the penetration of rigid projectiles into soil layers, including phenomenological theories, experimental approaches, analytical and numerical methods. In the phenomenological approach, most investigators assumed a polynomial velocity, V_p, dependent on the retarding force, F, on the projectile as (Omidvar, Malioche, Bless, and Iskander, 2015):

$$-F = -M\frac{dV_p}{dt} = AR + BV_p + \frac{1}{2}AC_D\rho_0 V_p^2 - mg, \tag{2.1}$$

where A and M are the projectile frontal area and mass, ρ_0 is the medium's density, C_D is the drag coefficient, and g is the gravity. Generally, the retarding force is considered as the summation of the first three terms, strength (AR), viscous effects (BV_p), and inertia ($1/2AC_D\rho_0 V_p^2$), while gravity force is ignored (Guzman, Iskander, Bless, and Qi, 2014).

In the analytical and semi-analytical approaches, the cavity expansion theory has been

used for the modeling of penetrations into different target materials. This approach goes back to (Bishop, Hill, and Mott, 1945), where a theoretical framework was developed to evaluate the required quasi-static pressure for expanding a cylindrical and spherical hole in a ductile material. Later, Hopkins (1960) developed the spherical cavity expansion for incompressible materials for quasi-static and dynamic motions. In addition, Forrestal and Luk (1988) developed the spherical cavity expansion theory based on the Hopkins model for compressible elastic-plastic solid materials by using the Tresca yield condition. Later, Warren and Forrestal (1998) was able to improve the spherical cavity expansion theory for solid materials by adding the effect of strain hardening and strain rate sensitivity. The model estimated the penetration into aluminum targets up to the velocity of 700 m/sec with good agreement with the available test results with striking velocities of 350-1200 m/sec. However, the assumption of a rigid projectile caused the model and test results to diverge at higher striking velocities (700-1200 m/sec). Subsequently, the spherical cavity expansion model was successfully employed in a dynamic Finite Element (FE) code (PRONTO 3D) to model oblique impacts and consider the bulging effects and deformation of the projectile at higher striking velocities. Coupling the solution with the FE code led to a more accurate calculation of penetration depth into the aluminum target, and the previous conspicuous deviation between the test results and the solution was addressed (Warren and Tabbara, 1997; Warren and Tabbara, 2000).

In case of geomaterials, for quasi-static solutions, the simple and practical methods developed by the cavity expansion theory make them desirable and applicable to geotechnical problems, such as in-situ soil testing, pile foundation, tunnelling in soil and rock and well-bore instability (Yu, 2000). For instance, Yu and Houlsby (1991) developed one of the most notable solutions for cavity expansion in dilatant elastic-plastic soils based on the Mohr-Coulomb yield criterion with a non-associated flow rule. Following that, many researchers implemented critical state soil models to account for strain-hardening or softening models during cavity expansion for both drained and undrained conditions (Chen and Abousleiman, 2013; Chen and Abousleiman, 2012; Mo and Yu, 2017; Mo and Yu, 2018). Recently, Martinez, DeJong, Jaeger, and Khosravi (2020) employed the cavity expansion analysis code ASCEND based on the model presented in Chen and Abousleiman, 2013; Chen and Abousleiman, 2012 for quasi-static equilibrium conditions to obtain the required dimensions and self-burrowing potential of an idealized bio-inspired penetrometer with a radially expanding shaft and a penetrating tip in different soil types.

With regard to dynamic solutions for geomaterials subject to impact, Longcope Jr (1990),

and Longcope and Forrestal (1983) used the cavity expansion with the linear-pressure volumetric model to obtain the stresses on the projectile nose for penetration into rock and hard geological targets. Similarly, Forrestal and Luk (1992) used the locked hydrostat plastic assumption with an incompressible elastic region to simulate penetration into soil targets. In these works, they assumed a Mohr-Coulomb pressure-dependent failure condition in the plastic region:

$$\sigma_r - \sigma_\theta = \mu p + \tau_0, \tag{2.2}$$

where μ and τ_0 are constants and p is the hydrostatic pressure. The pressure-dependent failure criterion, as presented in the above equation, has been widely used in the cavity expansion models to provide a dynamic solution for hard target materials (rocks and concrete) subject to projectile impact to obtain the deceleration rates and penetration depth. For instance, Forrestal and Tzou (1997) used the uniform spherical cavity expansion theory, the pressure-dependent failure equation, and a linear pressure-volumetric strain model to obtain the stresses on the cavity wall for concrete targets. They developed the elastic-plastic and elastic-cracked-plastic models to obtain the radial stresses on the projectile. They observed a reasonable agreement between their models with the compressible assumption and the available test data, especially with the striking velocity below 800 m/sec. The solution derived by (Forrestal and Tzou, 1997) was then coupled with the explicit dynamics, finite element computer program PRONTO 3D to account for projectile deformation and oblique impacts into geological targets (Jung, Longcope, and Tabbara, 1999). There were good agreements between the test data (oblique impacts into frozen soil) and the estimated projectile rotation, penetration depth, and acceleration. In addition, Macek and Duffey (2000) developed a finite spherical cavity expansion model coupled with a finite element code using the Mohr-Coulomb pressure-dependent plasticity model to estimate the near-surface effects and layering in the case of normal and oblique impacts into soils and rocks. Next, He, Wen, and Guo (2011) used the same pressure-dependent failure criterion (Equation 2.2) but changed the plastic region to a comminuted one where the target material is granular or pulverized. They developed a dilatant-kinematic relation and used a parameter (k) that can be selected to transform the modelling of this region from the compaction one as the result of pore collapse by hydrostatic pressure to the dilation one in consequence of distortion deformation (shear cracking) and tensile failure. In their model, $k > 2$ is for compressible materials, $k < 2$ is for the materials in dilation state, and $k = 2$ is for the incompressible state. They proposed that the k-parameter should

be obtained empirically, and they observed for the concrete, the value of $k = 1.7$ in the model is in good agreement with the same test data reported in (Forrestal and Tzou, 1997). Anwer Khan (2015) employed the spherical cavity expansion method using the locked hydrostatic model and defined a different load distribution on the projectile, where the minimum load is at the tip of the nose, to modify the model estimation of penetration into non-cohesive soil targets under dry, saturated, and compacted conditions for a low striking velocity (14 m/sec). Kotov, Linnik, and Sabaeva (2021) recently used Equation 2.2 and Tresca yield criterion to derive a closed-form solution for the cavity expansion problem in a rigid-plastic (neglecting the elastic precursor) medium under a shock wave with an incompressible assumption behind the wavefront. They suggested that the proposed solution can be employed to evaluate stresses on a high-velocity rigid projectile penetrating into a low-strength soil media. The advantage of the above analytical methods is that they directly link the penetration and stresses on the projectile to the mechanical properties of target medium. At the same time, it eliminates the need to develop a contact algorithm for the discrete medium. Therefore, they are much more computationally convenient for designing and engineering as well as benchmarking purposes.

It is worth noting that none of the above-mentioned closed-form or semi-analytical solutions employed the dynamic cavity expansion theory explicitly in terms of friction angle and cohesion parameters. However, for most geomaterials, including lunar regolith simulants, the Mohr-Colomb criterion parameters are available or can be obtained in conventional geotechnical tests in the form of the friction angle and cohesion parameters. Accordingly, instead of Equation 2.2, the Mohr-Coulomb failure criterion can be written as, (Labuz and Zang, 2012):

$$\sigma_I - \sigma_{III} = (\sigma_I + \sigma_{III})\sin(\phi_f) + 2C_{oh}\cos(\phi_f), \tag{2.3}$$

where σ_I and σ_{III} are the major and minor principal stresses, respectively, and C_{oh} is cohesion and ϕ_f is the angle of internal friction. Using Equation 2.3 instead of Equation 2.2 results in the solution which is more desirable for engineering application. Accordingly, here, we employ the Mohr-Coulomb criterion in the more commonly available form for geological materials failure (Equation 2.3) to represent the plastic region by considering the target material as a compressible medium.

Moreover, we aim to modify the locked hydrostat model presented by Forrestal and Luk (1992). In the previous model, the locked hydrostat density was constant for all

velocities of impact. But, in the current study, it is related to the striking velocity. The developed models based on the spherical cavity expansion theory are used to predict the deceleration rate and final penetration depth of a rigid projectile probe into geological targets under the perpendicular impact. Also, the emphasis of this study will be on the subsonic velocity ranges of impact, which is most likely the case in planetary low gravity conditions. For instance, the impact velocity of around or lower than 285 m/sec can be achieved by free-fall, if the projectile is launched from a lunar orbiter or lander at 25 km to the surface of the Moon. In addition, it is expected that the subsonic impact will be low enough to prevent high shock wave propagation in the probes, bulging, structural damage and probe deformation and damage the sensors or navigating system. The developed equations can be used to estimate and assess the stresses on compact projectile probes and final penetration depth.

2.2 Mathematical Developments

Here, we first present the governing equations and Mohr-Coulomb criteria. Then, the governing equations for the elastic region are solved. Subsequently, the governing equations for the plastic region are derived under two assumptions: (i) the locked hydrostat plastic region model is used, where it is assumed that the granular particles in the near vicinity of the projectile become completely close together due to the impact pressure and the kinetic energy of the projectile. Subsequently, the incompressible solution can be obtained from this general solution as a special case. Then, the modified locked hydrostat model will be developed for the case that the cavity velocity is not enough to create the fully locked plastic region. (ii) we assume that a linear volumetric pressure exists in the plastic region. Based on the developed models, we can estimate the stresses on the projectile nose, obtain the retarding force, and predict its resting position (final penetration depth) after the impact.

2.2.1 Cavity Expansion Model

We assume that the projectile probe impacts the granular medium with the initial vertical velocity of V_{p_0} and continues to penetrate into the medium as a rigid-body with a decreasing velocity of V_p. In the spherical cavity expansion model proposed by (Longcope Jr, 1990), it is assumed that a spherically symmetric cavity develops from an initial radius, $r_0 = 0$, with a uniform velocity of V_c to assist the probe penetration (Figure 2.1). Then, there is a plastic

region surrounding the inner cavity area, $r = V_c t$, and surrounded by the outer elastic region, $r = c_p t$, where c_p is the elastic-plastic interface speed, t is time, and r is the radial spherical coordinate. Finally, the elastic region is defined between $r = c_p t$, and $r = c_e t$, where c_e is the elastic wave speed. The elastic-plastic and elastic wave speeds are obtained by the following equations (Zukas, 2004):

$$c_p = \sqrt{\frac{1}{\rho_0}\frac{d\sigma}{d\epsilon}}, c_e^2 = \frac{E(1-\nu)}{(1+\nu)(1-2\nu)\rho_0}, \tag{2.4}$$

in which ν, E and ρ_0 are Poisson's ratio, Young's modulus and initial density of the granular medium, respectively. $d\sigma/d\epsilon$ is the slope of the stress-strain curve; therefore, c_p depends on the cavity expansion velocity.

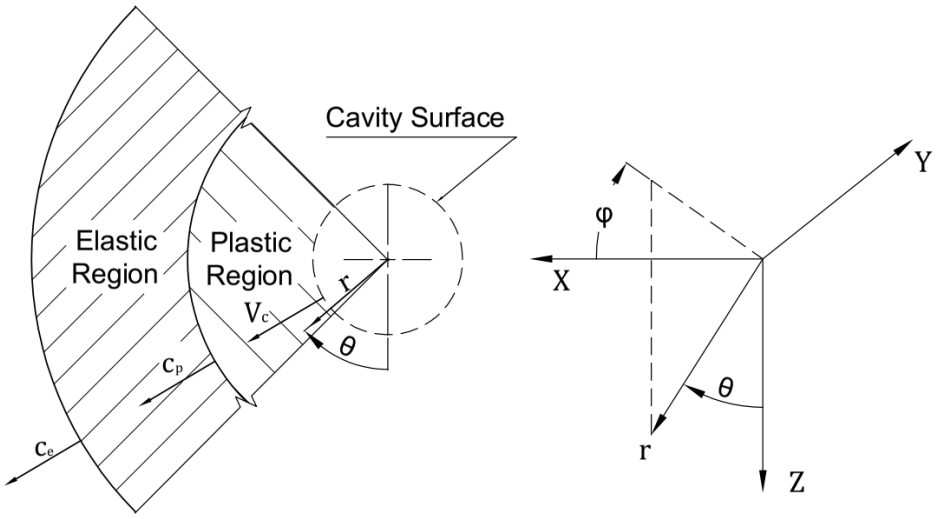

FIGURE 2.1: Response regions.

In the symmetrical spherical Eulerian coordinate system, the equation for conservation of momentum in the r direction is as follows (Cantwell, 2014):

$$\frac{\partial \sigma_r}{\partial r} + 2\frac{(\sigma_r - \sigma_\theta)}{r} = -\rho\left(\frac{\partial v}{\partial t} + v\frac{\partial v}{\partial r}\right), \tag{2.5}$$

where v is the radial particle velocity, σ_r and σ_θ are the stress components in the spherical coordinate system (positive in compression). The first term on the right-hand side of Equation 2.5 is due to local acceleration and the second term corresponds to the convective acceleration of particles.

The equation for conservation of mass is (Pritchard and Mitchell, 2016):

$$\nabla.\rho\vec{V} + \frac{\partial \rho}{\partial t} = 0,$$

where $\vec{V}$ is the particle velocity field with the radial component of v. In the symmetrical spherical coordinate system, $\vec{V}$ only has the non-zero radial component (v); subsequently, we can rewrite the equation for conservation of mass as follows:

$$\rho\left(\frac{\partial v}{\partial r}+\frac{2v}{r}\right)+\frac{\partial \rho}{\partial t}+v\frac{\partial \rho}{\partial r}=0. \tag{2.6}$$

Moreover, the Mohr-Coulomb failure criterion (Equation 2.3) in the spherical coordinate system can be written as:

$$\sigma_r-\sigma_\theta=(\sigma_r+\sigma_\theta)\sin(\phi_f)+2C_{oh}\cos(\phi_f), \tag{2.7}$$

In the symmetrical spherical coordinate, the hydrostatic pressure has the following relation to the normal stresses:

$$p=\frac{\sigma_r+2\sigma_\theta}{3}, \qquad \sigma_\theta=\sigma_\varphi, \tag{2.8}$$

Consequently, by rearranging Equation 2.7 we can derive the following expressions for σ_θ, $\sigma_r-\sigma_\theta$, and p:

$$\sigma_\theta=\frac{-2C_{oh}\cos\left(\phi_f\right)-\sigma_r\sin\left(\phi_f\right)+\sigma_r}{\sin\left(\phi_f\right)+1}, \tag{2.9a}$$

$$Y=\sigma_r-\sigma_\theta=\frac{2\left(C_{oh}\cos\left(\phi_f\right)+\sigma_r\sin\left(\phi_f\right)\right)}{\sin\left(\phi_f\right)+1}, \tag{2.9b}$$

$$p=\frac{-4C_{\mathrm{oh}}\cos\left(\phi_f\right)-\sigma_r\sin\left(\phi_f\right)+3\sigma_r}{3\sin\left(\phi_f\right)+3}. \tag{2.9c}$$

where $Y=\sigma_r-\sigma_\theta$ becomes a constant when the friction angle is zero, and it shows the Tresca criterion.

2.2.1.1 Elastic Region

In the symmetrical spherical coordinate system, for the elastic region, we have (Slaughter, 2012; Bower, 2009):

$$\epsilon_r=\frac{\partial u_r}{\partial r}, \qquad \epsilon_\theta=\epsilon_\phi=\frac{u_r}{r},$$

$$\sigma_r=\frac{-E}{(1+\nu)(1-2\nu)}\left((1-\nu)\epsilon_r+2\nu\epsilon_\theta\right), \qquad \sigma_\theta=\sigma_\phi=\frac{-E}{(1+\nu)(1-2\nu)}(\epsilon_\theta+\nu\epsilon_r),$$

where the stress components are positive in compression, ϵ_r, ϵ_θ and ϵ_ϕ are the strain components, and u_r is the radial displacement. Combining these equations results in the

following expressions for the stress components:

$$\begin{aligned}\sigma_r &= \frac{-E}{(1+\nu)(1-2\nu)}\left((1-\nu)\frac{\partial u_r}{\partial r}+2\nu\frac{u_r}{r}\right),\\ \sigma_\theta = \sigma_\phi &= \frac{-E}{(1+\nu)(1-2\nu)}\left(\frac{u_r}{r}+\nu\frac{\partial u_r}{\partial r}\right).\end{aligned} \tag{2.10}$$

By replacing Equation 2.10 into Equation 2.5, and since the region is far away from the cavity wall and displacements are infinitesimal, we can ignore the convective acceleration term to derive the following wave equation for the elastic region:

$$\frac{\partial^2 u_r}{\partial r^2}+\frac{2}{r}\frac{\partial u_r}{\partial r}-\frac{2}{r^2}u_r=\frac{1}{c_e^2}\frac{\partial^2 u_r}{\partial t^2}. \tag{2.11}$$

By assuming a uniform cavity expansion and employing $\zeta = r/c_p t$ and a dimensionless variable $\tilde{u}(\zeta) = u_r/c_p t$ (Longcope and Forrestal, 1983), we can derive the following ordinary differential equation from Equation 2.11:

$$\tilde{u}''(\zeta)\left(1-\frac{\zeta^2 c_p^2}{c_e^2}\right)-\frac{2\tilde{u}(\zeta)}{\zeta^2}+\frac{2\tilde{u}'(\zeta)}{\zeta}=0. \tag{2.12}$$

The closed-form solution for Equation 2.12 can be derived as follows:

$$\tilde{u}=A\zeta+B\frac{\left(3c_p^2\zeta^2-c_e^2\right)}{3\zeta^2}, \tag{2.13}$$

where A and B depend on the boundary conditions. At the elastic wavefront, $r = c_e t$, the radial displacement is zero, $u_r = 0$. In terms of the dimensionless variables, it results in

$$\tilde{u}(\zeta = c_e/c_p) = 0, \tag{2.14}$$

where it can be written as the following equation by using Equation 2.13:

$$\frac{Ac_e}{c_p}+\frac{2Bc_p^2}{3}=0. \tag{2.15}$$

At the elastic-plastic interface, $r = c_p t$ and $\zeta = 1$, we combine Equation 2.10 and Equation 2.13 to replace the resulting stresses in Equation 2.7 and obtain another equation:

$$\begin{aligned}\frac{BE\left(c_p^2-c_e^2\right)}{\nu+1} = \frac{E\sin\left(\phi_f\right)\left(6A(\nu+1)+B\left((1-2\nu)c_e^2+(6\nu+3)c_p^2\right)\right)}{3\left(2\nu^2+\nu-1\right)}\\ +2C_{\text{oh}}\cos\left(\phi_f\right).\end{aligned} \tag{2.16}$$

Therefore, A and B can be obtained by using Equation 2.15 and Equation 2.16 as follows:

$$A = -\frac{4(\nu+1)(2\nu-1)c_p^3 C_{oh}\cos(\phi_f)}{E(c_p-c_e)\left(\sin(\phi_f)\left((1-2\nu)c_e^2+c_p(c_e-2\nu c_e)+4(\nu+1)c_p^2\right)+3(2\nu-1)c_e(c_e+c_p)\right)}, \tag{2.17a}$$

$$B = \frac{6(\nu+1)(2\nu-1)c_e C_{oh}\cos(\phi_f)}{E(c_p-c_e)\left(\sin(\phi_f)\left((1-2\nu)c_e^2+c_p(c_e-2\nu c_e)+4(\nu+1)c_p^2\right)+3(2\nu-1)c_e(c_e+c_p)\right)}. \tag{2.17b}$$

Finally, having A and B, the stresses in the elastic region can be calculated as follows:

$$S(\zeta) = \frac{\sigma_r}{E} = \frac{3A\zeta^3(\nu+1)+2B\left((1-2\nu)c_e^2+3\zeta^2\nu c_p^2\right)}{3\zeta^3(2\nu^2+\nu-1)}, \qquad 1<\zeta<c_e/c_p, \tag{2.18a}$$

$$\frac{\sigma_\theta}{E} = \frac{3A\zeta^3(\nu+1)+B\left((2\nu-1)c_e^2+3\zeta^2 c_p^2\right)}{3\zeta^3(2\nu^2+\nu-1)}, \qquad 1<\zeta<c_e/c_p. \tag{2.18b}$$

where $S(\zeta)$ is the dimensionless radial stress.

2.2.1.2 Plastic Region

For the plastic region, two assumptions are used and the solutions are derived accordingly, as follows:

2.1.2.1 Locked hydrostat plastic region (assumption 1): When the projectile collides and penetrates into the soil, the pressures generated at the cavity wall and the cavity wall velocity (projectile's kinetic energy) tend to compress and lock the soil particles in the near vicinity by the closure of the internal pores. Consequently, the further soil volume change by increasing pressure decreases as particle crushing and comminution required in the presence of very high cavity pressure. As the impact velocity increases, this region expands more rapidly in the target material. This plastic region model is called the locked hydrostat model, as suggested by Forrestal, Norwood, and Longcope (1981). The following equation relates the volumetric strain to density:

$$\eta^* = 1-\rho_0/\rho^*, \tag{2.19}$$

where η^* and ρ^* are the locked volumetric strain and density, respectively. For softer target material or very high impact velocity, the pressure created at the cavity wall surpasses the comminution strength of the particles in the target medium. In that case, it is expected that the voids be filled with crushed and pulverized materials so we can estimate the nearby material density by the density of soil solids. For harder target material, where the impact velocity is not high enough to start crushing particles, we estimate that the projectile kinetic

energy and the cavity pressure are enough to decrease the void ratio by just interlocking the nearby particles. By using Equation 2.19 and assuming the density is equal to ρ^* we can rewrite Equation 2.5 and Equation 2.6 as follows:

$$\frac{\partial \sigma_r}{\partial r} + 2\frac{Y}{r} + \frac{\rho_0}{1-\eta^*}\left(\frac{\partial v}{\partial t} + v\frac{\partial v}{\partial r}\right) = 0, \tag{2.20a}$$

$$\frac{2v}{r} + \frac{\partial v}{\partial r} = 0. \tag{2.20b}$$

Similarly, we employ a dimensionless parameter $\zeta = r/c_p t$, dimensionless variables $S = \sigma_r/E$ and $U = v/c_p$, and Equation 2.9b to derive the following ordinary differential equations from the governing equations (Equation 2.20):

$$\frac{4C_{oh}\cos\left(\phi_f\right) + 4ES(\zeta)\sin\left(\phi_f\right)}{E\zeta\sin\left(\phi_f\right) + E\zeta} + S'(\zeta) + \frac{\beta^2(\zeta - U(\zeta))U'(\zeta)}{\eta^* - 1} = 0, \tag{2.21a}$$

$$U'(\zeta) + \frac{2U(\zeta)}{\zeta} = 0, \tag{2.21b}$$

where $\beta = c_p/\alpha$ is a dimensionless parameter, and $\alpha = \sqrt{E/\rho_0}$ is known as the sound speed (for uniaxial stress (bar velocity)) in solid materials (Stronge, 2018). At the cavity wall, $r = V_c t$, we have $v = V_c$. Consequently, we can write the boundary condition for Equation 2.21b as follows:

$$U(\zeta = \psi) = \psi, \tag{2.22}$$

where $\psi = V_c/c_p$ is the non-dimensional cavity wall speed. By using the boundary condition at the cavity wall (Equation 2.22), the solution of Equation 2.21b is obtained as follows:

$$U(\zeta) = \frac{\psi^3}{\zeta^2}, \qquad \psi < \zeta < 1. \tag{2.23}$$

Then, by substituting Equation 2.23 into Equation 2.21a, the solution for the non-dimensional stress will be obtained as,

$$\begin{aligned} S(\zeta) = \frac{\sigma_r}{E} = &-\frac{C_{oh}\left(\cos\left(\phi_f\right) + \cot\left(\phi_f\right)\right)}{E\left(\sin\left(\phi_f\right) + 1\right)} + \frac{\beta^2\psi^6\left(\sin\left(\phi_f\right) + 1\right)}{2\zeta^4\left(\eta^* - 1\right)} \\ &+ \frac{2\beta^2\psi^3\left(\sin\left(\phi_f\right) + 1\right)}{\zeta\left(\eta^* - 1\right)\left(3\sin\left(\phi_f\right) - 1\right)} + S_0\zeta^{-\frac{4\sin\left(\phi_f\right)}{\sin\left(\phi_f\right)+1}}, \quad \psi < \zeta < 1, \quad \phi_f \neq 0. \end{aligned} \tag{2.24}$$

For the case when $\phi_f = 0$, the closed-form solution for the radial stress changes to the following one:

$$S(\zeta) = \frac{\beta^2\psi^3\left(\psi^3 - 4\zeta^3\right)}{2\zeta^4\left(\eta^* - 1\right)} - \frac{4C_{\text{oh}}\log(\zeta)}{E} + S_0, \qquad \psi < \zeta < 1, \qquad \phi_f = 0. \tag{2.25}$$

Subsequently, σ_θ is obtained from Equation 2.9a.

Compressible elastic region: For evaluating S_0 and c_p, we need the boundary conditions at the plastic-elastic interface. Since we have a jump in the density from ρ^* in the plastic region to ρ_0 in the elastic one, where the variation of density is negligible, we use Rankine–Hugoniot jump conditions for conservation of mass and momentum at the interface (Zukas, 2004; Luk and Forrestal, 1987):

$$\rho^*(v_p - c_p) = \rho_0(v_e - c_p), \tag{2.26}$$

$$\sigma_{rp} + \rho^* v_p(v_p - c_p) = \sigma_{re} + \rho_0 v_e(v_e - c_p). \tag{2.27}$$

Then, we use Equation 2.19 and non-dimensionless variables to write the jump equations as follows:

$$U(\zeta) = \eta^* + (1 - \eta^*)\frac{\partial}{\partial t}(t\tilde{u}(\zeta)), \qquad \zeta = 1, \tag{2.28}$$

$$S_p(\zeta) = S_e(\zeta) + \beta^2\left(\frac{\partial}{\partial t}(t\tilde{u}(\zeta)) - 1\right)\left(\frac{\partial}{\partial t}(t\tilde{u}(\zeta)) - U(\zeta)\right), \qquad \zeta = 1. \tag{2.29}$$

By replacing Equation 2.13 and Equation 2.23 into Equation 2.28 we can derive c_p as follows:

$$c_p = -\frac{V_c}{\sqrt[3]{B\left(\eta^* - 1\right)\left(c_p - c_e\right)\left(c_e + c_p\right) - \eta^*}}, \qquad \phi_f \neq 0, \tag{2.30a}$$

$$c_p = -\frac{V_c}{\sqrt[3]{\frac{2(\eta^*-1)(\nu+1)C_{\text{oh}}}{E} - \eta^*}}, \qquad \phi_f = 0, \tag{2.30b}$$

where B is obtained from Equation 2.17b. Equation 2.30a needs a numerical computation (trial and error) to evaluate c_p and Equation 2.30b can provide the initial guess for it. Similarly, by using Equation 2.18 and Equation 2.28, the second equation (Equation 2.29) leads to the following equation:

$$S_0 = \frac{3A(\nu+1)+2B\left((1-2\nu)c_e^2+3\nu c_p^2\right)}{3\left(2\nu^2+\nu-1\right)} + \beta^2\eta^*\left(B\left(c_e^2-c_p^2\right)+1\right)^2 + \frac{C_{\text{oh}}\cot\left(\phi_f\right)}{E} - \frac{\beta^2\psi^6\left(\sin\left(\phi_f\right)+1\right)}{2\left(\eta^*-1\right)} - \frac{2\beta^2\psi^3\left(\sin\left(\phi_f\right)+1\right)}{\left(\eta^*-1\right)\left(3\sin\left(\phi_f\right)-1\right)}. \tag{2.31}$$

For the case when $\phi_f = 0$, S_0 is:

$$S_0 = \frac{3A(\nu+1)+2B\left((1-2\nu)c_e^2+3\nu c_p^2\right)}{3\left(2\nu^2+\nu-1\right)} - \frac{\beta^2\left(\psi^3-4\right)\psi^3}{2\left(\eta^*-1\right)} + \beta^2\eta^*\left(B\left(c_e^2-c_p^2\right)+1\right)^2. \tag{2.32}$$

where A and B are obtained from Equation 2.17.

Incompressible elastic region: For the case of an incompressible elastic region (a simpler assumption), Equation 2.30 changes to the following equation by using Equation 2.4 and setting $\nu = 0.5$:

$$c_p = -\frac{V_c}{\sqrt[3]{-\frac{9(\eta^*-1)C_{\text{oh}}\cos\left(\phi_f\right)}{\sin\left(\phi_f\right)\left(18\rho c_p^2+E\right)-3E}-\eta^*}}, \qquad \phi_f \neq 0, \tag{2.33a}$$

$$c_p = -\frac{V_c}{\sqrt[3]{\frac{3(\eta^*-1)C_{\text{oh}}-E\eta^*}{E}}}, \qquad \phi_f = 0. \tag{2.33b}$$

Moreover, we can replace Equation 2.4 into Equation 2.31 and Equation 2.32, then calculate the limit when $\nu \to 0.5$ in both. The result of the incompressible elastic solution is as follows:

$$S_0 = \eta^*\left(\beta + \frac{9\beta C_{\text{oh}}\cos\left(\phi_f\right)}{\sin\left(\phi_f\right)\left(18\rho c_p^2+E\right)-3E}\right)^2 - \frac{2C_{\text{oh}}\cos\left(\phi_f\right)\left(9\rho c_p^2+2E\right)}{E\left(\sin\left(\phi_f\right)\left(18\rho c_p^2+E\right)-3E\right)} + \frac{C_{\text{oh}}\cot\left(\phi_f\right)}{E} - \frac{\beta^2\psi^3\left(\sin\left(\phi_f\right)+1\right)\left(3\psi^3\sin\left(\phi_f\right)-\psi^3+4\right)}{2\left(\eta^*-1\right)\left(3\sin\left(\phi_f\right)-1\right)}, \tag{2.34}$$

and when $\phi_f = 0$ we have:

$$S_0 = -\frac{\beta^2\left(\psi^3-4\right)\psi^3}{2\left(\eta^*-1\right)} + \frac{2C_{\text{oh}}\left(9\rho c_p^2+2E\right)}{3E^2} + \eta^*\left(\beta - \frac{3\beta C_{\text{oh}}}{E}\right)^2. \tag{2.35}$$

For using the above assumption, we need to have the locked hydrostat volumetric strain. However, the projectile velocity may not be sufficient enough to create a fully locked plastic region for the entire velocity range for some geological targets. In this case, for each cavity velocity, we define a modified volumetric strain by using the pressure-volume strain data ($\eta = f(p)$) in a trial and error procedure according to Figure 2.2. At first, for the

cavity velocity V_c, we guess the volumetric strain to obtain the cavity pressure by using Equation 2.29 and Equation 2.9c. Then, we use our pressure-volume strain data to obtain the volumetric strain at the calculated pressure and check the error.

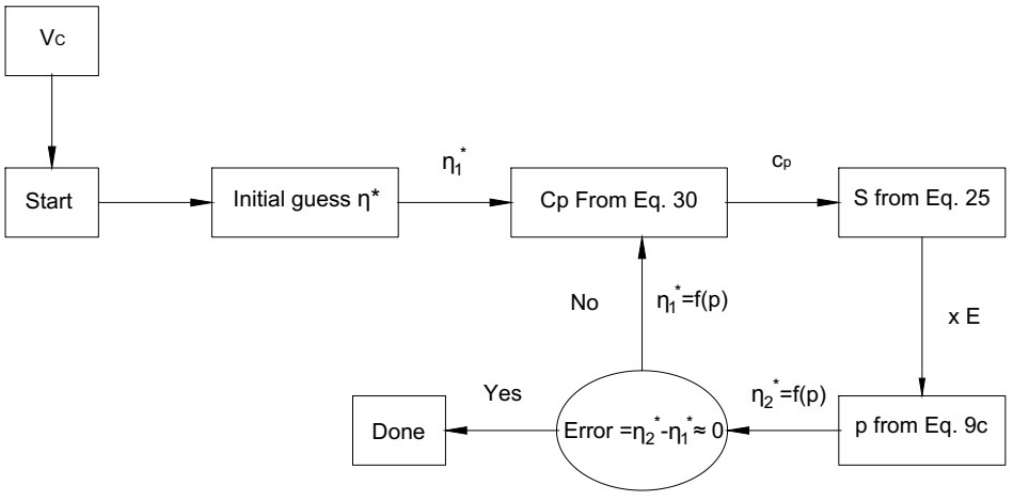

FIGURE 2.2: Modification of η^* for partially locked hydrostat plastic region.

2.1.2.2 Plastic region with a linear pressure-volumetric strain (assumption 2): Here, material description in the plastic region is represented by using Equation 2.7 and a linear pressure-volumetric strain relationship in spherical symmetry as follows (Forrestal and Luk, 1988):

$$p = K\eta = K(1 - \rho_0/\rho), \tag{2.36}$$

where ρ is the soil density in the plastic region, η is the volumetric strain, K is the bulk modulus, and p is the hydrostatic pressure. It is worth noting that $\sigma_r - \sigma_\theta$ (Equation 2.9b) and ρ, which is a function of p as indicated in Equation 2.36, can be replaced in the equation for conservation of momentum (Equation 2.5). Similarly, we can replace ρ and its derivatives in the equation for conservation of mass (Equation 2.6) by using Equation 2.9c and Equation 2.36. The resulting equations are as follows:

$$\frac{\partial \sigma_r}{\partial r} + 2\frac{Y}{r} + \frac{\rho_0}{1-\eta}\left(\frac{\partial v}{\partial t} + v\frac{\partial v}{\partial r}\right) = 0, \tag{2.37a}$$

$$\frac{2v}{r} + \frac{\partial v}{\partial r} + \frac{X}{1-\eta}\left(\frac{\partial \sigma_r}{\partial t} + v\frac{\partial \sigma_r}{\partial r}\right) = 0, \tag{2.37b}$$

where

$$X = \frac{3 - \sin\left(\phi_f\right)}{3K\left(\sin\left(\phi_f\right) + 1\right)}, \tag{2.38a}$$

$$Y = \sigma_r - \sigma_\theta = -\frac{6\left(C_{oh}\cos\left(\phi_f\right) + K\eta\sin\left(\phi_f\right)\right)}{\sin\left(\phi_f\right) - 3}. \tag{2.38b}$$

Then, assuming a uniform cavity expansion, we employ the similar parameter $\zeta = r/c_p t$ and dimensionless variables $S = \sigma_r/E$ and $U = v/c_p$ to derive the following ordinary differential equations from Equation 2.37 (Longcope Jr, 1990):

$$\frac{2Y}{\zeta E} + S'(\zeta) + \frac{\beta^2(\zeta - U(\zeta))U'(\zeta)}{\eta - 1} = 0, \tag{2.39a}$$

$$\frac{EX(\zeta - U(\zeta))S'(\zeta)}{\eta - 1} + U'(\zeta) + \frac{2U(\zeta)}{\zeta} = 0, \tag{2.39b}$$

where $\beta = c_p/\alpha$, and $\alpha = \sqrt{E/\rho_0}$ are the dimensionless parameters. Then, the continuity condition of the radial velocity and stresses at the elastic-plastic interface can be written as follows by using Equation 2.18a and Equation 2.13:

$$\frac{\partial}{\partial t}(t\tilde{u}(\zeta)) = U(\zeta) = B\left(c_p - c_e\right)\left(c_e + c_p\right), \qquad \zeta = 1, \tag{2.40a}$$

$$S(\zeta) = \frac{3A(\nu+1) + 2B\left((1-2\nu)c_e^2 + 3\nu c_p^2\right)}{3\left(2\nu^2 + \nu - 1\right)}, \qquad \zeta = 1. \tag{2.40b}$$

Linear solution: For the linear solution, we ignore the effects of the non-linear terms, e.g. the convective acceleration in the momentum equation ($v\partial v/\partial r$), the variation of density across the region ($v\partial\rho/\partial r$), and volumetric strain in Equation 2.37 and equivalent terms in Equation 2.39. We expect that the linear approximation in small impact velocities (subsonic velocities) works if $K\sin\left(\phi_f\right) < C_{\text{oh}}\cos\left(\phi_f\right)$, and therefore we can neglect η in Equation 2.38b. Subsequently, the linearized solution can be obtained as follows:

$$U(\zeta) = \frac{2\beta^2 BG(\zeta)\left(\beta^2 E - \rho_0 c_e^2\right) - (\zeta - 1)\rho_0 W\left(\beta^2 E\zeta X + 1\right)}{2\beta^2\zeta^2\rho_0\left(\beta^2 EX - 1\right)} - \frac{WG(\zeta)H(\zeta)}{2\beta^3\zeta^2\sqrt{EX}}, \qquad \psi < \zeta < 1, \tag{2.41a}$$

$$S(\zeta) = \frac{-2\beta^2 B\rho_0 c_e^2 + 2\beta^4 BE - \rho_0 W}{\zeta\rho_0 - \beta^2 E\zeta\rho_0 X} + \frac{WH(\zeta)}{\beta\zeta\sqrt{EX}} + \frac{1}{2}W\log\left(\frac{\zeta^2}{1 - \beta^2 E\zeta^2 X}\right) + S_0, \qquad \psi < \zeta < 1, \tag{2.41b}$$

where

$$W = \frac{12C_{oh}\cos\left(\phi_f\right)}{E\left(\sin\left(\phi_f\right)-3\right)}, \tag{2.42a}$$

$$H(\zeta) = \tanh^{-1}\left(\beta\sqrt{EX}\right) - \tanh^{-1}\left(\beta\zeta\sqrt{EX}\right), \tag{2.42b}$$

$$G(\zeta) = \beta^2 E\zeta^2 X - 1, \tag{2.42c}$$

$$S_0 = \frac{3A(\nu+1)+2B\left((1-2\nu)c_e^2+\frac{3\beta^2 E\nu}{\rho_0}\right)}{3\left(2\nu^2+\nu-1\right)} + \frac{2\beta^4 BE-\rho_0\left(2\beta^2 Bc_e^2+W\right)}{\rho_0\left(\beta^2 EX-1\right)} + \frac{1}{2}W\log\left(1-\beta^2 EX\right). \tag{2.42d}$$

By using the boundary condition at the cavity wall (Equation 2.22), we can obtain the following equation to calculate c_p numerically:

$$G\left(\frac{V_c}{c_p}\right)\left(2B\rho_0 Xc_p^3\left(c_p-c_e\right)\left(c_e+c_p\right)+W\sqrt{\frac{E}{\rho_0}}\sqrt{EX}H\left(\frac{V_c}{c_p}\right)\left(1-\rho_0 Xc_p^2\right)\right)+ X\left(\rho_0 V_c\left(EWXc_p\left(c_p-V_c\right)+2V_c^2\right)+EW\left(c_p-V_c\right)-2\rho_0^2 V_c^3 Xc_p^2\right)=0 \tag{2.43}$$

Non-linear solution: Now, we consider the effects of convective acceleration and variation of density through the plastic medium in Equation 2.39. Moreover, volumetric strain can be written as a function of radial stress by using Equation 2.9c and Equation 2.36. Then, after some algebraic manipulations, we can derive the following ordinary differential equations from the governing equations (Equation 2.39):

$$S'(\zeta) - \frac{3\beta^2 K(\zeta-U(\zeta))\left(\sin\left(\phi_f\right)+1\right)U'(\zeta)}{4C_{oh}\cos\left(\phi_f\right)+ES(\zeta)\left(\sin\left(\phi_f\right)-3\right)+3K\left(\sin\left(\phi_f\right)+1\right)} + \frac{4C_{oh}\cos\left(\phi_f\right)+4ES(\zeta)\sin\left(\phi_f\right)}{E\zeta\sin\left(\phi_f\right)+E\zeta} = 0, \tag{2.44a}$$

$$-\frac{3EKX(\zeta-U(\zeta))\left(\sin\left(\phi_f\right)+1\right)S'(\zeta)}{4C_{oh}\cos\left(\phi_f\right)+ES(\zeta)\left(\sin\left(\phi_f\right)-3\right)+3K\left(\sin\left(\phi_f\right)+1\right)} + U'(\zeta)+\frac{2U(\zeta)}{\zeta} = 0. \tag{2.44b}$$

We need to have c_p before processing the solution. Regarding the non-linear nature of the added terms, it is necessary to choose a close initial estimation to obtain the accurate value for c_p in a converging trial and error procedure. Therefore, we derive an approximation for c_p by the linear method (neglecting the non-linear terms), solve Equation 2.43, then numerically solve Equation 2.44 with its boundary conditions (Equation 2.40). Next, we again evaluate the updated c_p by using the following equation at the cavity interface:

$$c_p = \kappa\frac{V_c}{U(\zeta=V_c/c_p)} + (1-\kappa)c_p, \qquad 0<\kappa<0.5 \tag{2.45}$$

where κ is a constant between 0 and 0.5. This range gives different convergence rates; subsequently, repeating the procedure leads to an accurate value for the interface velocity, stresses, and displacements.

2.2.2 Geometry of the Projectile Probe Nose

Figure 2.3 shows the schematic of possible geometries for the nose of projectile probes: conical- and ogival-shaped nose. For the conical nose illustrated in Figure 2.3a, γ is the probe cone angle. For the ogival nose, illustrated in Figure 2.3b, s is the radius of curvature, and the calibre-radius-head (CRH) and ϕ are defined as

$$CRH = \frac{s}{2a}, \tag{2.46}$$

$$\phi_0 \leq \phi \leq \pi/2, \qquad \phi_0 = sin^{-1}(\frac{s-a}{s}), \tag{2.47}$$

where $2a$ is the diameter of the probe. For the conical nose, we have:

$$\phi = \frac{\pi - \gamma}{2}, \tag{2.48}$$

where γ is the cone angle of the probe (Figure 2.3a).

In the cavity expansion model, it is assumed that the normal stress on the probe nose results from the stress required for the cavity expansion at the cavity wall, σ_r, and the frictional stress between the probe and soil is $\mu\sigma_r$ where μ is the sliding friction coefficient (Longcope Jr, 1990). As a result of the normal stress on the nose, the cavity expands with $V_c = V_p cos(\phi)$, where V_p is the probe's velocity (Figure 2.3).

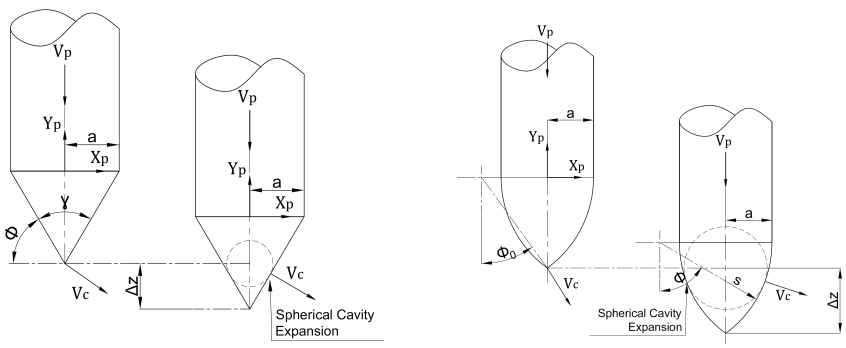

(A) Conical nose probe (B) Ogival nose probe

FIGURE 2.3: Nose geometry

Therefore, the resulting retarding axial force (F_p) on the conical probe nose and acceleration (a_p) will be:

$$a_p = -\frac{F_p}{M} = \frac{-E}{M}\int_{r=0}^{r=a} S(\frac{V_p\cos(\phi)}{c_p})(cos(\phi)+\mu sin(\phi))\frac{2\pi r}{cos(\phi)}dr = \frac{-E}{M}\pi a^2(\mu\tan(\phi)+1)S(\frac{V_p\cos(\phi)}{c_p}), \tag{2.49}$$

where M is the mass of the probe. Similarly, for the ogival nose, we can obtain the following equation:

$$a_p = -\frac{F_p}{M} = \frac{-E}{M}\int_{\phi_0}^{\frac{\pi}{2}} 2\pi s^2\left(\sin(\phi)-\frac{s-a}{s}\right)(\mu\sin(\phi)+\cos(\phi))S\left(\frac{V_p\cos(\phi)}{c_p}\right)d\phi. \tag{2.50}$$

By substituting the radial stress at the cavity wall, $S(\zeta = V_p cos(\phi)/c_p)$, the retarding acceleration of the probe will be obtained. Consequently, the penetration depth, z, can be calculated by the following integral:

$$z(V_p) = \int_{V_{p_0}}^{Vp}\frac{V_p}{a_p}dV_p, \tag{2.51}$$

where V_{p_0} is the initial impact velocity, and by setting $V_p = 0$, the total penetration is obtained.

2.3 Computational Procedure

The analytical models developed in the previous section are implemented in a Mathematica code called PESCE (Alaei Varnosfaderani, Maghoul, and Wu, 2021). Radial stresses on the probe nose have been evaluated to simulate the probe's motion penetrating into the granular medium (Equation 2.51). We used the obtained closed-form solutions for the radial stresses in subsection 2.1.2.1 for the locked hydrostat plastic region assumption (Assumption 1). Also, for the linear pressure-volumetric strain assumption (Assumption 2), the obtained closed-form solution (Equation 2.41b) is used when we neglect the non-linear terms. However, in the numerical result, when the non-linear terms are included in the governing equations (Equation 2.44), the equations proceeded numerically. Therefore, we rewrite Equation 2.44 in the form of $dy/d\zeta = f(\zeta, y)$ to implement the classic Runge–Kutta method (RK4). Our code starts the solution at the end of the interval, the elastic-plastic interface, to obtain the stresses at the cavity wall. By having the stress at the cavity wall, we can calculate the probe's motion using Equation 2.49, Equation 2.50, and Equation 2.51. Figure 2.4 shows the recommended flowchart for this numerical procedure. Alternatively, suppose we have enough data for lower cavity velocities. In that case, instead of using

the linear solution (Equation 2.43), we can extrapolate data to a near higher cavity velocity and find an approximation for c_p. Then start the nonlinear solution and the trial and error procedure. Once we know the numerical solution for $S(V_p)$, we can solve Equation 2.49 or Equation 2.50 numerically to calculate the acceleration and Equation 2.51 to evaluate the penetration depth. Alternatively, we fit a proper least-square polynomial function for the evaluated numerical solution ($S(V_p)$) to obtain a closed-form solution for acceleration and penetration depth. We observed that if we fit fourth-order polynomial least square functions, the coefficients of determination are above 0.99 in all simulations. At the same time, the maximum errors between the evaluated data and the fitted functions for the stress on the cavity wall are below 7%. Therefore, to maintain consistency, we fitted fourth-order polynomial functions in all sections of the numerical results.

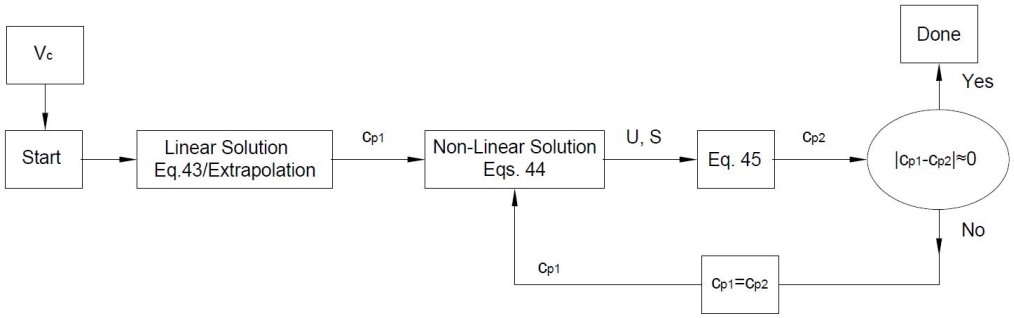

FIGURE 2.4: Non-linear solution flowchart for linear pressure-volumetric strain assumption.

2.4 Results and Discussion

In this section, the implemented models presented in subsection 2.2.1 are used to study the penetration of a rigid projectile probe into different geological and granular materials. Finally, the penetration of LUNAR-A into the lunar regolith will be discussed.

2.4.1 Radial stress in a three-layered soil medium

Forrestal and Luk (1992) used the pressure-dependent failure model (Equation 2.2) and locked hydrostat condition along with incompressible elastic assumption to simulate the penetration into soil targets. In the penetration test, located at a site called Antelope Lake at the Sandia Tonopah Test Range in Nevada, the average properties of the three-layered soil medium are reported as follows: ρ_0 =1860 Kg/m^3, E =160 MPa, Y =10 MPa, η^* =0.13, K =240 MPa (estimated from the pressure-volumetric strain diagram) (Forrestal and Luk,

1992). As we can see, they used the Tresca criterion in their numerical result, and again similarly, we set our model for $\phi_f = 0$ and $C_{oh} = Y/2$. For this target material, soil, the shear strength becomes a constant value for sufficiently high pressures (Forrestal and Luk, 1992). The minimum pressure in their triaxial test was 10 MPa, and the minimum pressure on the cavity wall ($V_c = 0$) for the locked hydrostat model is $p = \sigma_r - 2Y/3$ =10.33 MPa using the Tresca criterion (Figure 2.5). Accordingly, the Tresca criterion for modelling the plastic region seems appropriate. Moreover, based on the pressure volumetric strain data in (Forrestal and Luk, 1992), we can assume that the cavity pressure and projectile's kinetic energy are high enough to estimate $\eta^* = 0.13$ for all velocities.

Figure 2.5 compares the radial stresses at the cavity wall for different cavity expansion velocities, V_c, and models. The results show that, in lower velocities, the solutions for Assumption 2 are not sensitive to the non-linear effects of convective acceleration and variation of density through the plastic medium. The solutions labeled as *Assumption 2: Linear* in Figure 2.5 indicates the radial stresses when the non-linear terms are removed from the governing equations for Assumption 2 while *Assumption 2: Non-Linear* presents the solutions when the non-linear terms are considered. However, at high velocities, non-linear terms such as convective acceleration and density variation through the plastic medium significantly affect the results. Similarly, in low velocities, the solutions for Assumption 1 when the elastic medium is assumed incompressible are close to the ones when the elastic medium is assumed compressible. The difference between these two models becomes more evident in higher velocities, leading to predict higher radial stresses on the probe's nose when the elastic medium is assumed incompressible.

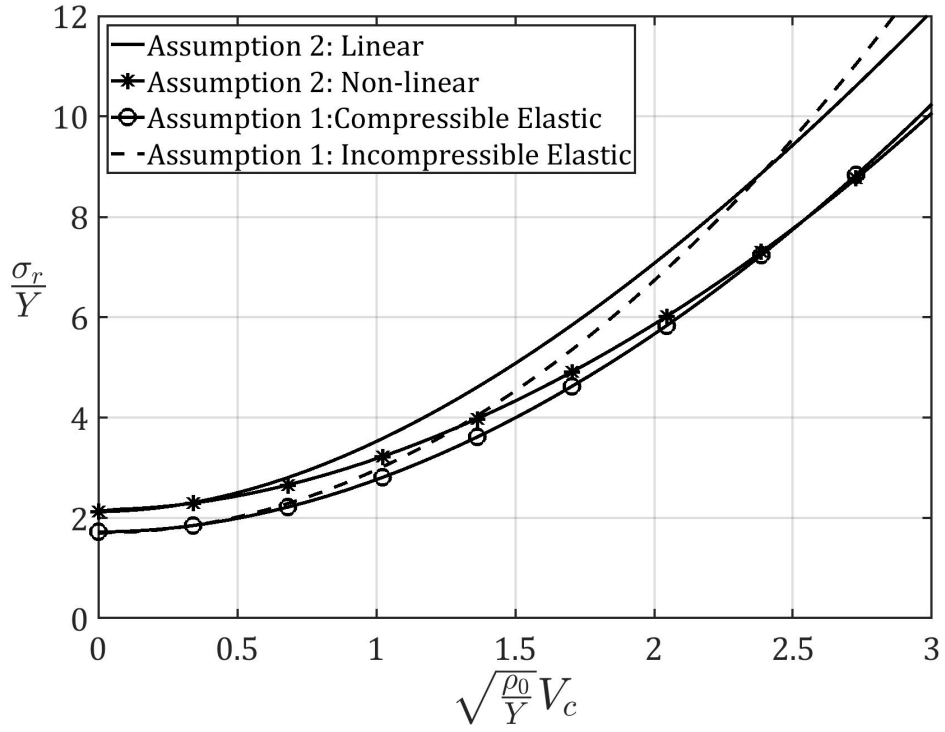

FIGURE 2.5: Radial stress at the cavity wall for a three-layered soil medium

Next, we used the radial stress at the cavity wall as presented in Figure 2.5 to predict the penetration depth of an ogival rigid projectile ($CRH = 3$) with a mass of 23.1 Kg and an initial impact velocity of V_{p_0} =280 m/sec (Forrestal and Luk, 1992) by different models presented in this study. Forrestal and Luk (1992) did not observe any nose erosion in their test, and therefore they set $\mu = 0$ for the modelling. Before using Equation 2.51 to calculate the probe's acceleration and the penetration depth, we noticed that the fourth-order polynomial least square functions perfectly match the radial stresses at the cavity wall for each model shown in Figure 2.5. Using a fitted fourth-order polynomial least square function facilitates the integration process, and it enables us to find a closed-form solution for the probe's acceleration and the penetration depth. Subsequently, using the fitted functions, we can obtain the probe's acceleration for each model by using Equation 2.50 as the following:

$$a_h(V_p) = -5300.97 - 0.197V_p - 0.066V_p^2 + 0.000021V_p^3 - 1.083 \times 10^{-8}V_p^4, \tag{2.52}$$

$$a_{hi}(V_p) = -5245.07 + 2.11 \times 10^{-14}V_p - 0.077V_p^2 + 1.26 \times 10^{-19}V_p^3 - 1.07 \times 10^{-22}V_p^4, \tag{2.53}$$

$$a_{NV}(V_p) = -6601.51 - 1.31V_p - 0.062V_p^2 + 0.000031V_p^3 - 2.33 \times 10^{-8}V_p^4, \tag{2.54}$$

where a_h, a_{hi}, and a_{NV} are the acceleration of the projectile obtained by Assumption 1,

Assumption 1 with incompressible elastic, and Assumption 2 including non-linear terms. If we ignore the higher-order terms in the above equations in lower velocities (V_p^3 and V_p^4), the obtained accelerations will be in the form of Equation 2.1. Moreover, if we only consider the constant and V_p^2 terms in a_{hi}, as the other terms have very small coefficients in comparison, the resulting equation would be in the format of Poncelet Penetration Equation. Now, by using Equation 2.51, the predicted penetration depth can be obtained. In Table 2.1, different models are used to estimate the penetration depth in the three-layered soil medium.

Model	Expected penetration
Assumption 1 by assuming compressible elastic	5.22 m
Assumption 1 by assuming incompressible elastic	4.98 m
Assumption 2	4.42 m

TABLE 2.1: Estimated penetration depth in a three-layered soil medium using different models.

Forrestal and Luk (1992) predicted the same penetration depth (4.98 m) by using the incompressible (elastic) locked hydrostat model. The reason is that the pressure-dependent failure model (Equation 2.2) and the Mohr-Columb criterion (Equation 2.7) lead to the Tresca plastic model where the shear strength is constant ($\sigma_r - \sigma_\theta = cte$). The actual penetration depth for a perpendicular impact is reported to be 4.98 m and 5.18 m for two tests with the angle of obliquity of 30°, and 5.02 m and 4.82 m for two tests with the yaw angle (angle between the projectile axis and projectile velocity) of 3.5° and 4°, respectively (Forrestal and Luk, 1992). If we disregard the test results where the yaw angle is not zero, the hydrostat model with both compressible and incompressible elastic assumptions give reasonable predictions of the penetration depth. The incompressible hydrostat model (Assumption 1 with incompressible elastic) obtained a lower penetration depth by estimating higher stresses at the cavity wall. However, in higher velocities, we can predict that the difference between these solutions becomes more conspicuous. The compressible semi-infinite elastic medium that surrounds the plastic region expects to mitigate stresses on the cavity wall more effectively than an incompressible one. Also, the result is compatible with (Warren and Forrestal, 1998) for compressible and incompressible solution. On the other hand, Assumption 2 seems to overestimate the projectile stresses since the resulting penetration depth is higher than the prediction obtained via Assumption 2.

Figure 2.6 shows the deceleration of the projectile estimated by different assumptions and two measured tests reported by Forrestal and Luk (1992). As we can expect from the estimated penetration depth, Assumption 2 leads to a higher estimation of the deceleration and shorter duration of the penetration. Figure 2.6 indicates that the deceleration declines to a nearly constant level and then jumps to its final value where the projectile has a small rebound and loses contact with the soil.

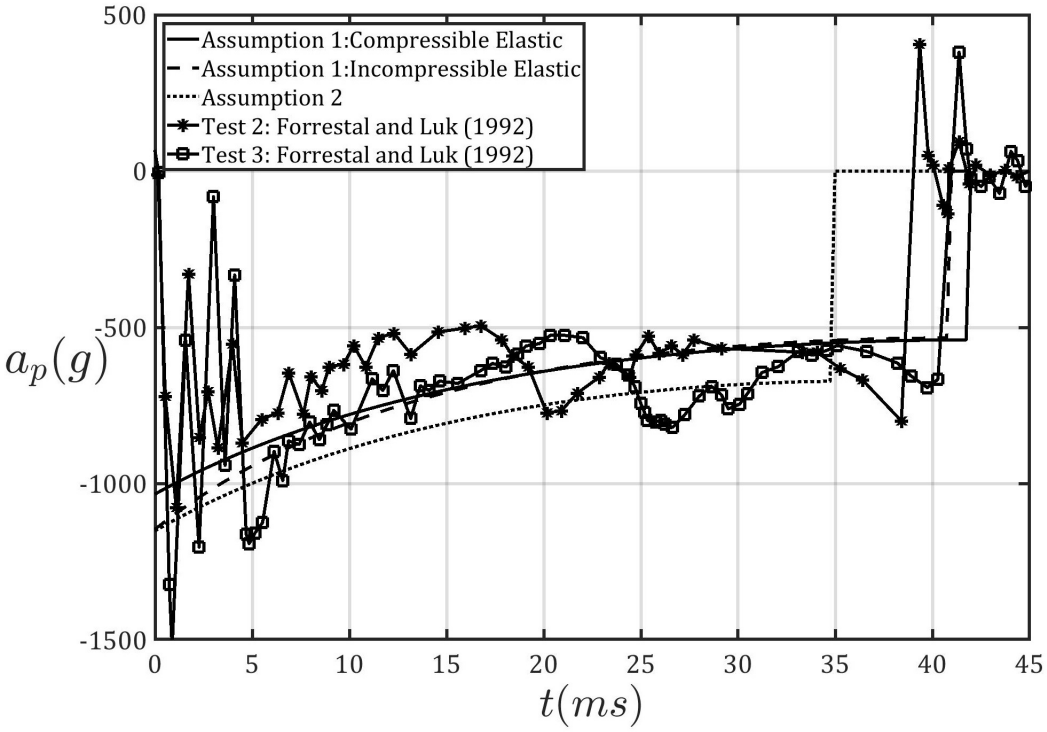

FIGURE 2.6: Deceleration of the projectile

2.4.2 Radial stress in a volcanic ash

Longcope and Forrestal (1983) used the plastic region's pressure-dependent failure model (Equation 2.2) for a kind of dry welded volcanic ash target named antelope tuff. They set $\mu = 1$ and τ_0=10 MPa to fit a line to the triaxial test data of the sample in the cylindrical coordinate, assuming circumferential stress and axial stress are equal. With the same assumptions, the equivalent Mohr-Columb parameters have been obtained by using Equation 2.7 and Equation 2.9c as $C_{oh} = 4.74$ MPa and $\phi_f = 25.38°$, which result in the same failure envelope (line) which is represented by Longcope and Forrestal (1983). Moreover, the pressure-volume strain data as presented in Longcope and Forrestal (1983) shows that at $\eta = 0.12$ around p =250 Mpa, the data has deviated conspicuously from the fitted line, which suggests that the medium's particles are getting very close to each other where further pressure leads to the start of comminution and strain hardening.

Post-analysis of the data (Figure 2.7) shows that in the desired subsonic velocity range, the cavity pressure is below 250 MPa. Therefore, we suggest that the projectile's kinetic energy and the pressure are just high enough to create a partially compacted plastic region in the vicinity of the projectile nose with $\eta^* \leq 0.12$, which is obtained by trial and error procedure desribed in Figure 2.2 and using Equation 2.36. The other reported properties of the medium are: ρ_0= 1620 Kg/m^3, ν =0.234, K = 2 GPa, E =3.192 GPa (calculated by bulk modulus and Poisson's ratio).

Figure 2.7 compares the normal stress at the cavity wall for different cavity expansion velocities, V_c, and models. Compared to the previous soil, there is a noticeable difference between the linear and non-linear solutions for Assumption 2. By looking at Equation 2.38b we can see that for this target material we cannot ignore $K\phi_f\eta$ in the numerator of Equation 2.38b even for small volumetric strain since we have $K\sin(\phi_f)/(C_{\text{oh}}\cos(\phi_f)) = 200$ while from the linear solution the lowest volumetric strain at the cavity wall (V_c=0) is around 0.01. Therefore, using the linear solution we obtain $K\eta\sin(\phi_f) > 2(C_{\text{oh}}\cos(\phi_f))$, which contradicts the initial assumption (ignoring η) in Equation 2.38b. Like the previous target material, Assumption 2 has predicted higher stresses at the cavity wall, but the difference is more conspicuous for antelope tuff.

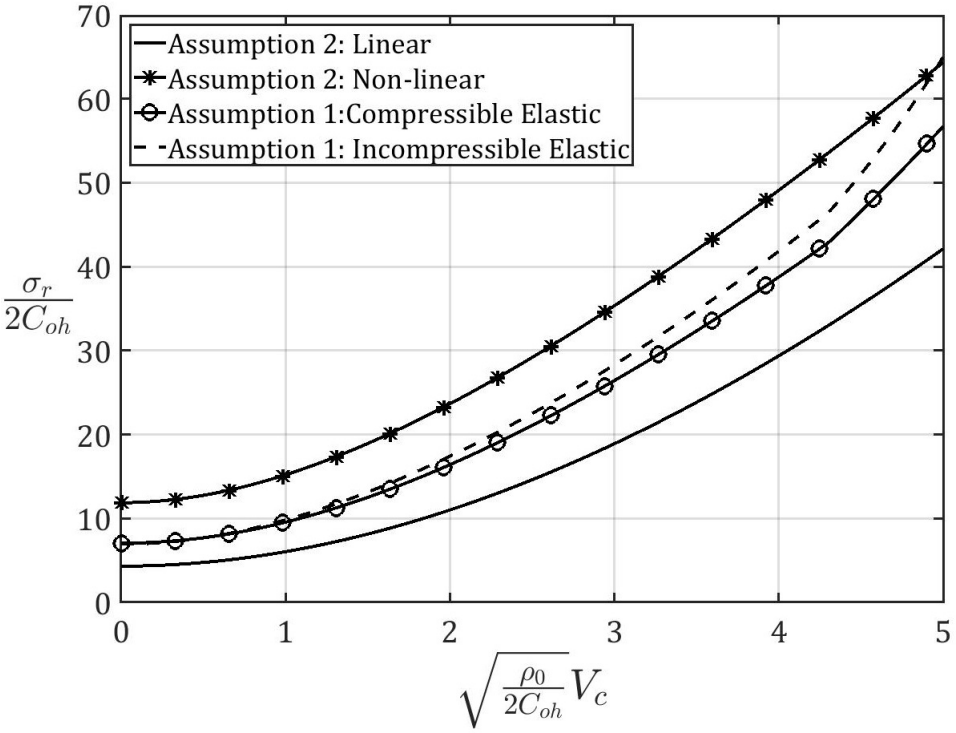

FIGURE 2.7: Radial stress at the cavity wall

The tested projectile (Longcope and Forrestal, 1983) was an ogival penetrator ($CRH = 6$,

$2a$ =0.156 m) with a mass of 162 Kg and an attached pusher plate of 55.3 Kg. At t=3 ms (during the early penetration phase), the pusher plate detached from the projectile, causing a jump in the recording acceleration (Longcope and Forrestal, 1983). For simplicity, at first, we neglect the effect of the pusher plate. The impact velocity was 520 m/sec. Similar to the previous test, the effect of sliding friction was neglected ($\mu = 0$) (Longcope and Forrestal, 1983). Again, the fourth-order polynomial least square functions are used to represent the radial stresses at the cavity wall in Figure 2.7. Using the fitted functions, we can obtain the projectile's acceleration for each model by using Equation 2.50. Similarly, by using Equation 2.51, the predicted penetration depth are calculated. Table 2.2 compares different models for estimating penetration depth in this medium.

	With the pusher plate from t=0 to 3 ms	Without the pusher plate
Assumption 1 by assuming compressible elastic	12.77 m	12.39 m
Assumption 1 by assuming incompressible elastic	12.61 m	12.23 m
Assumption 2	8.17 m	7.79 m

TABLE 2.2: Estimated penetration depth in antelope tuff using different models by neglecting friction.

Table 2.2 shows that adding the impact of the pusher plate led to a 3-5% increase in the expected penetration depth by using different methods. Longcope and Forrestal (1983) predicted a penetration depth of 7 m by using the pressure-dependent failure model and neglecting the friction while the measured depth was 7.9 m. Table 2.2 shows that Assumption 2 better estimates the final penetration if we can ignore the friction for this target material. However, this target material has no water content, and friction has notable effects on nose erosion (Forrestal et al., 1986). Forrestal et al. (1986) estimated that for the antelope tuff, the coefficient of sliding friction would be 0.08 for the velocities higher than 30 m/sec, and then it increases linearly to 0.5 at zero velocity. We used this along with various values to see the effect of friction on our solution.

Table 2.3 shows the effect of sliding friction on penetration depth and time. The pusher plate's effect is included until it separates from the projectile at 3 ms. As stated above, the actual penetration depth was 7.9 m while Longcope and Forrestal (1983) estimated the final penetration depth of 7 m by neglecting the friction effect. Therefore, adding friction to their solution will further reduce predicted penetration depth. On the other hand, Table 2.2 shows that using Assumption 1 allows us to add the friction effect since, without friction, it predicts higher penetration depths than the Longcope and Forrestal

(1983) solution. Assumption 2 predicts lower penetration since it results in a higher stress evaluation at the cavity wall. The reason is that this target material is a dry porous medium where it undergoes huge deformation and particle rearrangement followed by void collapses which result in stress reduction and absorbing projectile energy. Assumption 2, however, associates this large deformation for the entire plastic region to stress based on Equation 2.36 and its relatively high value of K. Therefore, this model appears to estimate a lower bound for the penetration depth, while Assumption 1 seems to yield a more accurate estimation when friction is included. From the measured deceleration in Longcope and Forrestal (1983), we can see that around t= 29.3 ms, there is a sudden drop in the deceleration. It decreased to zero approximately at 30.3 ms and then oscillated around zero until it disappeared. From Table 2.3, we can see Assumption 1 with $\mu = 0.1$ has a good agreement with the measured penetration time (around 30 ms) and depth (7.9 m) reported in Longcope and Forrestal (1983).

	μ =0.03		μ =0.05		μ^a		μ =0.1	
Assumption 1 by assuming compressible elastic	10.94 m	45.7 ms	9.99 m	41.5 ms	8.83 m	35.5 ms	8.22 m	33.9 ms
Assumption 1 by assuming incompressible elastic	10.81 m	45.5 ms	9.87 m	41.3 ms	8.74 m	35.4 ms	8.14 m	33.7 ms
Assumption 2	7.00 m	28.5 ms	6.39 m	25.9 ms	5.66 m	22.2 ms	5.27 m	21.1 ms

[a] From (Forrestal et al., 1986)

TABLE 2.3: Estimation of the penetration depth and time.

2.4.3 LUNAR-A penetration in JSC-1 simulant

In this section, the LUNAR-A penetrations in JSC-1 simulant is estimated and evaluated. LUNAR-A was a portable rig design containing two-component probes, a seismometer and a heat-flow, for the lunar subsurface investigation, with a total mass of 14 Kg, a diameter of 14 cm and a length of 75 cm (Shiraishi, Tanaka, Fujimura, and Hayakawa, 2008). It was meant to hit the Moon's surface with a velocity of 285 m/sec and predicted to penetrate 1 to 3 m depending on the lunar regolith's properties, according to the impact tests using full-size models and a lunar regolith simulant target. At shallow depths (<30 cm), penetration and excavation are not problematic on the lunar surface. However, the high relative density of the regolith just a few centimetres below the surface makes penetration challenging (Colwell, Batiste, Horányi, Robertson, and Sture, 2007). For the depth of 0-30 cm and 30-60 cm, Houston, Mitchell, and Carrier III (1974) recommends a relative density of 74±3% 92±3%, respectively, for lunar regolith. Accordingly, we used the lunar regolith simulant properties of JSC-1 reported in (Klosky, Sture, Ko, and Barnes, 2000) with a relative density of 95% and 75% for a rough estimation. The properties of the regolith presented in (Klosky,

Sture, Ko, and Barnes, 2000) are: ρ_0 =1720 Kg/m^3, E =60 MPa, K =37 MPa, $\phi_f = 49.5^\circ$ and C_{oh} =6.2 kPa for Dr =75% and ρ_0 =1810 Kg/m^3, E =70 MPa, K =43MPa, $\phi_f = 53.6^\circ$ and C_{oh} =14.4 kPa for Dr =95%. For E and K, the proprieties at lower confining pressure (10 kPa) are used regarding the low gravity on the Moon. Based on the high hardness of lunar soil and the simulant (Klosky, Sture, Ko, and Barnes, 2000), it is expected that particle fracture is marginal at this low-velocity impact. Moreover, considering the relatively low bulk modulus of the medium, Assumption 2 can lead to a reasonable approximation of the penetration. However, triaxial test on regolith and pressure-volume strain data are needed to confirm this assumption further.

Table 2.4 shows our approximate estimation of the LUNAR-A penetration in the compacted JSC-1 simulant with relative density of Dr =75% and 95%. Moreover, compared to terrestrial soils, lunar soils and JSC-1 simulant are exceptionally frictional. Therefore, the effect of friction has been added to the simulation. As we can see, increasing CRH can notably improve the penetration depth, reduce the maximum normal stresses on the projectile nose and the probe acceleration upon the impact. As CRH increases, ϕ_0 at the nose tip increases. It results in a reduction in the cavity expansion velocity ($V_p \cos(\phi)$). Consequently, the normal stress and the decelerating force on the projectile decrease. This is compatible with the nose performance coefficient used by Young (1997) in their empirical correlation formulation. In addition, increasing the coefficient of friction indicates that the probe's performance decreases as penetration depth decreases and maximum acceleration increases in more frictional regolith layers. Probes with a higher CRH have a larger surface in contact and friction with the surrounding regolith, so they are more likely to be affected by high frictional environments. However, the numerical simulation shows that the higher CRH probe still has better penetration depth and lower acceleration in the high frictional regolith. Lunar regolith's penetration data, high-pressure test data (triaxial test and pressure-volume strain), sliding friction coefficient between probe and regolith are needed to verify/modify our proposed model for real lunar investigation cases.

	Dr =75%						Dr =95%					
	μ =0.1		μ =0.3		μ =0.5		μ =0.1		μ =0.3		μ =0.5	
	CRH =3	CRH =6	CRH =3	CRH =6	CRH =3	CRH =6	CRH =3	CRH =6	CRH =3	CRH =6	CRH =3	CRH =6
Penetration depth	1.96 m	2.51 m	1.32 m	1.54 m	1.00 m	1.11 m	1.62 m	2.04 m	1.09 m	1.25 m	0.82 m	0.90 m
Maximum acceleration	4444 g	3385 g	6525 g	5459 g	8606 g	7533 g	5084 g	3915 g	7480 g	6333 g	9877 g	8750 g
Maximum normal stress	59 MPa	41 MPa	59 MPa	41 MPa	59 MPa	41 MPa	67 MPa	46 MPa	67 MPa	46 MPa	67 MPa	46 MPa

TABLE 2.4: Expected LUNAR-A penetration in JSC-1 compacted simulant

2.5 Conclusions

Non-linear cavity expansion approximations have been developed using the Mohr-Colomb failure criterion to simulate the rigid projectile penetration into geological targets under perpendicular subsonic impacts. The locked hydrostat and linear pressure-volumetric strain assumptions were used to evaluate the stresses on the projectile penetrating into geological targets. The locked hydrostat modification was introduced where the cavity pressure is not high enough to compact the material near the cavity wall completely. The velocity of impactors is assumed to be low enough that the resulting plastic wave does not exceed the elastic wave. A closed-form solution for radial stresses at the penetrator's nose was developed for the locked hydrostat model. Similarly, the numerical procedure to find stresses on the penetrator's nose was presented for the linear pressure-volumetric strain model. Our computation shows that fourth-order polynomial least-square fitted curves can perfectly represent the obtained normal stresses at the cavity wall, facilitating the numerical integration and result in closed-form solutions for the projectile's deceleration. Numerical results show that the linear volumetric strain model estimates higher stresses on the projectile and, therefore, evaluates a lower penetration, especially in porous target materials with high bulk modulus. However, for dense soils, the difference between the test and this method was less significant. It can be due to this fact that in this method the compression of the soil near the projectile is directly connected to stresses on it. However, the closure of voids near the projectile can absorb much of the energy and reduce the level of stresses. Therefore, this method provides a lower bound for the penetration depth of the projectile, and its estimation seems to be beneficial when dealing with dense soils and regolith and also where we do not have access to pressure-volumetric strain data. On the other hand, the locked hydrostat model and the modified version presented in this study estimated relatively lower stresses at the cavity wall and can predict the final penetration depth more accurately. Moreover, the numerical results indicate that, at higher velocities, the incompressible elastic assumption results in higher estimated stresses on the projectile and, as a result, a shallower penetration depth prediction.

Our developed models can be used to design and evaluate the stresses on subsonic portable probes for subsurface investigation. However, for this purpose, different penetration tests and experiments in the subsonic range in regolith and granular materials are required to thoroughly verify the robustness of the proposed solutions or modify and develop the proposed methods. To meet this objective, the mechanical properties of the soil used

in this method, such as density, Young's modulus, Poisson's ratio, variation of density under different pressures, friction angle, and cohesion, need to be determined before any tests. In addition, if the friction between the granular material and the probe is not negligible, as in lunar regolith, the magnitude of the sliding friction coefficient is required. Also, it is important to determine the subsonic range for the target material since it varies significantly for different soil types. Additionally, the probe material must be hard enough for very tough soils to avoid the bulging effects, which reduce the probe velocity and affect our assumption of solid projectile penetration. Alternatively, by coupling this solution with the Finite Element Method (FEM), it will be possible to consider the deformation of the probe in higher-velocity impact penetrating harder soils in the subsonic range or simulating oblique impact problems into granular materials. Furthermore, measuring the final penetration depth is insufficient to verify the method. The acceleration needs to be measured throughout the penetration to determine precisely how well the method can predict the deceleration of the probe and, therefore, the forces and stresses it encounters during penetration. Besides, measuring acceleration allows us to detect different phases in the probe penetration and determine which assumption is more appropriate for the prediction of the probe velocity in each phase. Finally, the stress profile around the projectile nose can be investigated and modified further for different geometries to reflect the real stress propagation more accurately.

Chapter 3

Penetration Analysis of High-Frequency Vibro-based Probes in Granular Media Using the Discrete Element Method

Abstract

Due to payload limitations in space missions, light and compact investigation tools should be developed for subsurface exploration on the Moon, Mars, and beyond. Here, we aim to investigate the effects of high-frequency vibrations on reducing the overhead load required for the penetration of a typical probe into granular media. The Discrete Element Method is used to examine the effect of vibration frequency, mode, and the probe's head on penetration resistance. The results show that employing high-frequency vibration is a promising technique for overcoming the payload limitations for subsurface investigation in remote areas.

3.1 Introduction

Percussion is instrumental in fracturing rigid, brittle materials such as concrete, stones, and ceramics. In contrast, rotation is more effective in soft and ductile materials such as wood and plastics (Badescu, Bar-Cohen, Sherrit, Bao, Chang, Donnelly, and Aldrich,

Alaei Varnosfaderani, M., Maghoul, P., Wu, N. (2023). "Penetration analysis of high-frequency vibro-based probes in granular materials using the Discrete Element Method." *ASCE, Earth and Space 2022*, 176-183. https://doi.org/10.1061/9780784484470.016.

2012). One of the proposed designs to overcome the drilling challenges in planetary missions was an ultrasonic/sonic driller/corer (USDC) mechanism for rock drilling (Sherrit, Bao, Chang, Dolgin, Bar-Cohen, Pal, Kroh, and Peterson, 2000). The USDC consists of three main parts: an ultrasonic horn transducer (actuator: piezoelectric stack, backing element, and a horn), a free mass, and a drill stem. The piezoelectric stack is confined and remains in compression between the backing and the variable cross-section horn. The horn amplifies the longitudinal vibrations from the piezoelectric stack and vibrates at its resonant frequency of around 21.5 kHz. It results in a free mass vibration between the horn tip and the top of the drill stem with average frequencies between 100 and 1000 Hz. Sonically stress pulses transfer ultrasonic energy from the transducer to the drill stem and create shock waves at the bit/rock interface. Rock fracture occurs when fatigue strength is finally passed by hammering. The lightweight (450 g) prototype proved to be efficient for drilling different rocks at shallow depth with low preload (less than 5 N) and low driven power (Bao, Bar-Cohen, Chang, Dolgin, Sherrit, Pal, Du, and Peterson, 2003). Subsequently, the device was mounted on several rover configurations (Sojourner Rover and FIDO Rover) (Bar-Cohen, Sherrit, Dolgin, Bridges, Bao, Chang, Yen, Saunders, Pal, Kroh, et al., 2001). However, removing cutting after a certain depth becomes problematic and reduces its efficiency (Wang, Quan, Yu, Bai, Li, and Deng, 2018). Cardoni, Harkness, and Lucas (2010) proposed two new ultrasonic drilling devices where the ultrasonic bits were designed to transform the longitudinal vibrations into longitudinal-torsional vibration. In their preliminary drilling tests, it was observed that composite mode devices could improve drilling/coring efficiency.

Firstbrook, Harkness, and Gao (2014) conducted a series of experiments to observe high-powered ultrasonic vibration effects on penetration in granular materials. An ultrasonic Langevin transducer provided ultrasonic vibration of 20 kHz up to 10 µm amplitude. The horn, penetrator, was manufactured from 94Ti/6Al/4V alloy and designed to resonate in the second longitudinal mode at 20 kHz with the resulting amplification ratio (gain) of 3.5. The rig was set to penetrate into different Martian regolith simulants with high and low density at slow (3 mm/s) and fast (9 mm/s) rates corresponding to 4.81 V and 12 V, respectively. While slow non-ultrasonic penetration needed a larger overhead force, they observed the opposite was true in ultrasonic penetrations. Moreover, adding ultrasonic vibrations led to a marked reduction of the required peak axial force. It seems that the ultrasonic vibration provides granular fluidization in the immediate surrounding of the drill, reducing the surface friction and assisting sand particles mobilization and the probe

penetration. The highest reduction of axial force occurred using the lowest amplitude of 1 µm, which corresponded to the lower total power consumption (actuator and ultrasonic units). After that, the peak penetration force reduction became more gradual and less conspicuous. Interestingly, the high-density regoliths exhibited a more significant reduction in the peak force than the low-density regoliths by implementing ultrasonic vibrations. Therefore, incorporating the ultrasonic vibro-based technique in self-burrowing probes seems helpful for penetration into the lunar regolith, which has a high relative density just a few centimetres below the surface.

In their subsequent study, (Firstbrook, Worrall, Timoney, Suñol, Gao, and Harkness, 2017) investigated the effect of gravity on the penetration of probes in granular media. They only considered the high-density regoliths with the faster penetration rate (9 mm/s-12 V) with a higher resolution of amplitude in the range of 0-2 µm. The tests were conducted in a centrifuge, a cost-effective method to examine gravity's effects by observing the penetration in higher gravities (1g-10g) and then extrapolating results downward. Regardless of gravity, the ultrasonic vibrations assisted penetration. Higher gravities led to implementing higher axial forces. Moreover, in lower gravities, the percentage of reduction in penetration forces was higher. For example, they observed that the force could be reduced by 70% in 1g and 1 µm amplitude of vibration, while the reduction would be just 50% in 10g for the same vibration's amplitude. Therefore, the trend suggests that these benefits could be advantageous in lower gravity to compensate for the lower weight and force on the drill bit. Similarly, Firstbrook et al. (2018b) observed noticeable enhancements in a percussive probe's drilling efficiency by synchronizing short ultrasonic vibration pulses with the hammer impact. The number of hammer strikes needed to achieve a specified depth (190 mm) at the highest excitation amplitude (1.6 µm) was reduced from 48 to 15 and from 33 to 17 for block paving sand (BP) (Dr =48.3%) and lunar regolith simulant SSC-3 (Dr =43.1%), respectively. In addition, it was noticed that at low penetration depths, implementing only ultrasonic vibration could fluidize the sand to such an extent that the penetrator had a brief moment of near-freefall. This advantage is beneficial for future probe applications on the moon. The probe can exploit the ultrasonic vibration to bury itself into the loose regolith on the moon's surface on its weight. Subsequently, the ultrasonic vibration performs its capacity to assist the primary mechanism in penetrating into the dense regolith just a few centimetres below the surface.

Firstbrook, Worrall, Harkness, Flessa, McGookin, and Thomson (2018) investigated the effects of ultrasonic vibration on auger drilling performance. Glass microspheres with a

particle size distribution of 150-250 µm were chosen to replicate the penetration in fine sand. The maximum overhead force was approximately reduced from 600 N to 100 N only by implementing rotary penetration (14.7 RPM) compared to the non-rotary one. On the other hand, ultrasonic vibration was able to reduce it roughly to 350 N in the non-rotary penetration by implementing an amplitude of 10 µm. Therefore, it seems that rotation has much more significant effects on the reduction of required overhead force than ultrasonic vibrations. Moreover, the required force was independent of any ultrasonic vibration in the rotary penetration, indicating the force had already been adjusted more than ultrasonics could provide. However, the required maximum torque decreased from 120 Nm to 85 Nm (30% reduction) by increasing the ultrasonic vibration amplitude from 0 to 10 µm.

However, all their experiments were conducted at 20 kHz, which corresponds to the second longitudinal vibration mode of an ultrasonic horn. What has not been investigated yet is whether it is possible to save more energy by using vibrations at lower frequencies and have similar effects. More precisely, the role of vibration frequency is needed to be studied. Furthermore, the impact of other vibration modes on penetration into granular materials is also unknown. For example, it is required to investigate whether the lateral vibration, or swinging, or stirring motion of the probe nose is more effective than the longitudinal vibration or not. Such lateral vibrations, at a lower frequency, are used by snakes to hide into granular materials. Knowing the most efficient vibration frequency and mode is critical to design any vibro-based penetrator for future space missions. Therefore, we aim to investigate the effect of vibration frequency, mode, and the probe's nose geometry on assisting penetrations into granular materials by using DEM simulation. The discrete element method (DEM) is particularly well-suited for this investigation because it models granular materials at the individual particle level. Unlike continuum-based methods such as FEM or FDM—which treat the material as a continuous medium, DEM models individual particles by capturing their size, geometry, and interactions with surrounding particles. Therefore, DEM accounts for critical phenomena such as compaction, dilation, and particle rearrangements during penetration events. By leveraging DEM, we aim to more realistically represent the discrete nature of granular materials and gain deeper insights into penetration mechanisms and the effects of vibration on reducing soil resistance.

3.2 Model Descriptions

As shown in Figure 3.1, a three-dimensional DEM model was developed in EDEM 2021 (Altair Engineering Inc.) to simulate the vibro drilling process. The height of the regolith in the sandbox is 675 mm. The drilling tool with a diameter of 40 mm penetrates into a sandbox with an inner cross-section area of $205 \times 205\,\text{mm}^2$ and 820 mm in height to minimize the effects of the boundaries. The size of the drilling tool is similar to the DROD system in (Alkalla, Pang, Pitcher, and Gao, 2021), with the only exception that we have a mono head drilling bit instead of two valves. The DEM parameters are selected from (Alkalla, Pang, Pitcher, and Gao, 2021) to model the lunar regolith qualitatively (Table 3.1). The Hertz–Mindlin contact model was selected. The particles are modeled with uniformly sized triple spheres to account for the irregularity of lunar regolith shapes. In addition, the Johnson-Kendall-Roberts (JKR) model and standard rolling friction model are added to account for the cohesion and high frictional properties of the lunar regolith. All DEM simulations in this study were performed on a workstation equipped with an Intel® Core™ i7-6700 CPU operating at 3.40 GHz and 32.0 GB of installed RAM.

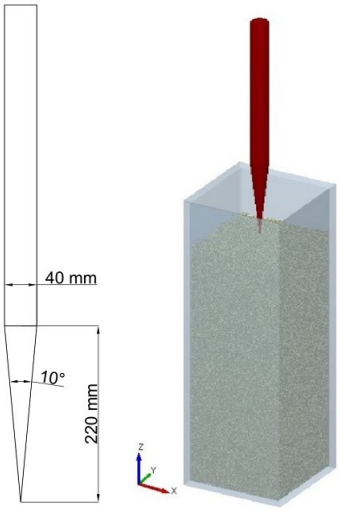

FIGURE 3.1: Probe's dimensions and model in EDEM.

3.3 Results and Discussion

In the first simulation, the probes were pushed into the granular materials at a constant speed of 2 m/s. For the purpose of evaluating the effects of lateral vibration on penetration resistance, a lateral vibration of 500 Hz with different amplitudes has been added to the vertical motion. Figure 3.2 shows that a lateral vibration with an amplitude of 0.05 mm

TABLE 3.1: DEM model parameters.

Parameters	Value
Number of triple sphere particles	1344958
Sphere particle radius[a]	1 mm
Particle solid density[a]	2875 kg/m^3
Particle shear modulus[a]	50 MPa
Particle Poisson's ratio	0.25
Particle-Particle friction[a]	0.5
Particle-Wall friction[a]	0.2
Coefficient of rolling friction	0.1

[a] From (Alkalla, Pang, Pitcher, and Gao, 2021)

has no noticeable effect on penetration resistance. In contrast, the required vertical force has been reduced significantly as the amplitude increased to 0.5 mm and 1 mm. As the amplitude increases to A=0.5 mm and A=1 mm, the penetration force drops approximately by 25 percent and 50 percent, respectively.

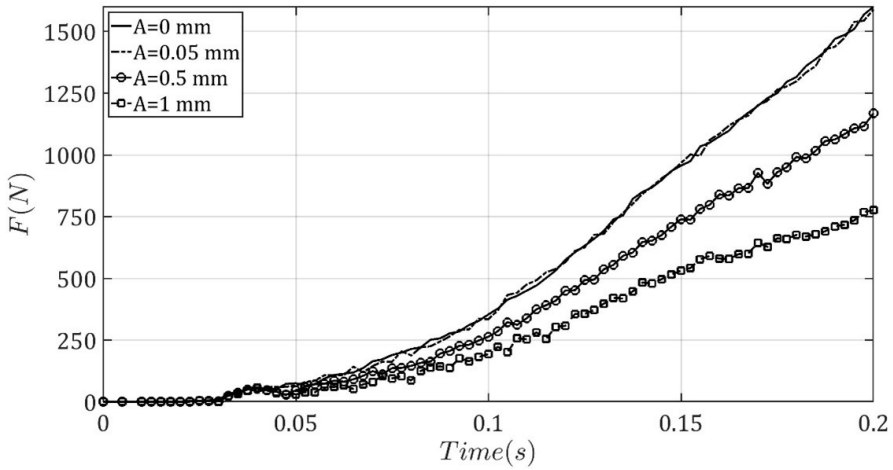

FIGURE 3.2: Total vertical force in different vibration amplitude at frequency 500 Hz.

In the next simulation, the penetration speed is dropped from 2 m/s to 200 mm/s at t=0.11 s, after full embedment of the probe head into the regolith. This reduction in speed is deliberate to better understand the effect of penetration speed on soil resistance force and to isolate the effect of vibration frequency on resistance while minimizing the influence of rapid penetration. At this point (t=0.11 sec), the lateral vibration with an amplitude of 0.05 mm is added to the vertical motion. The simulation was conducted at various vibration frequencies to investigate vibration's impact on penetration resistance. As we can see from Figure 3.3, the reduction in penetration speed leads to a sudden drop in the penetration resistance force. In comparison to the previous simulation, Figure 3.3 shows a more notable

reduction in penetration resistance at a frequency of 500 Hz and an amplitude of 0.05 mm. Compared to the previous simulation, the penetration speed here is only 200 mm/s, which is ten times slower than before. Therefore, at a lower penetration rate, vibrations of the probe appear to be more effective in reducing the penetration resistance. In other words, the probe can transfer its vibration energy more effectively to the surrounding regolith at a slower penetration rate. Furthermore, increasing the vibration frequency from 500 Hz to 5500 Hz significantly reduces the maximum penetration resistance by approximately 36%. However, increasing the frequency again from 50500 Hz to 10500 Hz has a less noticeable effect on further decreasing the penetration resistance.

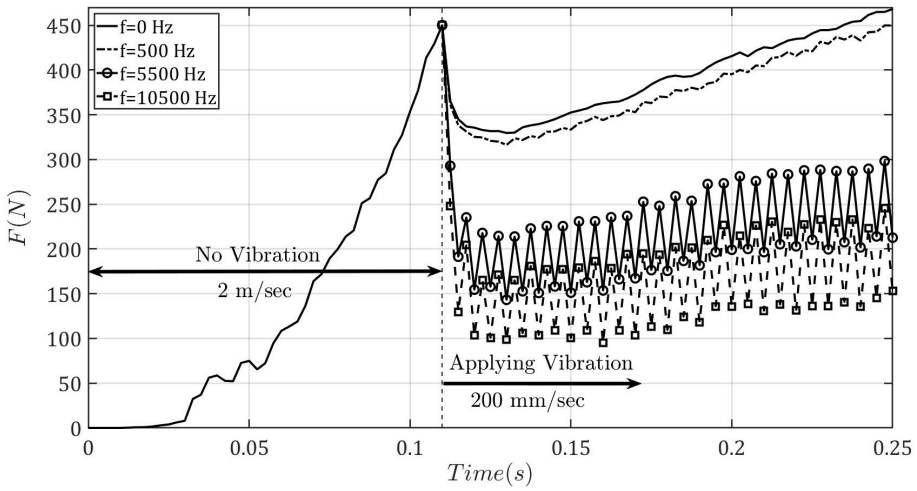

FIGURE 3.3: Total vertical force in different frequencies with amplitude of 0.05 mm.

We then applied longitudinal vibrations with the frequency of 10500 Hz and amplitude of 0.05 mm to compare with the previous horizontal vibrations. Figure 3.4 shows that the effect of longitudinal vibration on the reduction of the resistance force is inconspicuous compared to lateral vibration. The reason is that longitudinal vibration is in the direction of penetration, which results in compression of the lower layers of the regolith. Alternatively, lateral vibration forces the regolith particles away from the probe penetration path. Therefore, it is more effective at fluidizing the surrounding soil and assisting the probe's penetration. Based on the experimental results (Firstbrook, Harkness, and Gao, 2014), longitudinal vibrations seem to require higher frequencies to fluidize the soil particles effectively.

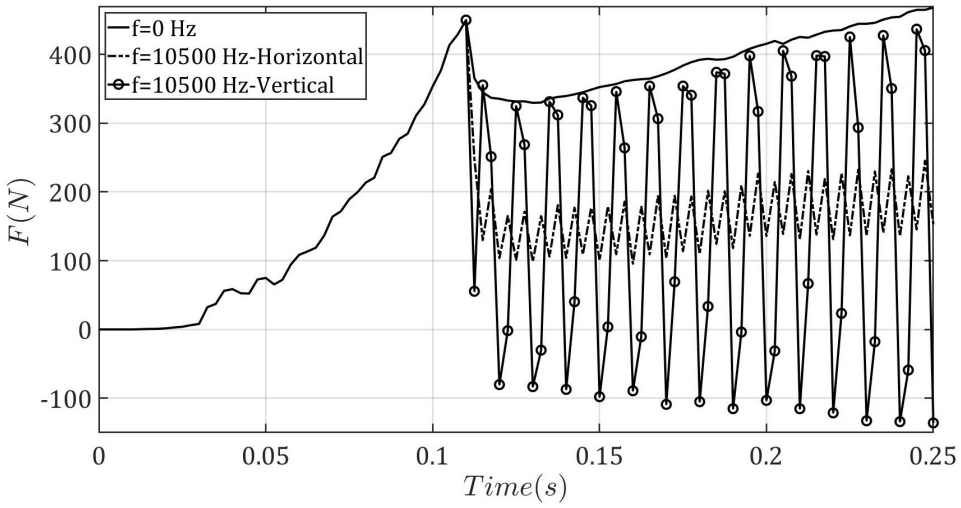

FIGURE 3.4: Total vertical force in longitudinal and lateral vibration with amplitude of 0.05 mm.

In the following simulation, the probe is assumed to weigh 10 kg. It is released into the granular material at t=0.01 s, and it penetrates it under its own weight. Figure 3.5 shows that probes have a free-fall motion at first until the granular material resistance force starts to decelerate the probe. If there is no lateral vibration (A=0), around t=0.27 sec, the probe begins to bounce, indicating that it has reached the maximum depth it can penetrate under its own weight. However, implementing lateral vibration at the frequency of 10500 Hz and amplitude of 0.05 mm can eliminate the rebound. Moreover, at t= 0.35 sec, the probe penetration rate remains almost constant, and at t=0.039 sec, the probe starts to experience a slight downward acceleration.

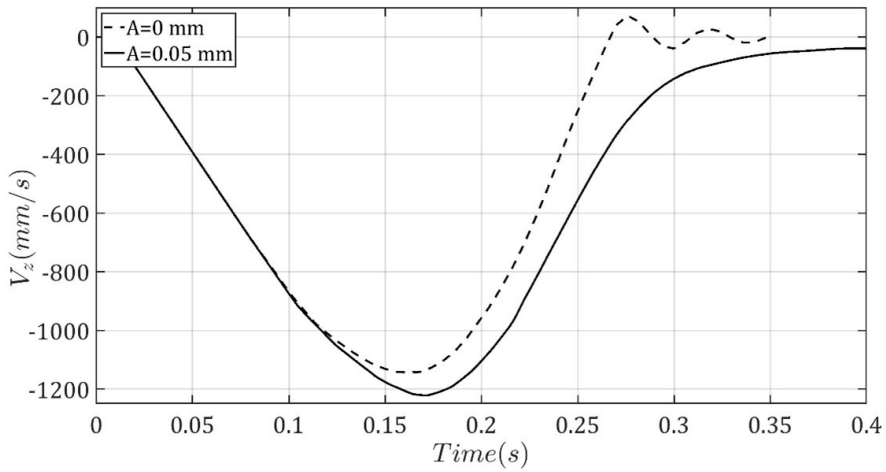

FIGURE 3.5: Vibration impact at the frequency of 10500 Hz on the penetration rate for the conical nose ($\alpha = 10.4°$).

Next, we repeated the above simulation with another probe with the Caliber Radius

Head (CRH) of 3 and the same diameter to observe the effect of the nose on the performance. Figure 6 shows that the vibrated probe still leaves no rebound behind. However, the impact of vibration on the ogival nose is less pronounced than the conical nose as illustrated in Figure 5. Based on the empirical equations developed by Young (1997) for high-velocity impacts (less than 1200 m/s), the above conical nose has the nose performance coefficient of 1.93, and the ogival nose has the nose performance coefficient of 0.85. Similarly, for the current simulation, quasi-static penetration with lateral vibration, the nose performance effect is prominent. The vibrated ogival nose probe reaches an almost constant penetration rate of 6 mm/s at t=0.30 s, while the vibrated conical nose has an almost constant velocity of 40 mm/s around t=0.40 s. Moreover, this is compatible with the result from (Alaei Varnosfaderani et al., 2022), which shows a high-speed probe with a longer nose length can outperform the one with a shorter nose in terms of penetration.

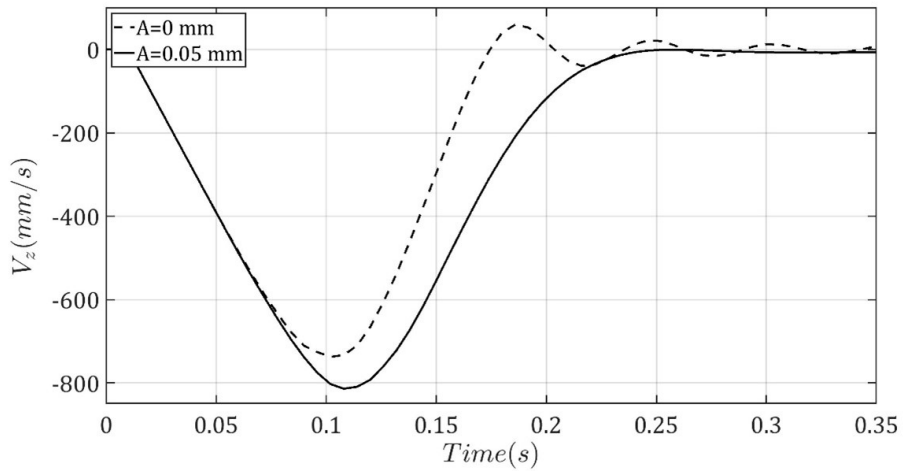

FIGURE 3.6: Vibration impact at the frequency of 10500 Hz on the penetration rate for ogival nose ($CRH = 3$).

3.4 Conclusions

DEM simulations have been used to analyze the effects of probe lateral vibrations on reducing regolith resistance forces. Our simulations show that the required penetration force will reduce by increasing the vibration frequency or amplitude. However, the rate of the reduction in the required axial force decreases with increasing the vibration frequency, while this rate seems to be consistent in different amplitudes. On the other hand, vibration appears to be more effective at lower penetration rates, where the kinetic energy of the probe's vertical motion is much lower than the kinetic energy of vibration. Furthermore, the nose geometry of the probe (nose performance) played a significant role in the penetration

rate achievable at a constant overhead weight. In all the above simulations, the probe has been considered as a rigid body, and a few centimeters of penetration were simulated. For future investigations, it is required to model the probe as a flexible structure to investigate its flexural resonance vibration modes on reducing the required axial forces.

Chapter 4

The Effect of Bending Vibration Modes on Penetration of Bio-Inspired Drilling Tool in Granular Materials: An Experimental Study

Abstract

Conventional drilling tools used on Earth are impractical for lunar subsurface exploration due to payload limitations. To overcome this, high-frequency vibration can be employed to reduce the soil penetration resistance and develop a more compact drilling tool for remote subsurface investigations. Therefore, this study aims to investigate the effects of bending vibrations to facilitate probe penetration into granular materials. We attached piezo patches to the probe and conducted experimental modal analyses to determine resonance frequencies. The probe was then inserted into different granular materials, with and without lateral vibrations and corresponding vertical penetration forces were measured. Our test results demonstrate that bending vibration modes significantly reduce the vertical force required for probe insertion into granular soil samples.

Alaei Varnosfaderani, M., Maghoul, P., Wu, N. (2024). "The Effect of Bending Vibration Modes on Penetration of Bio-Inspired Drilling Tool in Granular Materials: An Experimental Study." *ASCE, Earth and Space 2024*. https://doi.org/10.1061/9780784485736.033.

4.1 Introduction

Subsurface investigation on planetary bodies, such as the Moon and Mars, can provide valuable information regarding the geologic formation, the possibility of extraterrestrial life, shifts in historical climate, and the presence of mineral resources such as volatiles. Moreover, it assists in effectively planning for construction, mining, and establishing a human presence beyond Earth on these celestial bodies. However, accessing the subsurface layers of dusty planets poses challenges. Traditional drilling techniques from Earth are not suitable due to size and weight restrictions during space missions. As a result, it becomes essential to develop lightweight tools specifically designed for exploring these remote sub-layers. These tools need to work well under reduced gravity, provide accurate data for scientific research, and explore despite limited resources. One of the solutions proposed to address the challenges of drilling in planetary missions was the development of an ultrasonic/sonic driller/corer (USDC) mechanism for rock drilling (Sherrit, Bao, Chang, Dolgin, Bar-Cohen, Pal, Kroh, and Peterson, 2000). This innovative system consists of three key components: an ultrasonic horn transducer comprising a piezoelectric stack, backing element, and horn; a free mass; and a drill stem. The piezoelectric stack is placed in compression between the backing and the horn, and the horn is designed with a variable cross-section to amplify the longitudinal vibrations deriving from the piezoelectric stack. This causes the horn to vibrate at its resonant frequency, typically around 21.5 kHz. As a result, the free mass between the horn tip and the top of the drill stem starts to vibrate at average frequencies ranging from 100 to 1000 Hz. The ultrasonic energy produced by the transducer is then transferred to the drill stem, causing frequent shock waves to propagate within the rock and result in its fracturing. The USDC prototype, weighing merely 450 grams, exhibited efficiency in drilling various rocks at shallow depths while operating with low preload (less than 5 N) and driven power (Bao, Bar-Cohen, Chang, Dolgin, Sherrit, Pal, Du, and Peterson, 2003). The device was further developed to be integrated into various rover platforms, including the Sojourner Rover and FIDO Rover, showcasing significant progress in its application (Bar-Cohen, Sherrit, Dolgin, Bridges, Bao, Chang, Yen, Saunders, Pal, Kroh, et al., 2001). However, a challenge with the proposed USDC system is the removal of cuttings as drilling progresses to greater depths. This issue hindered its efficiency in drilling greater depth. For example, Cardoni, Harkness, and Lucas (2010) introduced two new ultrasonic drilling tools to address this issue. These tools were designed to transform the back-and-forth vibrations into a twisting type of vibration. Initial

drilling tests showed that these newly designed tools had the potential to make drilling and coring more efficient. Firstbrook, Harkness, and Gao (2014) investigated the application of high-powered ultrasonic vibrations to enhance penetration in granular materials. They utilized a 20 kHz ultrasonic Langevin transducer, characterized by a 10 µm amplitude, for their experimental investigations. The penetrator, made of 94Ti/6Al/4V alloy, resonated in the second longitudinal mode at 20 kHz and had a gain of 3.5. They conducted penetration experiments in various Martian regolith simulants with differing densities at slow (3 mm/s) and fast (9 mm/s) penetration rates, both with and without ultrasonic vibration. The test results demonstrated the interplay between vibration and penetration dynamics. In instances of slow, non-ultrasonic penetration, a higher penetration force input was required. In contrast, ultrasonically assisted penetrations required reduced force inputs due to a transformative effect induced by the vibrational energy. The vibrations exhibited a remarkable fluidizing effect on the granular soils surrounding the drilling apparatus. This effect mitigated frictional resistance and facilitated the mobilization of sand particles and the efficiency of penetration. Interestingly, it was observed that the degree of force reduction varied with the density of the regolith simulants. High-density regoliths exhibited a more pronounced reduction in force when subjected to ultrasonic vibrations, a phenomenon not as prominently observed in low-density counterparts. This finding underscores the efficacy of ultrasonic vibro-based techniques, particularly in scenarios where high-density materials are encountered, such as the lunar regolith situated a few centimeters below the Moon's surface. In subsequent investigations, (Firstbrook, Worrall, Timoney, Suñol, Gao, and Harkness, 2017) examined the role of gravity on the probe penetration into granular media. They observed that vibration's effects were more pronounced in reduced gravities, leading to significant reductions in penetration forces. Later, (Firstbrook et al., 2018)demonstrated the efficacy of synchronizing ultrasonic vibrations with hammer impacts, which resulted in significant reductions in required hammer strikes for specific depths. Furthermore, in another study, (Firstbrook, Worrall, Harkness, Flessa, McGookin, and Thomson, 2018) examined ultrasonic vibration's impact on auger drilling. While acknowledging rotation's predominant influence in reducing overhead force, they highlighted that ultrasonic vibration still contributed to a substantial 30% reduction in maximum torque. The above studies shed light on the potential of ultrasonic vibrations to enhance penetration mechanisms in granular media. However, their experimental scopes were confined to a 20 kHz vibration frequency, which corresponds to the longitudinal mode of an ultrasonic horn. To expand this understanding, (Alaei Varnosfaderani, Maghoul,

and Wu, 2022) investigated the influence of various vibration modes on the penetration mechanisms in granular media. Utilizing Discrete Element Method (DEM) simulations, they explored the effect of lateral vibrations on regolith resistance during probe insertion. Their simulations showed that increasing vibration frequency or amplitude led to a greater reduction in required penetration force and a smoother penetration. Lateral vibrations exhibited superior efficacy during slower probe insertion due to enhanced energy transformation between the vibrated probe and soil. Additionally, the investigation showed the substantial impact of probe nose geometry on penetration rates under constant weight conditions. However, the numerical solution involves specific simplifications, including the assumption that the probe structure is rigid. Furthermore, despite the previous studies on employing high-power longitudinal vibration, it is important to note that this method only allows penetration along the horn's tip to the section where there is an increase in cross-section connected to the ultrasonic transducer. This hinders a bio-inspired self-burrowing design. To address this issue, we propose lateral vibration, inspired by natural self-burrowing mechanisms such as snakes' penetration mechanism into granular material. Our study aims to experimentally prove the feasibility of employing lateral vibration in fluidizing soils and reducing the penetration force. We compare the effects of different lateral vibration mode shapes to enhance penetration. These vibrations can be induced via thin piezo patches on the probe's surface to enable full burial without increasing the probe's perimeter.

4.2 Experimental Set-up

In this study, we created a hex probe-actuator probe to investigate how lateral vibration affects soil resistance during probe penetration (Figure 4.1). More detailed drawings have been provided in the Appendix A. For piezo patch integration, we machined the probe's outer surface near its end to affix piezo patches, ensuring no perimeter increase. This design allows simultaneous insertion of both the probe body and patches into the soil—unlike longitudinal vibration, where the horn's larger cross-section remains outside the soil. However, we restricted penetration to a 24 cm depth to avoid contact wear. Practical applications can utilize advanced manufacturing to secure patches within the tube, protecting them from abrasion. The piezo patches used (50.00 mm × 7.00 mm × 0.50 mm, PZT material (APC International)) are illustrated in Figure 1. The patches have the same polarization direction. Therefore, when we apply the same AC voltage to the outer

surface electrode of the patches, it induces bending vibrations in the probe.

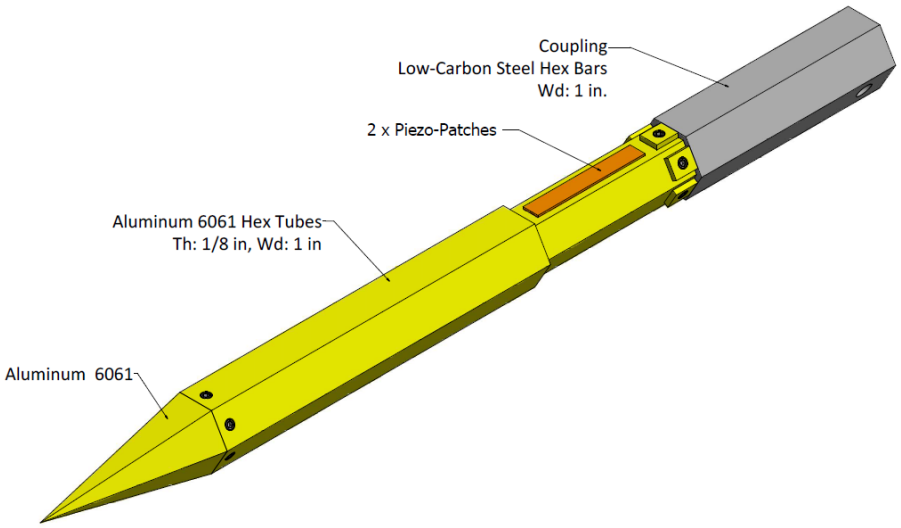

(A) Probe coupling Assembly

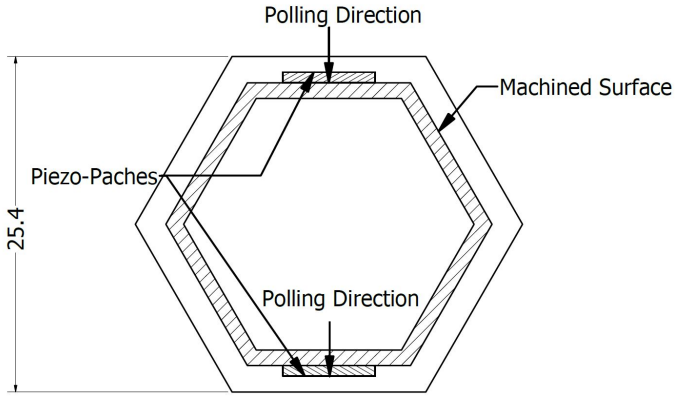

(B) Probe actuators configurations

FIGURE 4.1: Probe configuration

A linear actuator, driven by a 12 V DC input at a max speed of 10 mm/sec, pushes the probe into the soil. By adjusting the input voltage, we can control penetration speed. A force sensor measures the required penetration force, as shown in Figure 4.2.

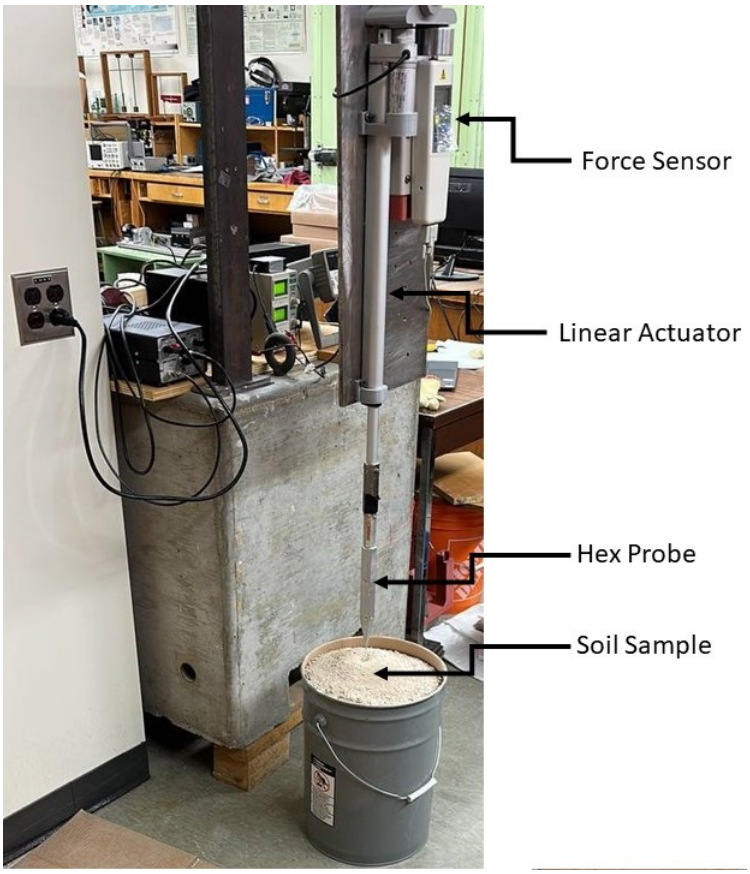

FIGURE 4.2: Set-up configuration

The soil sample comprises fine-cutting sub-angular limestone, with dry density from 1610 to 1950 kg/m^3. We chose sub-angular granular materials to better simulate the angular nature of lunar regolith, as opposed to the rounded soil particles commonly found on Earth. However, for future research, it is imperative to use more precise lunar regolith simulants. This precaution aims to prevent unforeseen issues, such as the challenges faced by the Mole during the Insight mission. In that instance, unexpected soil properties diminished friction between the HP3 and the soil, which led to mission failure (Dunn, 2021). Following the guideline of (Firstbrook, Harkness, and Gao, 2014), the material is poured from a fixed height of 1 m to ensure uniformity in mixing, distribution, and dependable outcomes. This procedure yields medium-dense sand at approximately 1790 kg/m^3 density and 58% relative density. The pail used measures 28.8 cm in diameter and 40 cm in height. The diameter of the pail is more than 11 times greater than the diameter of the probe to reduce boundary effects in penetration tests (Bolton, Gui, Garnier, Corte, Bagge, Laue, and Renzi, 1999).

4.3 Results and Discussions

Before conducting penetration tests, we perform a modal test to identify the probe's resonance bending frequencies. In the modal test, we applied a chirp signal with a voltage amplitude of Vmax =10V ranging in frequency from 0 to 20 kHz to the set of piezo patches to create bending vibration. Simultaneously, we positioned a Laser vibrometer sensor to focus its laser beam precisely on the probe's tip. Figure 4.3 illustrates the Laser vibrometer sensor's alignment, directing its beam onto the probe's tip.

FIGURE 4.3: Directing a laser beam toward the probe tip

After recording the velocity, we converted the data into displacement and acceleration measurements. Figure 4.4 depicts the FFT of the probe tip's displacement and acceleration. It is shown that probe tip acceleration is less prominent below 3.5 kHz compared to the 3.5-20 kHz range. Additionally, above 11 kHz, probe tip displacement remains relatively minimal in comparison to the 0-11 kHz range. Consequently, we suggest effective resonance modes for sand fluidization likely occur in the 3.5-11 kHz frequency range, characterized by noticeably higher displacement and acceleration levels.

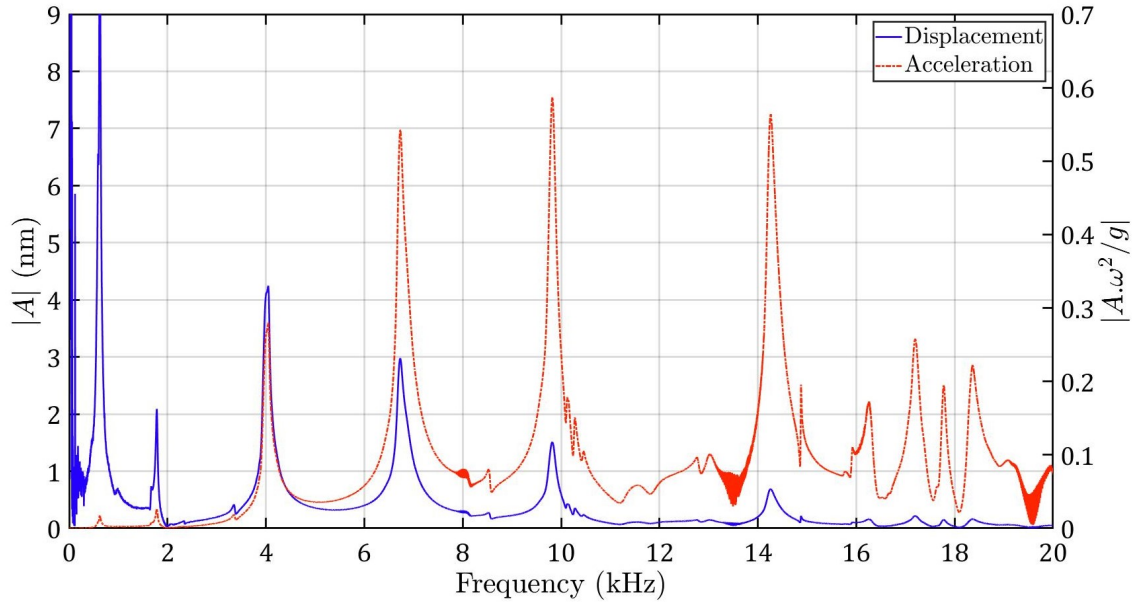

FIGURE 4.4: Single-sided probe tip amplitude spectrum

After the initial modal test, we performed a preliminary test by pushing a probe into the soil while altering the vibration frequency to identify the resonance frequencies that could reduce penetration force instantly. Throughout all vibration-based penetration tests, we kept the voltage constant at Vmax = 200V. Results showed that frequencies below 3.5 kHz had an inconspicuous effect on reducing soil resistance, and frequencies above 11 kHz led to a very slow reduction in penetration force. However, within the range of 3.5 kHz to 11 kHz, resonance modes promptly reduced penetration force. As highlighted by Alaei Varnosfaderani et al. (2022), achieving a substantial vibration amplitude is crucial for enhancing energy transfer to soil particles. Additionally, acceleration amplitude plays a critical role in fluidizing soil particles near the probe's tip. We then selected one resonance mode within the 0-3.5 kHz range and another within the 11 kHz-20 kHz range, where we didn't observe efficient vibration resonance frequencies for an immediate reduction in penetration force. We selected the frequencies 623 Hz and 14263 Hz based on our modal analysis data in Figure 4.4. At 623 Hz, we observed significant vibration displacement and acceleration below 3.5 kHz, while at 14263 Hz, we found the highest acceleration amplitude above 11 kHz in our modal test (as shown in Figure 4.4). Next, we performed three penetration tests: one without vibration, one with vibration at a frequency of 623 Hz, and another with vibration at a frequency of 14263 Hz. Figure 4.5 shows the penetration force over time for these tests, comparing the non-vibrating probe (f=0 Hz) with the probe vibrating at f=623 Hz and f=14263 Hz. As we can see from this figure, penetration takes almost 60 sec to be completed. However, even after this period, the structure is still under

stress, as the force in Figure 4.5 is not dropping to zero immediately. Most importantly, this figure indicates that both acceleration and displacement amplitudes are essential for soil fluidization, as lacking one causes unsatisfactory soil fluidization. At f=623 Hz, low acceleration amplitude results in no significant reduction in penetration force despite the highest amplitude of displacement in the range of 623-20000 Hz (Figure 4.4). On the other hand, at f=14263 Hz, low vibration displacement amplitude leads to insignificant improvement in penetration force despite high acceleration compared to the entire frequency range (Figure 4.4).

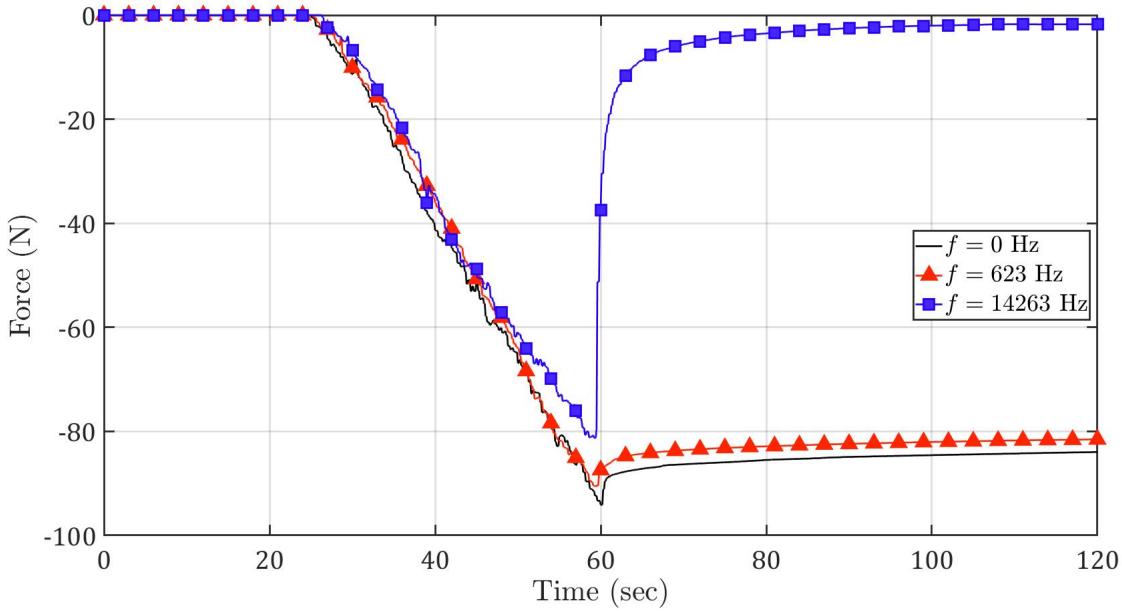

FIGURE 4.5: Penetration force with inefficient vibration modes

In Figure 4.6, we compare the efficacy of activating efficient bending modes to mitigate penetration force when compared to non-vibrational penetration. Notably, at the frequency of f=6731 Hz, the bending mode exhibits a more pronounced effect, reducing the maximum penetration force from 94.1 N in the non-vibrating probe (f=0 Hz) to 68.6 N. At f=9823 Hz and f=3937 Hz, the reduction is less substantial, with values of the maximum penetration force of 81.2 N and 86.5 N, respectively. Additionally, when the linear actuator stops (around t=60 sec), at the end of penetration, the probe structure remains under compressive stress in the non-vibrating probe case, as Figure 4.6 shows only a gradual decline in peak force, reaching 84 N at 120 sec from the peak of 94.1 N at 60 seconds. In contrast, at f=3937 Hz, f=6731 Hz, and f=9823 Hz, the force dropped to zero in $t_r = 2.0$ seconds, 1.2 seconds, and 1.6 seconds, respectively. This further proves that all three modes are capable of soil fluidization and implies that all three modes allow for a gradual penetration rate under

the probe weight without the need for the linear actuator. However, the resonance mode at f=6731 Hz appears to be the most effective, as it achieves the most substantial reduction in penetration force (R=26%) during the penetration process. On the other hand, the f=3937 Hz mode lags behind in terms of both reduction in penetration force and the time taken to achieve it when compared to the other two modes. These results are summarized in Table 4.1.

f_{avg} (Hz)	F^{a}_{max} (N)	R^{b}(%)	$t_r{}^{c}$(sec)
0	94	–	–
3937	86	9%	2.0
6731	69	26%	1.2
9823	81	14%	1.6

[a] Maximum Penetration Force in Newton
[b] Percentage of Maximum Force Reduction
[c] Release Time in seconds

TABLE 4.1: Penetration forces in one-directional excitation (hex probe)

As depicted in Figure 4.4, the three tested modes in Figure 4.6 exhibit higher levels of vibration displacement and acceleration amplitudes compared to the other resonance modes within the frequency range. This proves beneficial for reducing penetration force as it efficiently transmits more vibration energy to soil particles to fluidize the surrounding soils. In contrast, the resonance frequencies tested in Figure 4.5 show either lower displacement or acceleration amplitudes compared to the other resonance modes. This results in inefficient energy transfer to soil particles and minimal enhancement in reducing penetration force compared to the conditions depicted in Figure 4.6.

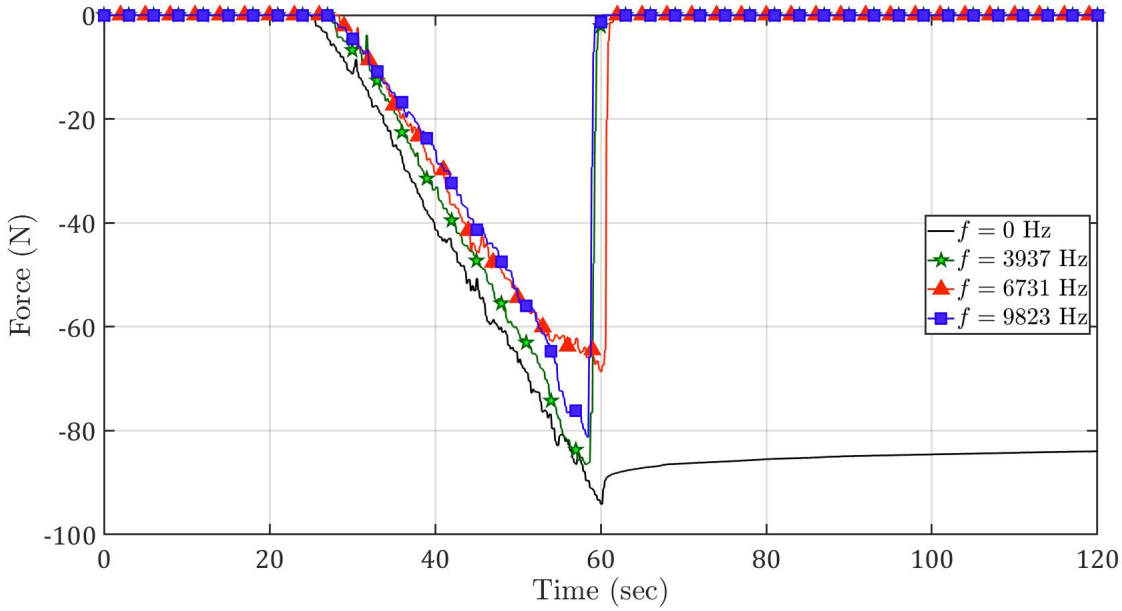

FIGURE 4.6: Penetration tests with efficient modes

4.4 Conclusions

Our modal testing revealed that effective resonance modes for sand fluidization likely occur in the 3.5-11 kHz frequency range, marked by significantly higher displacement and acceleration levels. Below 3.5 kHz, resonance bending modes have limited impact on soil resistance, while above 11 kHz, reduction in the penetration force occurs very slowly. Our preliminary penetration tests confirmed the importance of both vibration displacement and acceleration amplitude for enhanced energy transfer to soil particles. The 6731 Hz mode exhibited the most significant effect, reducing the maximum penetration force from 94.1 N to 68.6 N, surpassing the 3937 Hz and 9823 Hz modes. Additionally, after the probe ceased penetration, all three modes (3937 Hz, 6731 Hz, and 9823 Hz) enabled a sudden drop in penetration force under the probe weight, eliminating the need for a linear actuator. In conclusion, our test results indicate that utilizing lateral vibration has the potential to decrease soil penetration force significantly. However, in future studies, it is crucial to investigate how soil penetration resistance is influenced by bending vibrations in two distinct directions. The current hex probe design does not enable us to apply identical powerful bending vibrations in two perpendicular directions. To address this limitation, in the Chapter 5, we will concentrate on developing a probe geometry capable of effectively accommodating bending vibrations in two directions.

Chapter 5

Experimental Investigations of the Effects of Bending Vibrations Resonance Modes on Penetration into Granular Materials

Abstract

Inspired by the bending vibration observed in the biological locomotions such as those found in snakes, horned lizards, and sandfish, we have developed a novel vibro probe utilizing bending resonance modes to study the bending vibration effects in assisting penetration into granular materials. This approach contrasts with traditional probes that rely on longitudinal vibrations for penetration. This newly developed probe was used to experimentally investigate the impact of bending vibration in reducing the required penetration force and enhancing the penetration process within granular materials such as lunar or Martian regolith. The bending vibrations were excited by thin piezo patches attached to the probe's machined surface without increasing the probe's outside diameter. This simple mechanism enables pushing the whole probe inside the granular materials. Experimental modal analysis was employed to determine the resonance frequencies of the probe. Subsequently, the probe was pushed into granular materials, both with and without the bending vibrations, by a linear actuator. Experimental results indicated that employing

Alaei Varnosfaderani, M., Wu, N. and Maghoul, P. (2024). "Experimental investigations of the effects of bending vibrations resonance modes on penetration into granular materials." *Smart Materials and Structures*, 33(6), 065019. https://doi.org/10.1088/1361-665X/ad4758.

bending vibration in one direction led to a reduction in penetration force by up to 27% while utilizing two directions resulted in a reduction of up to 42%. Additionally, when the probe stopped penetrating the soil due to insufficient axial force, bi-directional bending vibration proved more effective in swiftly fluidizing the surrounding soil. These findings highlight the efficacy of bending vibrations in compact subsurface drilling tools.

5.1 Introduction

Access to dusty sub-layers of celestial bodies, such as the Moon, Mars, and asteroids, is crucial for scientists and engineers to discover evidence of life and investigate the extra-terrestrial past climate, evolution, and resources. Furthermore, the Moon and Mars sublayers' thermal, physical, and mechanical properties have always been vital for scientists to plan early construction and mining activities. Therefore, probes that can penetrate deeper into the sublayers have significant scientific and exploratory value. However, the current conventional subsurface investigation instruments used on Earth, such as rotary or percussive drilling techniques (cone penetration test, pressuremeter test, etc.), do not meet the space exploration mass and volume restriction requirements. The rigs used in these investigation instruments penetrate the desired depth by using the high axial force exerted by heavy machinery to overcome the soil layers' resistance. Accordingly, the development of innovative light, compact, and energy-efficient subsurface investigation tools for space missions is of paramount importance.

Numerous investigations have been done to replicate functional principles from organisms such as earthworm, caecilian, and razor clam locomotion, to provide sufficient penetration for a probe. For instance, Omori, Murakami, Nagai, Nakamura, and Kubota (2012) developed a prototype subsurface robotic system consisting of excavation and propulsion units. The excavation unit is based on an earth auger (EA), digging and making a space for the probe to proceed. The propulsion unit was based on the peristaltic crawling of earthworms, which prevents the probe's deviation, keeps it in the vertical position, and adjusts the friction against penetration. After the EA unit creates a hollow volume in front of the probe, the peristaltic crawling mechanism drives it forward. The performance of the prototype under its weight was satisfactory, up to 430 mm in depth. However, more development is needed to remove the dust properly. On another front, inspired by the dual-reciprocating drilling method (DRD) in wood wasp ovipositors, Gao, Ellery, Jaddou, Vincent, and Eckersley (2007) designed a bio-inspired micro-penetrator concept, less than

10 kg, consisting of an aftbody and forebody. After ground impact, which was expected to occur at approximately 150 m/s, the forebody penetrates below the surface while the aftbody remains on the surface for communication purposes. By employing Young's empirical equation, they roughly estimated that the initial penetration would be around 0.6 and 1.3 m, depending on the regolith characteristics. Then, the DRD self-contained drilling system continues for another meter. Later, there were different investigations on the DRD method to develop it further for soil drilling in space exploration. For example, Pitcher, Alkalla, Pang, and Gao (2020) introduced a compact, self-contained Dual Reciprocation Oscillation Drill (DROD) to overcome payload constraints. This innovative tool combines a cylindrical cam and dual followers for reciprocating motion, inspired by wood wasp ovipositors, with a double-faced wedge for oscillation, drawing inspiration from fish caudal fins. Its design allows for nuanced control over both reciprocating and oscillating movements, influenced by the cam slope and wedge angle.

Another solution proposed for overcoming drilling challenges in planetary missions involves the use of sonic/ultrasonic vibrations to decrease soil resistance and enhance penetration capabilities. In terms of rock drilling in planetary missions, Sherrit, Bao, Chang, Dolgin, Bar-Cohen, Pal, Kroh, and Peterson (2000) introduced a light mechanism called ultrasonic/sonic driller/corer (USDC) to address transportation limitations and drilling in harsh environments. The USDC has three main elements: an ultrasonic transducer, free mass, and a drill stem. The ultrasonic units consist of a piezoelectric stack that creates the ultrasonic waves at the frequency of 20 kHz while always remaining under pressure and compressed between a backing element and a horn. The ultrasonic horn has a variable cross-section and is designed to magnify the longitudinal vibration of the piezoelectric stack and transfer it to the free mass. As a result, the free mass starts to vibrate with average frequencies between 100 and 1000 Hz between the tip of the ultrasonic horn and the drill stem. Subsequently, the drill stem transmits the sonic shock waves at the bit/rock interface to the rock, and fracture occurs when fatigue strength is finally passed by hammering. The efficiency of the prototype led to mounting it on several rover configurations (Sojourner Rover and FIDO Rover) and conducting more tests. Although the prototype weighed only 450 grams, it was capable of shallow-depth drilling into different rocks such as granite, diorite, basalt, and limestone with a maximum preload of 5 N and power of 5 W (Bar-Cohen, Sherrit, Dolgin, Bridges, Bao, Chang, Yen, Saunders, Pal, Kroh, et al., 2001). A number of studies were later conducted to enhance the method and increase the drilling efficiency. For instance, Cardoni, Harkness, and Lucas (2010) designed two new ultrasonic drilling

systems for rock sampling, which designed a horn to transfer the longitudinal vibrations into the composite longitudinal-torsional vibrations. They found that the composite mode devices enhanced drilling/coring performance. Wang, Quan, Yu, Bai, Li, and Deng (2018) developed a Rotary-Percussive Ultrasonic Drill (RPUD) intended for rock sampling in minor planet exploration. In contrast to previous ultrasonic rock driller designs, RPUD could exploit longitudinal vibrations generated by piezoelectric ceramics on both sides. In addition to the ultrasonic horn, which transfers the longitudinal vibration to the free mass, a V-LT coupler of the rotary unit on the other side of the piezo-ceramics transforms the longitudinal vibration into longitudinal-torsional vibration, which creates an elliptic trajectory on the top of the V-LT coupler. This elliptical motion drives the rotor to rotate continuously by friction on the contact surface. The RPUD prototype requires a driving frequency of 19.95 kHz, a voltage of 225 V_{pp}, and a preload of 18 N. It can operate at the maximum speed of 117.75 rpm and provides a maximum torque of 38 mNm. They reported that the RPUD prototype has much better drilling efficiency than percussive drilling. While the RPUD prototype drilled 22 mm in 5 minutes and could exceed this value, percussive drilling could only reach the depth of 15.5 mm in five minutes, while further drilling appeared to be inefficient and almost unlikely.

Regarding penetration testing in regolith and granular materials, Firstbrook, Harkness, and Gao (2014) investigated the effects of high-powered ultrasonic longitudinal vibrations on assisting penetration into granular materials. They used an ultrasonic Langevin transducer to provide ultrasonic vibration of 20 kHz up to 10 μm amplitude. A major limitation comes from the design of the ultrasonic horn penetrator, which must amplify the vibration amplitude and penetrate into the granular materials. The horn attaches to the ultrasonic transducer, and then its cross-section must be reduced to concentrate the vibration and increase the amplitude of the vibration. Therefore, only the lower cross-section area of the horn can penetrate, while the rest remains above the surface. To have a 20 cm length of penetration, they designed the horn from 94Ti/6Al/4V alloy to resonate in the second longitudinal mode at 20 kHz with the resulting amplification ratio (gain) of 3.5. They conducted various penetration tests for Martian regolith simulants with different relative densities. A linear actuator was used to provide the penetration at a slow rate of 3 mm/s with an input voltage of 4.81 V and a faster rate with a speed of 9 mm/s with an input voltage of 12 V. Almost in most of the non-ultrasonic penetration tests, they reported a higher penetration force for the slow rate. However, they noticed that the slow rate required a lower penetration force in the ultrasonic penetrations. Moreover, the reduction

in the required penetration force was evident in the ultrasonic penetrations. This reduction was more conspicuous in the higher relative density regoliths. Therefore, the ultrasonic technique seems to be useful for assisting penetration into the lunar regolith, which has a high relative density just a few centimeters below the surface. Also, they observed the maximum rate of reduction in the penetration resistance occurred when they increased the amplitude of vibration from 0 to 1 μm, corresponding to the minimum power consumption (actuator and ultrasonic units). After that, the reduction in penetration force was less conspicuous, indicating that the ultrasonic energy had already fluidized the surrounding regolith near the horn's tip, and expanding the fluidized region became more challenging after a certain point.

In order to examine the effect of gravity in ultrasonic penetration, (Firstbrook, Worrall, Timoney, Suñol, Gao, and Harkness, 2017) conducted a series of penetration tests inside a centrifuge. The tests were conducted in high gravities from 1g to 10g, which allowed them to detect a trend and extrapolate the results for lower gravities. Since their previous study examined the effect of penetration rate and a wider range of ultrasonic vibration amplitude (0-5 into various Martian regolith, in this study, they only used one regolith simulant, a medium-fine sub-rounded quartz-based sand (BP) with a density of 1.79 g/cc, the penetration rate of 9 mm/s with the amplitude range of 0-1.6 μm) in other to focus more on the effect of gravity. They reported higher penetration resistance in higher gravities, while ultrasonic penetration exhibited a higher percentage reduction of the resistance force in lower gravities. For instance, they observed an 80% reduction in penetration force at 1g in comparison to 70% at 5g by applying the amplitude of vibration of 1.6 μm. Subsequently, Firstbrook, Worrall, Timoney, and Harkness (2018) examined the ultrasonic effects on percussive penetration into two regolith simulants. They noticed the number of required strikes to penetrate 190 mm was reduced from 48 to 15 and from 33 to 17 for BP (D_r =48.3%) and SSC-3 (D_r =43.1%), respectively, when they synchronized the ultrasonic vibration pulses with the amplitude of (1.6 μm) with the hammer impacts. Furthermore, they reported that the probe sunk into the granular material for a short time at the beginning of the penetration when they only implemented the ultrasonic vibration. They didn't observe this effect at the larger depths of penetration. Finally, Firstbrook, Worrall, Harkness, Flessa, McGookin, and Thomson (2018) studied the effects of ultrasonic longitudinal vibrations on assisting rotary penetration of an auger drilling rig into glass microspheres with a particle size distribution of 150-250 mm. They noticed that not only the ultrasonic vibration effects are lower than the rotation effect in reducing the maximum

overhead force, but it also has no apparent result in reducing the maximum penetration force in rotary drilling. However, they observed that increasing the amplitude of vibration decreased the required maximum torque of 120 Nm in non-ultrasonic rotary drilling to 85 Nm (30% reduction) in ultrasonic rotary drilling with the amplitude of 10 μm.

In the reviewed literature on longitudinal vibration applications, penetration is limited to the horn's tip up to where its cross-section increases and it connects to the ultrasonic transducer. Typically, the cross-section at this connection point between the transducer and the horn is similar, with the horn narrowing towards the tip. This tapering, a common feature in existing ultrasonic systems, is designed to efficiently transmit and focus the ultrasonic waves. Therefore, this design restricts full probe penetration into soil sub-layers. Moreover, despite existing research on high-power longitudinal vibrations, biological locomotions like those observed in snakes, horned lizards (Sherbrooke and Nagle, 1996), and sandfish (Baumgartner, Fidler, Weth, Habbecke, Jakob, Butenweg, and Böhme, 2008) leverage low-frequency bending vibrations for digging or hiding in granular materials. Additionally, (Alaei Varnosfaderani, Maghoul, and Wu, 2022) demonstrated through the Discrete Element Method (DEM) simulations that lateral vibrations at higher frequencies or amplitudes significantly reduce penetration force in granular materials. However, these simulations assume a rigid probe structure, indicating a need for further exploration of bending vibrations' effects.

Therefore, inspired by the bending vibration of biological locomotions in granular materials, our study aims to experimentally investigate the influence of bending vibration across various resonance frequencies in assisting penetration. Inducing bending vibrations in a structure can be efficiently achieved by applying AC voltage to thin piezo actuator patches on the structure's surface (Dosch, Inman, and Garcia, 1992; Dimitriadis, Fuller, and Rogers, 1991). Accordingly, we excited bending vibrations by attaching thin piezo patches to the machined surface of the probe structure without expanding its outer dimensions. Also, it is possible to attach the piezo patches inside the probe surface. This approach allowed us to fully bury the entire probe-actuator system into granular materials for practical applications.

5.2 Experimental Apparatus

In this study, we have designed and fabricated a circular probe-actuator configuration to study the effects of bending vibration on soil resistance against probe penetration. Detailed

explanations of each component and element of the test setup are provided in the following. First, we described the main components that are shared between different rig penetration tests. Next, we showed the probe configuration. Then, we explained our modal test setup. Finally, we presented the specifications of the granular material used in this investigation.

5.2.1 Main Components

Figure 5.1 displays the penetration test setup. In particular, Figure 5.1a illustrates the schematic of the setup with its components. Additionally, Figure 5.1b shows the real set-up with an undisturbed sample prepared for penetration tests. The linear actuator is connected by a coupling to the probe assembly and pushes the probe into the soil. The required input voltage is 12 V DC, and the maximum speed is 10 mm/sec. By reducing the input voltage, we can decrease the penetration speed. The lever mechanism, designed and fabricated using three-dimensional (3D) printing technology, is positioned between the force sensor and the linear actuator. The sensor, linear actuator, and lever mechanism are installed on a base plate. The supporting beam holds the base plate and is connected to our laboratory's fixed supporting frame. The clamps are also printed with the 3D printer, and they are designed only to prevent falling and side movements of the linear actuator-probe assembly.

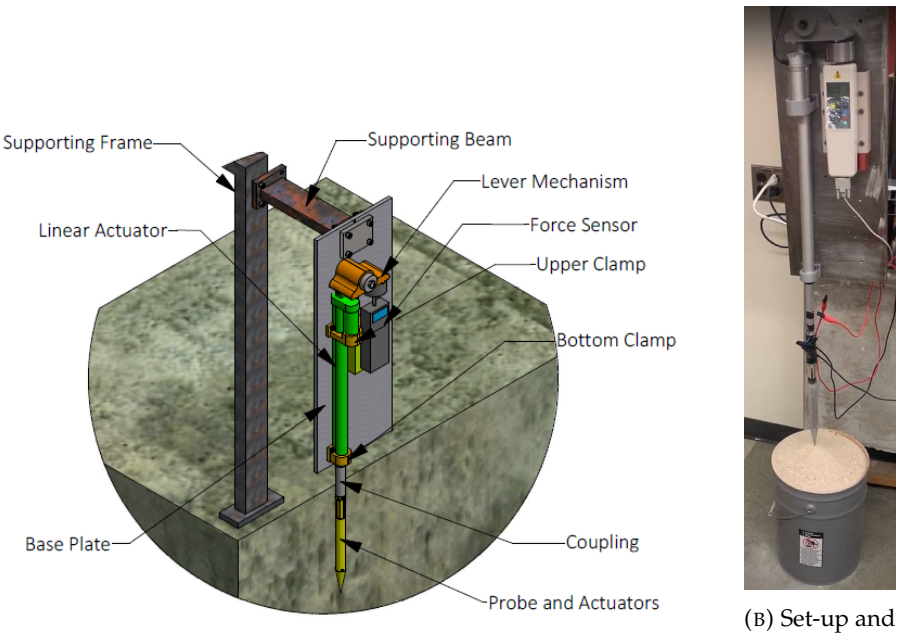

(A) Schematic of the set-up and components

(B) Set-up and sample

FIGURE 5.1: Configuration of the penetration test set-up

5.2.2 Rigs Configuration

Figure 5.2 illustrates the configuration of the probe-coupling assembly and the positioning of the piezo patches on the Aluminium probe. More detailed drawings have been provided in the Appendix B. In our approach, we have machined the outer surface of the probes to facilitate the attachment of the piezo patches. These patches are thin and, when glued to the machined surface, do not increase the overall perimeter of the probe. This design allows us to push the probe and piezo patches together into the soil. However, to safeguard the piezo patches from potential contact and wear caused by the soil, we limit the insertion depth to 24 cm. It is important to note that, for practical implementation, it's possible to securely place the piezo patches inside the tube using advanced machining and manufacturing techniques. This ensures their protection from direct contact with the abrasive granular materials. The piezo patches used in this setup have dimensions of 49.7 mm $\times$ 7.00 mm $\times$ 0.80 mm, and they are made from PZT material (No. 850 (APC International, Ltd, 2021)). In Figure 5.2b, the cross-sectional areas of the piezo patches attached to the machined surface of the probes and their polling directions are shown. We utilized two sets of piezoelectric patches placed on parallel machined surfaces. In each set, the piezo patches have the same poling direction.

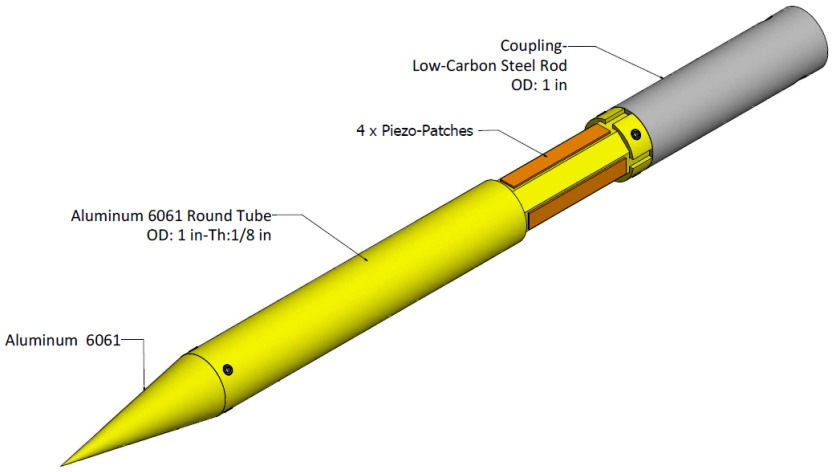

(A) Probe coupling Assembly

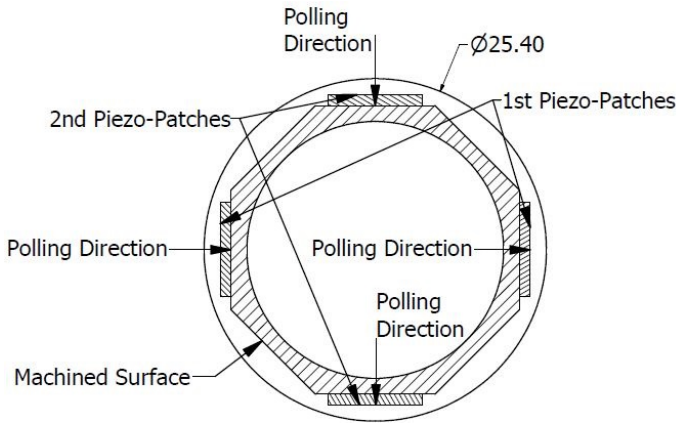

(B) Probe actuators configurations

FIGURE 5.2: Probe Configuration

Figure 5.3 displays how electrical circuits are employed to generate bending vibrations in various directions within the probe structure. By applying an AC voltage to the outer electrodes of a specific set of piezo patches, we can induce one-directional bending vibration in the structure. This vibration occurs parallel to the polling direction of that particular set of piezo patches. It's essential to maintain a ground connection at the interface between the probe and the piezo patches to carry out this process. In Figure 5.3a and Figure 5.3b, the required electrical circuits for generating unidirectional bending vibrations are presented, with the vibration direction indicated in each figure. In addition, we can create chaotic bending motions or whirling motions if we use the electrical circuit illustrated in Figure 5.3c. Applying an AC voltage to the outer electrodes of one set and another AC voltage (with a different frequency) to another set and grounding inner electrodes induce complex bending motions in two directions within the probe structure. This results in a chaotic horizontal movement at the tip of the probe. However, if the second signal has the same frequency as the first one but with a precise phase difference of 90 degrees, the bending vibrations in

two directions generate a circular whirling motion in the probe structure and at its tip.

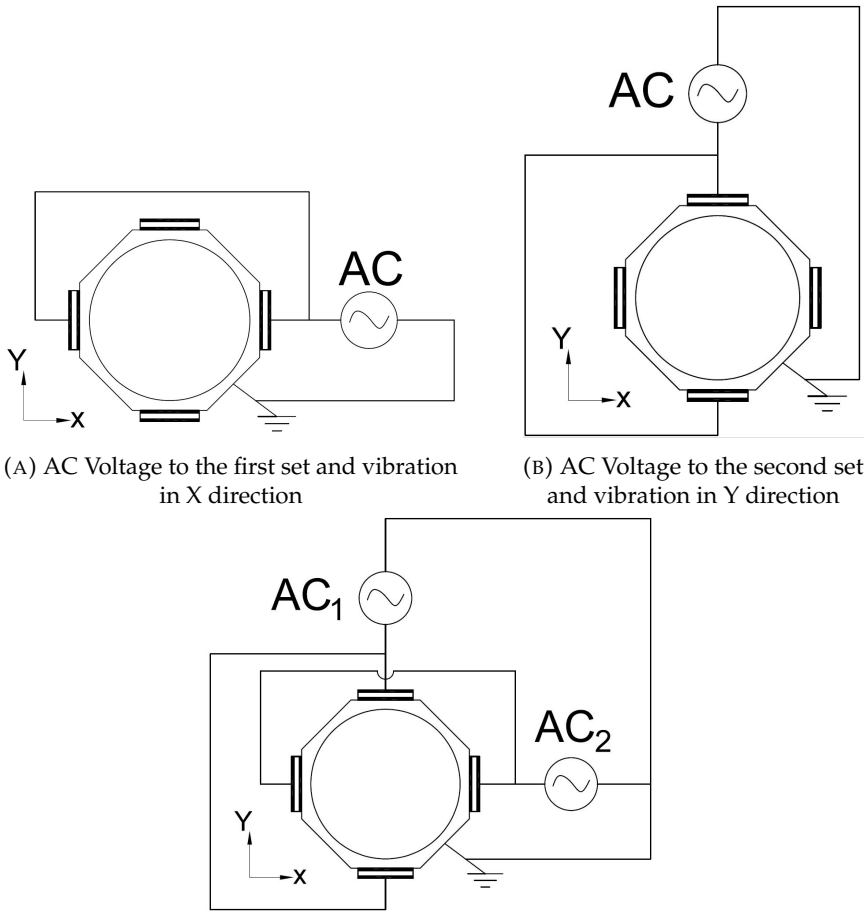

(A) AC Voltage to the first set and vibration in X direction

(B) AC Voltage to the second set and vibration in Y direction

(C) Complex vibration/Whirling motion excitations

FIGURE 5.3: Applying voltage and exciting bending vibrations in different directions

5.2.3 Signal Generator and Data Acquisition System

Our signal generator and data acquisition system is a four-channel Siemens LMS SCADAS mobile integrated with LMS Test Lab software. Figure 5.4 shows the schematic of our modal test. The signal generator creates the required AC voltage, and it will be applied to the piezoelectric actuators attached to the probe structures. The input signal can be generated by either our LMS software or 33120A Agilent Arbitrary Waveform Generator. The applied voltage creates vibration in the probe structure. To measure the resulting lateral velocity at the probe tip, we used a laser vibrometer sensor. This sensor consists of a Polytec OFV-5000 Vibrometer controller and a Polytec OFV-505 Vibrometer Sensor Head. The sensor head detects the lateral velocity and provides a corresponding voltage signal, which is then transmitted to the data acquisition system. Finally, the LMS Test Lab software shows and saves all the input voltage signals and the recorded velocities.

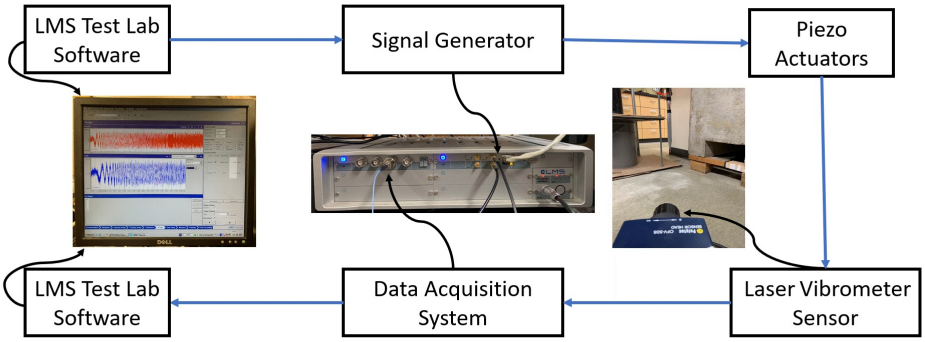

FIGURE 5.4: Modal test setup

In the penetration test, the resonance voltage signal(s) generated by the signal generator will be amplified through the amplifiers to reach V_{max} = 200 V. Then, the amplified signals will be applied to the piezoelectric actuators.

5.2.4 Soil Properties

The soil sample consists of fine-cutting sub-angular limestone particles, as shown in Figure 5.5 with the maximum and minimum dry density of 1950 Kg/m^3 and 1610 Kg/m^3, respectively. The limestone sample contains particles, with nearly 60% of its weight having particles finer than 0.42 mm.

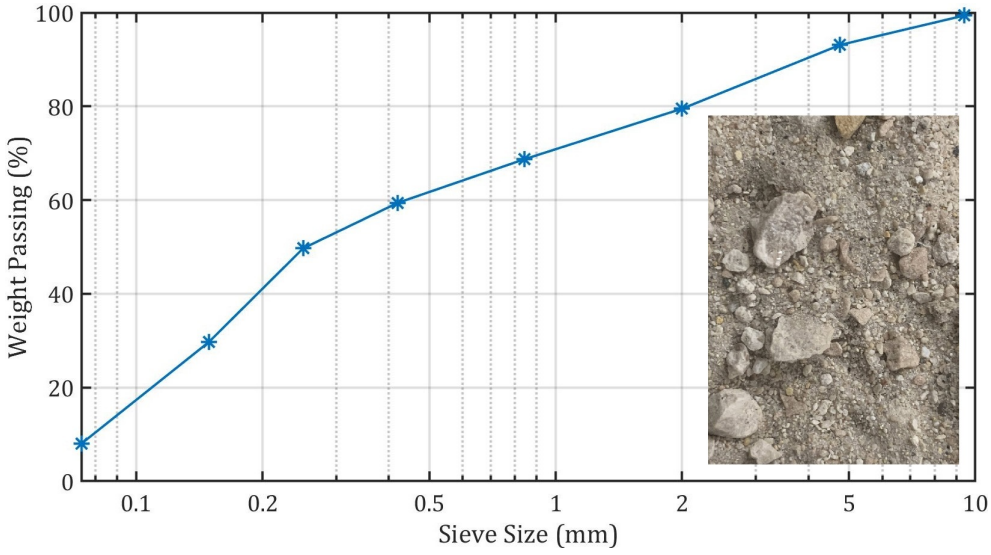

FIGURE 5.5: particle size distribution

In order to ensure the proper mixing of granular particles to achieve a homogeneous distribution and obtain consistent results, it is recommended to pour the material from a height greater than 40 cm, as stated by (Firstbrook, Harkness, and Gao, 2014). Taking this into account, we have devised a setup consisting of a container with a built-in cone, a stand, and a steel pail. The container is positioned above the stand, enabling a hands-off pouring of sand into the pail located at the base of the stand (Figure 5.6). The hands-off approach is beneficial for maintaining consistent results. The bottom of the container is positioned approximately 100 cm above the pail to ensure that the granular particles receive a sufficient fall distance. The process results in medium-dense sand with a bulk density of around 1790 Kg/m^3 and a relative density of 58%. Additionally, the pail used for this procedure has a diameter of 28.8 cm and a height of 40 cm. It is worth noting that the pail's diameter is over 11 times larger than the diameter of the probe to ensure minimal boundary effects during the penetration tests, as noted by (Bolton, Gui, Garnier, Corte, Bagge, Laue, and Renzi, 1999).

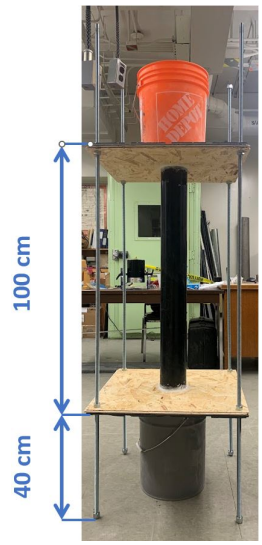

FIGURE 5.6: Hands-Off Approach to Pouring Sand into the Pail

5.3 Experimental Procedure and Results

In this section, we begin by presenting the penetration test results for the non-vibrating probe. Following this, we conducted modal tests in subsequent sections to identify various resonance frequencies and mode shapes of the probes. Subsequently, rapid penetration tests were performed to pinpoint the most promising and beneficial resonance vibrations for penetrations. Finally, we present and discuss a series of penetration tests that utilize

the most effective resonance modes to reduce the required vertical force for penetrating the probe.

5.3.1 Non-Vibrating Probe Penetration Tests

Figure 5.7 displays the recorded forces of three consecutive tests performed on undisturbed samples without applying any vibration (non-vibrating probe) along with the average (AVG) penetration forces for these three tests. As can be seen, there is a distinct peak in the magnitude of the recorded penetration force precisely when the linear actuator terminates the penetration process at around 61 sec. Throughout the actuator's operation, a slight deflection in the frame was observed. It was expected that the penetration force would drop to zero immediately when the linear actuator stopped working. However, the deflected frame caused the recorded penetration force to drop only slightly to a semi-steady state. In fact, upon stopping the linear actuator at the end of penetration, the deflected frame shape pushed the probe into the soil to return to its initial shape and release stresses. However, as the penetration force from the deflected frame was insufficient for an immediate complete return, the frame remains deflected, leading to a very gradual reduction in the recorded force and the observation of a semi-steady state. The penetration process typically lasts for about 61 seconds, with a penetration rate of 4 mm/sec for all tests. For the non-vibrating probe penetration (Figure 5.7) and the subsequent tests with the vibrating probe (5.3.5), we extended our recordings to 120 seconds. This extension enables us to assess the impact of bending vibration on two aspects: first, the reduction in penetration force as the probe penetrates the soil (prior to t$\approx$ 61 sec), and second, the damping of the peak force when the linear actuator stops (beyond t $\approx$61 sec).

It's worth noting that the recorded forces remain at zero for the approximately initial 25 seconds in Figure 5.7. During this period, as the linear actuator is extending, the combined weight of the probe and actuator is sufficient to drive the probe into the soil sample. Beyond this point, the probe can no longer advance based on its own weight alone. Therefore, the linear actuator provides the extra required force, which is supported by the lever mechanism, and recorded by the force sensor.

Additionally, the maximum deviation in peak force from the average curve is approximately 4% (Figure 5.7). Moreover, when the system reached the semi-steady state at t=120 seconds, the deviation was less than 4%. In 5.3.5, we employed this average plot for comparative analyses with the penetration forces in the presence of bending vibrations.

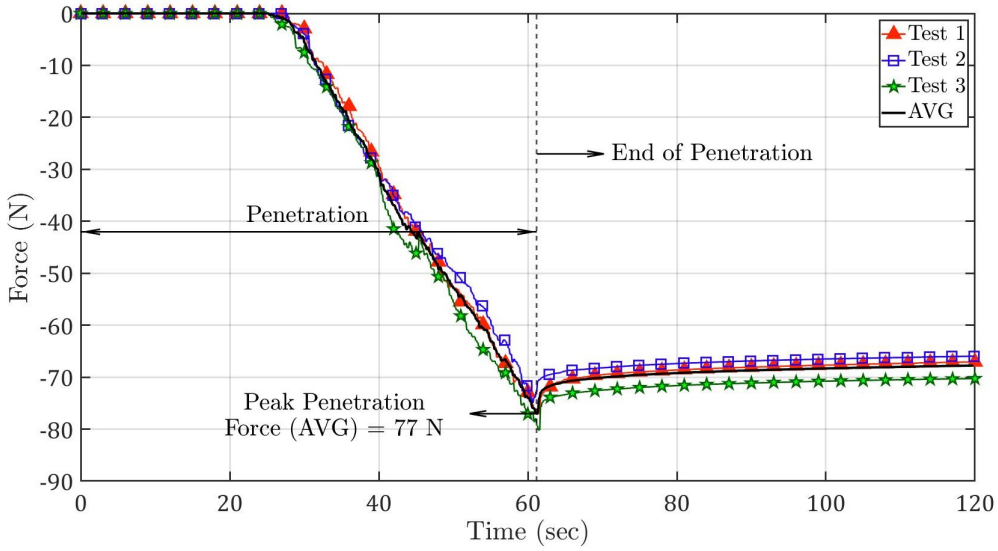

FIGURE 5.7: Penetration Force of Non-Vibrating probe

5.3.2 Modal Analysis

In the modal tests, we applied a chirp signal to each set of actuators separately to measure the velocity of the probe tip and identify its bending vibration resonance modes. The chirp signal had a maximum voltage of $V_{max} = 10$ V, with the frequency sweeping from 10 Hz to 20.480 kHz (the maximum frequency of the signal generator). The spectrum diagram of the input signal is depicted in Figure 5.8.

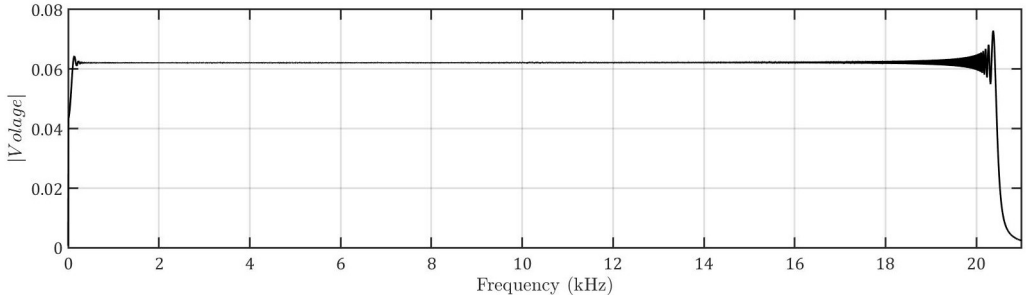

FIGURE 5.8: Single-sided amplitude spectrum of the input voltage

For each set of piezoelectric patches, we began by exciting the piezoelectric in front of the laser vibrometer sensor (Figure 5.9a). This induced a bending vibration with waves traveling on one side of the probe. Subsequently, we activated the second piezoelectric patch in the same set, producing a similar bending vibration pattern on the opposite side (Figure 5.9b). Lastly, both piezoelectric patches were activated simultaneously, leading to a combined vibration effect (Figure 5.9c). This entire process was then repeated for the second set.

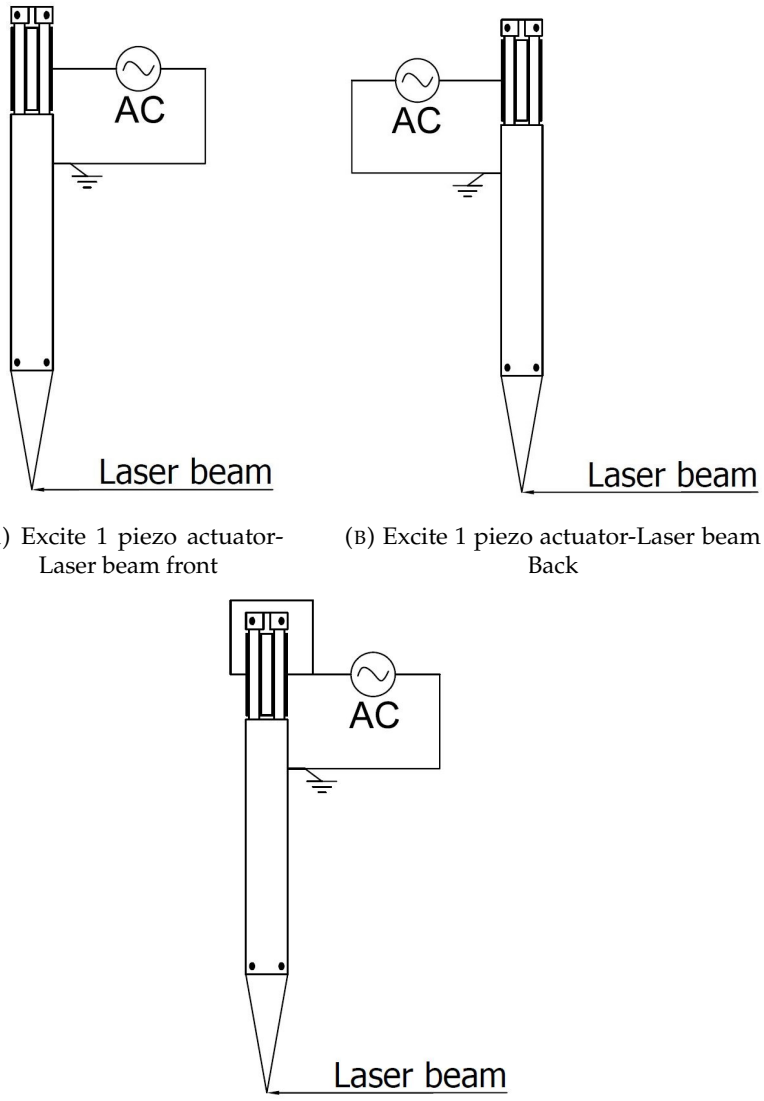

(A) Excite 1 piezo actuator-Laser beam front

(B) Excite 1 piezo actuator-Laser beam Back

(C) Excite 2 piezo actuators together

FIGURE 5.9: Bending vibration and laser beam direction

Figure 5.10 displays the amplitude spectrum of the probe tip's speed in two distinct directions. The first direction corresponds to the activation of the first set of piezo actuators, while the second direction, perpendicular to the first one, corresponds to the activation of the second set of piezo actuators. The directions 1 and 2 here are corresponding the X and Y directions shown in Figure 5.3. Figure 5.10a shows the results for the first direction, while Figure 5.10b is related to the second direction. Both Figure 5.10a and Figure 5.10b demonstrate that when a single piezoelectric patch is active in a set, the responses at the probe tip are quite similar to when the other patch is active alone in the same direction. Additionally, exciting both piezoelectric patches simultaneously approximately doubles the vibration speed in each direction. This consistent outcome is a result of the similar

properties of the piezoelectric patches and also indicates a reliable and consistent bond between the patches and the probe.

It's worth noting a slight difference in the natural frequencies between the two directions. For example, we have a bending resonance mode of $f_1 = 6069$ Hz in the first direction, and this mode is $f_2 = 5886$ Hz in the second direction. In an ideal scenario, symmetrical probes would have the same resonance frequencies for similar bending modes in both directions ($f_1 = f_2$). However, small differences due to manufacturing or gluing the piezoelectric patches can lead to slight frequency deviations. At higher resonance frequencies, like around 9405 kHz, the differences in vibration become more noticeable. This is probably because the higher the frequency, the more these vibrations are affected by small imperfections or inconsistencies in how the piezoelectric patches are attached and the probe's overall symmetry. To simplify, when we discuss a specific bending mode regardless of its direction, we represent it with its corresponding average frequency (e.g., bending mode at $f_{avg} = 5978$ Hz refers to bending modes $f_1 = 6069$ Hz in the first direction and $f_2 = 5886$ Hz in the second direction).

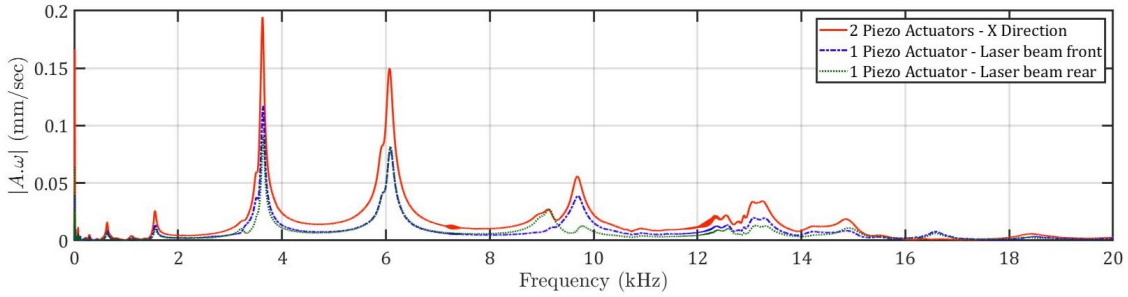

(A) Direction 1

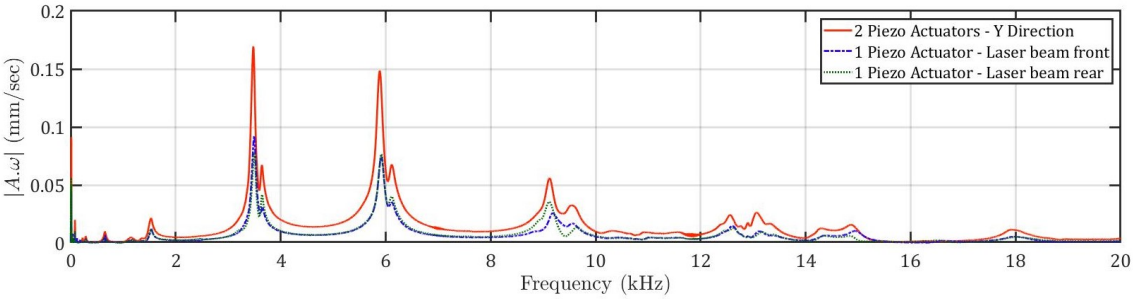

(B) Direction 2

FIGURE 5.10: Single-sided Amplitude Spectrum of Probe Tip Velocity

After recording the velocity, we further transformed it into displacement and acceleration measurements. Figure 5.11 illustrates the FFT of the probe tip's displacement, velocity, and acceleration. Upon observing Figure 5.11c, it becomes evident that the acceleration of the probe's tip is not notably prominent below 3000 Hz when compared to the broader

frequency range of 3-20 kHz. Furthermore, Figure 5.11a indicates the displacement of the probe's tip remains minimal above 10 kHz (within the 10-20 kHz range) compared to the rest of the probe tip's frequencies (0-10 kHz). Consequently, we can reasonably estimate that the most effective resonance modes for fluidizing the sand are most likely situated within the frequency range of 3-10 kHz. This range exhibits notably higher levels of both displacement and acceleration compared to the entire frequency spectrum.

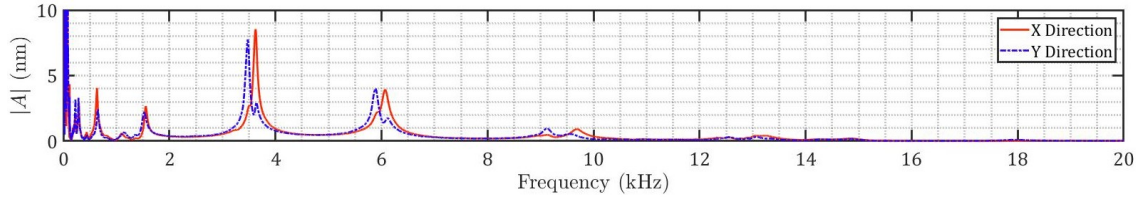

(A) Displacement Amplitude Spectrum

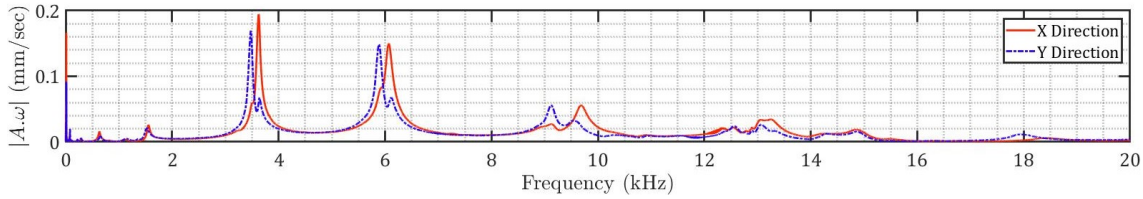

(B) Velocity Amplitude Spectrum

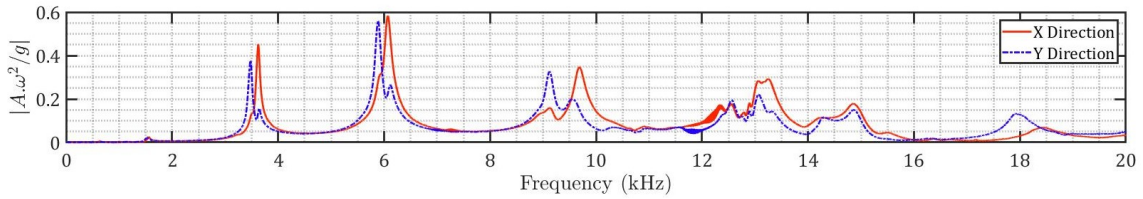

(C) Acceleration Amplitude Spectrum

FIGURE 5.11: Single-sided Amplitude Spectrum of Probe Tip

5.3.3 Preliminary Penetration Tests

Initially, our objective is to identify bending resonance modes that can fluidize the soil sample for subsequent primary penetration tests. We used the linear actuator to push the probe into the soil at various depths to achieve this objective. When the penetration process stops, the force in the structure does not drop to zero due to the slight deflection of the frame, and the force sensor indicates that the probe is under compression. Following this, we used an amplifier to apply a voltage of V_{p-p} = 400 V at various resonance frequencies to the piezo patches. If a bending resonance frequency proves effective in fluidizing the soil, the stress in the structure is released, resulting in a decrease in force as indicated by the force sensor. Our findings revealed that resonance frequencies below 3000 Hz have no noticeable effect on soil fluidization and are ineffective in reducing the force in the force sensor. This is because the acceleration amplitude at frequencies below 3000 Hz is

very low when compared to the rest of the frequency range. Acceleration plays a crucial role by imparting enough inertia force to the soil particles, allowing them to shift away from the probe's tip. On the other hand, within the 10-20 kHz range, even with the high level of acceleration of the probe tip compared to the other resonance modes in the whole frequency range, only vibrations at 13250 Hz showed limited potential in our preliminary penetration tests to reduce the penetration force. This can be attributed to the amplitude of displacement at a frequency range of 10000 Hz to 20000 Hz, which is very low compared to the resonance modes between frequencies of 0-10 kHz. The amplitude of displacement needs to reach a significant level to effectively transfer the vibration energy to the soil particles, as pointed out by (Alaei Varnosfaderani, Maghoul, and Wu, 2022). Conversely, resonance frequencies of f_1=3626 Hz, f_1=6069 Hz, and f_1=9688 Hz along the direction 1 noticeably reduced the force to zero, indicating their effectiveness in soil fluidization. This is because the resonance frequency within the 3-10 kHz range demonstrates significantly higher levels of both displacement and acceleration when compared to the entire frequency spectrum. Therefore, these frequencies have been selected for the main penetration tests. Also, for inefficient modes, we chose 1554 Hz and 13250 Hz as they exhibit the highest acceleration below 3000 Hz and above 10000 Hz, respectively. Additionally, 13250 Hz showed slight potential for soil fluidization.

5.3.4 Finite Element Analysis

In our study, finite element analysis (FEA) was employed to model the experimental setup using ABAQUS in order to visually demonstrate the specific mode shapes that we excite during soil penetration tests. The model included several components: the probe itself, the coupling mechanism, piezoelectric patches, and the shaft that connects to the linear actuator. The model was built with 352,804 nodes and 239,394 elements. It utilized 237,082 C3D10 quadratic tetrahedral elements for the structural parts and 2,312 C3D10E elements for the piezoelectric patches. The resulting mode shapes are depicted in Table 5.1.

TABLE 5.1: Bending Mode Shapes Used for Penetration Tests

X Direction	Y Direction
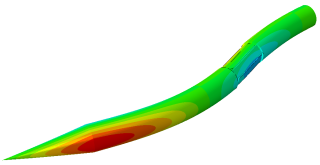	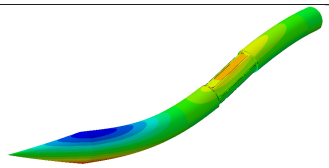
(A) 1541.4 Hz	(B) 1541.6 Hz
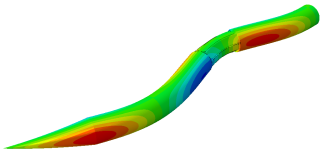	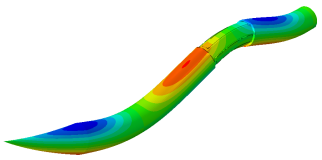
(C) 3037.4 Hz	(D) 3039.0 Hz
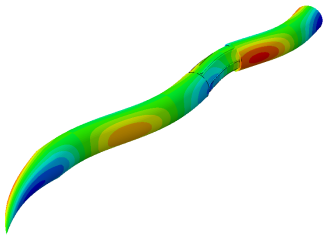	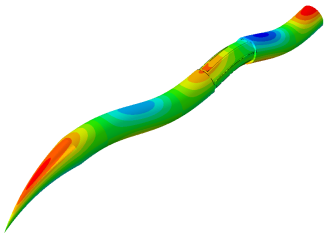
(E) 6256.6 Hz	(F) 6258.3 Hz
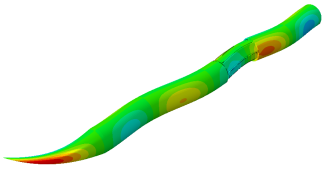	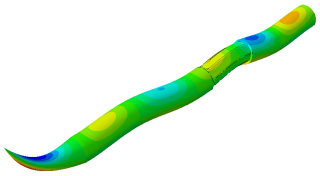
(G) 9797.5 Hz	(H) 9797.2 Hz
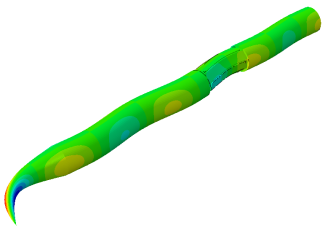	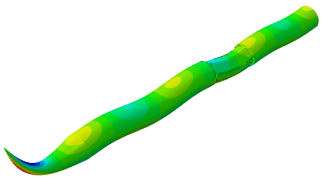
(I) 14055 Hz	(J) 14056 Hz

Furthermore, we performed a comparison between the average bending frequencies obtained from the ABAQUS simulations and those measured during our laboratory tests, as shown in Table 5.2.

TABLE 5.2: Comparison of Average Bending Frequencies

AVG From Abaqus	AVG from Modal Tests	Difference %
1541.5	1543	1.0%
3038.2	3553	14.4%
6256.4	5978	-4.6%
9797.3	9405	-4.2%
14055.5	13159	-6.8%

While our simulation results successfully approximated the natural frequencies and mode shapes, modeling the complex entire system posed significant challenges. The system's dynamic response is influenced by the integrated assembly of the probe, coupling, linear actuator, base plate, supporting beam, and frame, which complicates the simulation. Notably, slight deflections in the support structure during penetration underscored the interconnectedness of system components and their impact on the system's dynamic response. Therefore, FEA was primarily leveraged to illustrate the resonance mode shapes critical for our penetration tests.

5.3.5 Main Penetration Tests

5.3.5.1 Uni-direction Bending Vibration

In this section, we performed diverse penetration tests, recording the necessary penetration force at different frequencies to assess and compare the results with the average penetration forces of the non-vibrating probe in Figure 5.7. As discussed above, Figure 5.3a and Figure 5.3b demonstrate the driving electrical circuit diagram used to induce bending vibrations in the X and Y directions, respectively. Figure 5.12 compares the penetration force of the probe when it is non-vibrating with the vibrating one at the frequencies of 1554 Hz and 13250 Hz. Given the anticipated 4% difference in test results, Figure 5.12 indicates no improvement in the peak penetration force at these resonance modes. When the linear actuator is stopped at the end of the penetration (around 61 sec) at 13250 Hz, there is only a minor enhancement in damping the peak force. This slight improvement is likely due to the high acceleration of the probe (Figure 5.11c). However, as discussed in 5.3.3, the bending vibration displacement amplitude at the probe's tip above 10 kHz is not sufficiently large (Figure 5.11a). This prevents the efficient transfer of vibrations to the surrounding sand. Furthermore, there is no noticeable improvement in penetration

tests at the frequency of 1554 Hz. This lack of improvement is attributed to the insufficient acceleration of the probe tip (Figure 5.11c), which fails to provide the necessary inertia for soil particles to initiate movement and fluidization.

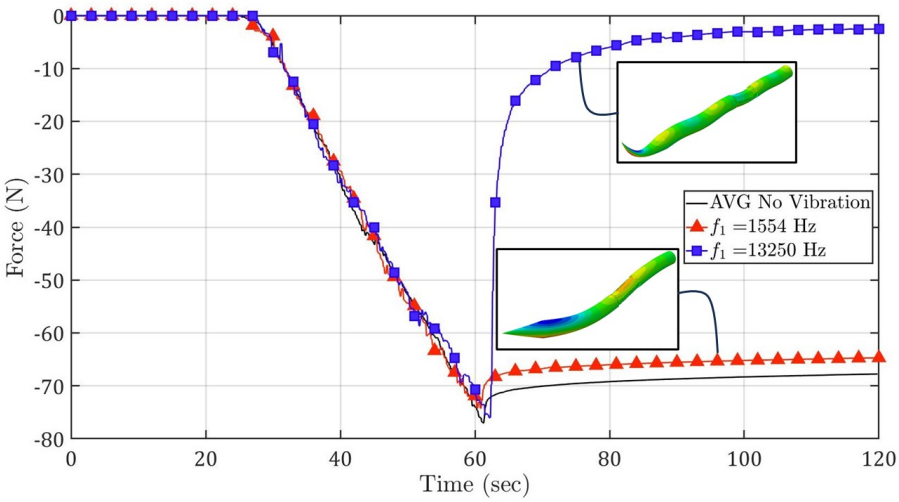

FIGURE 5.12: Penetration force with inefficient modes of vibration

Figure 5.13 presents a comparison of penetration forces under more favorable bending vibration modes against penetration forces without vibration. Each drawing compares average penetration forces without and with vibration at a specific bending resonance mode. These modes are denoted as f_1 for the first direction and f_2 for the second direction as described in 5.3.2. The average penetration force at these modes (f_1 and f_2) is also indicated in each figure.

In Figure 5.13a, the resonance frequencies are f_1=3626 Hz for the first direction and f_2=3479 Hz for the second direction. Figure 5.13a indicates that this bending vibration mode had minimal impact on reducing penetration force during the sand penetration process. Notably, they did not significantly affect the maximum penetration force either. However, a significant decrease in the peak force magnitude was observed once the linear actuator ceased its motion. The average curve shown in Figure 5.13a indicates that, in this vibration mode, the force took approximately 2.3 seconds to reach zero after the probe stopped its penetration. In contrast, without vibration, there was only a 12% reduction in peak force at t=120 sec (59 sec after the probe stopped penetrating). This suggests that this vibration mode could be most advantageous when the probe experiences frequent pauses and restarts or when it moves at a very slow penetration rate.

In Figure 5.13b, the resonance frequencies are f_1=6069 Hz for the first direction and f_2=5886 Hz for the second direction. This figure also presents average penetration forces

for these vibration scenarios and the non-vibrating probe. In Figure 5.13b, resonance frequencies are f_1=9688 Hz for the first direction and f_2=9122 Hz for the second direction. For a better comparison with non-vibrating probes, Figure 5.13d displays average penetration forces for vibro-probes from Figure 5.13a to Figure 5.13c and to the non-vibratory probe. Moreover, we extract key parameters, including the maximum penetration force ($F_{\max}$), the reduction in maximum penetration force (R%), and the release time ($t_{\max}$) required for the force to drop to zero when the probe stops at the end of penetration, from the findings in Figure 5.13c. These results are summarized in Table 5.3. Vibration modes at f_{avg} =5915 Hz and f_{avg} =9833 Hz in both directions considerably reduce penetration forces. However, the lower frequency mode (f_{avg} = 5915 Hz) demonstrates a more pronounced reduction. In Figure 5.13, vibrating at f_{avg}=5915 Hz reduces maximum penetration forces by 28% (from 77 N to 55.5 N) and eliminates the penetration force within 1.15 seconds. On the other hand, vibrating at f_{avg}=9800 Hz reduces maximum penetration forces by 21% (from 77 N to 60.8 N), with the peak force dissipating over 4.4 seconds.

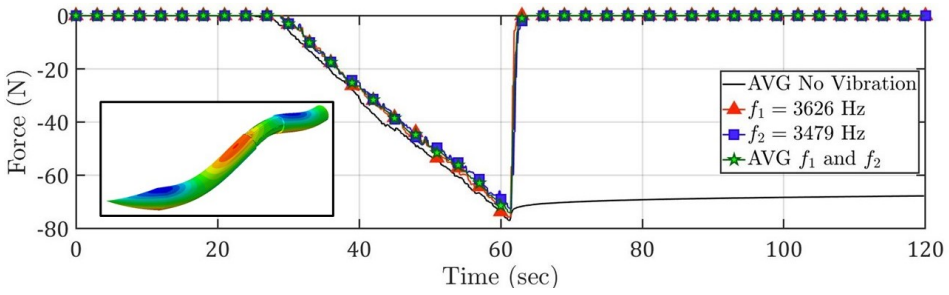

(A) $f_1 = 3626$ and $f_2 = 3479$ Hz

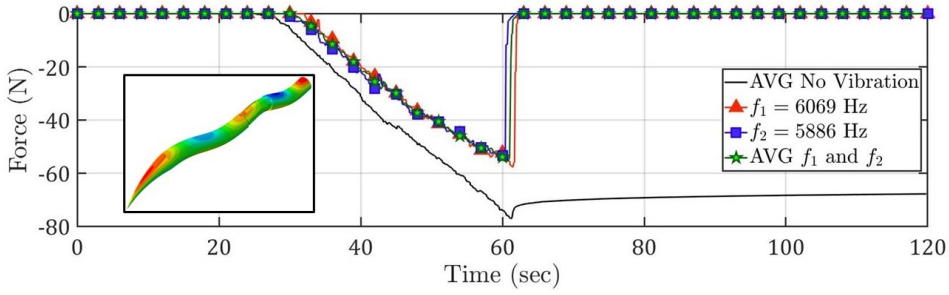

(B) $f_1 = 6069$ and $f_2 = 5886$ Hz

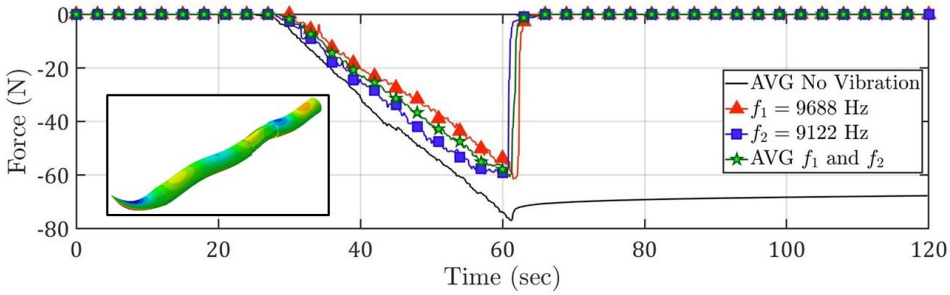

(C) $f_1 = 9688$ and $f_2 = 9122$ Hz

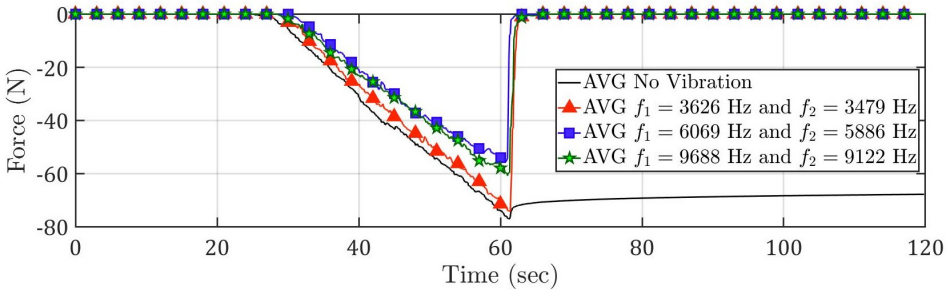

(D) Average penetration force

FIGURE 5.13: Penetration force at efficient bending Modes

f_{avg} (Hz)	F^a_{max} (N)	R^b(%)	$t_r{}^c$(sec)
0	77	–	–
3553	74	4%	2.3
5978	56	28%	1.4
9405	61	21%	4.4

[a] Maximum Penetration Force in Newton
[b] Percentage of Maximum Force Reduction
[c] Release Time in seconds

TABLE 5.3: Penetration forces in one-directional excitation

5.3.5.2 Bi-direction Bending Vibration

Moving forward, we investigate the effects of bi-directional excitation on the piezo probe with the combination effects of the efficient bending modes. In this approach, we apply an AC voltage to the first set of piezoelectric elements and another AC voltage to the second set (Figure 5.3c). The two signals either share the same frequency with a 90-degree phase difference or have different frequencies. As a result, the probes generate bending vibrations in both directions. When the frequencies are similar with a 90-degree phase difference, this results in a whirling circular motion in the probe. Alternatively, if there are two distinct frequencies of bending vibration in each direction, it leads to chaotic motion in the probe. Utilizing the recorded velocity data at the probe's tip (Figure 5.10), corresponding to the input chirp signal (Figure 5.8), we calculated the probe's tip displacement in the XY plane resulting from harmonic excitations in both directions. In the analysis of whirling motion, the excitation frequency for each resonance mode is identified as the average of the resonance frequencies in the X and Y directions. This averaged frequency is then applied to both sets of piezoelectric patches. Figure 5.14 presents the displacement of the probe tip for the three predominant resonance modes. The resulting trajectory predominantly exhibits an elliptical shape and is within a timeframe of $\Delta t = 3.8 \times 10^{-4}$ seconds. However, the ellipse's orientation dynamically shifts because the excitation frequency is finely tuned to approximate the average frequency of the two similar bending resonances across different directions. The capacity for the trajectory to change direction offers a significant advantage for penetration, as it allows the probe to uniformly and effectively fluidize the soil in every direction surrounding the probe, thereby facilitating enhanced penetration capabilities.

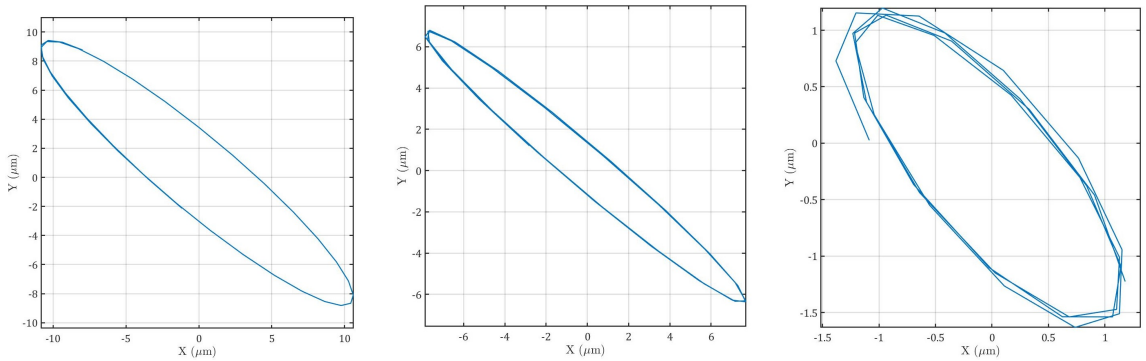

(A) f_{avg}= 3553 (Hz) (B) f_{avg}= 5978 (Hz) (C) f_{avg}= 9405 (Hz)

FIGURE 5.14: Trajectories of the probe tip's whirling motion for three effective resonance modes.

For the chaotic probe motion, wherein two distinct resonance modes are excited in

different directions, the excitation frequency corresponds precisely to the resonance frequency specific to each direction. Therefore, the trajectory of the probe's tips, as depicted in Figure 5.15, exhibits chaotic motion within the XY plane, attributable to the differing excitation frequencies. Similar to the whirling motion, such chaotic behavior plays a significant role in fluidizing the soil uniformly across the XY plane and, therefore, increasing the probe's penetration efficiency.

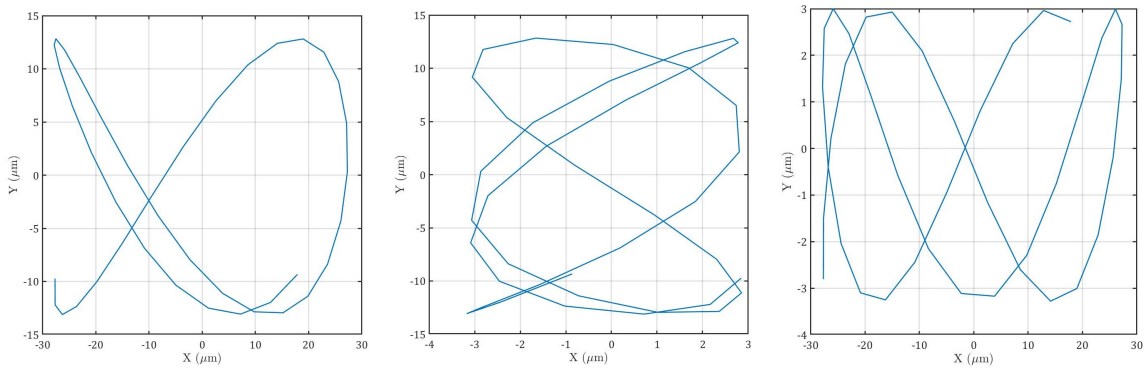

(A) f_1= 3626 (Hz), f_2= 5886 (Hz) (B) f_1= 9688 (Hz), f_2= 5886 (Hz) (C) f_1= 3626 (Hz). f_2= 9122 (Hz)

FIGURE 5.15: Trajectories of the probe tip's chaotic motion.

The outcomes for the penetration tests are presented in Figure 5.16. The maximum penetration force and the time when it drops to zero when the probe stops have improved for all three combinations. For a better comparison of the results, we presented them in Table 5.4. When comparing the results of bidirectional excitation (refer to Figure 5.16 and Table 5.4) with unidirectional excitation (see Figure 5.13 and Table 5.3), it is evident that bidirectional excitation significantly reduces penetration forces and accelerates the force drop to zero when the probe stops penetrating.

In unidirectional excitation, a maximum 27% reduction in penetration forces was observed at 5978 Hz. However, bidirectional excitations produced more substantial reductions, ranging from 33% to 42% for chaotic motions and 15% to 41% for whirling motions. Notably, the 15% improvement is seen in the 3553 Hz whirling motion, a significant enhancement compared to the 4% reduction with the signal applied in only one direction.

From Table 5.4, it is apparent that the most effective reduction in penetration force occurs with at least 9405 Hz in one direction. The optimal case is when this mode is applied in two directions, resulting in a 42% drop in maximum penetration force from 77 N in the non-vibrating probe to 45 N. The time for the force to drop to zero upon cessation of penetration is reduced to 1 second compared to 4.4 seconds when applied in

one direction. When applying an AC signal with 9405 Hz in one direction and 3553 Hz or 5978 Hz in another direction, the reduction in maximum penetration forces is 42% and 35%, respectively, with release times of 2 seconds and 0.8 seconds, respectively.

Table 5.4 also indicates that the quickest reduction in penetration forces upon the probe's penetration cessation occurs when the frequency is 5978 Hz in at least one direction. For example, the release time is 0.7 seconds when both directions have 5978 Hz excitation voltage and 0.8 seconds when one direction has 5978 Hz and the other is either 9405 Hz or 3553 Hz. In contrast, the release times were longer when excitations were applied in one direction (uni-direction Bending Vibration), specifically 1.4 seconds, 2.3 seconds, and 4.4 seconds when the voltage was 5978 Hz, 3553 Hz, and 9405 Hz, respectively.

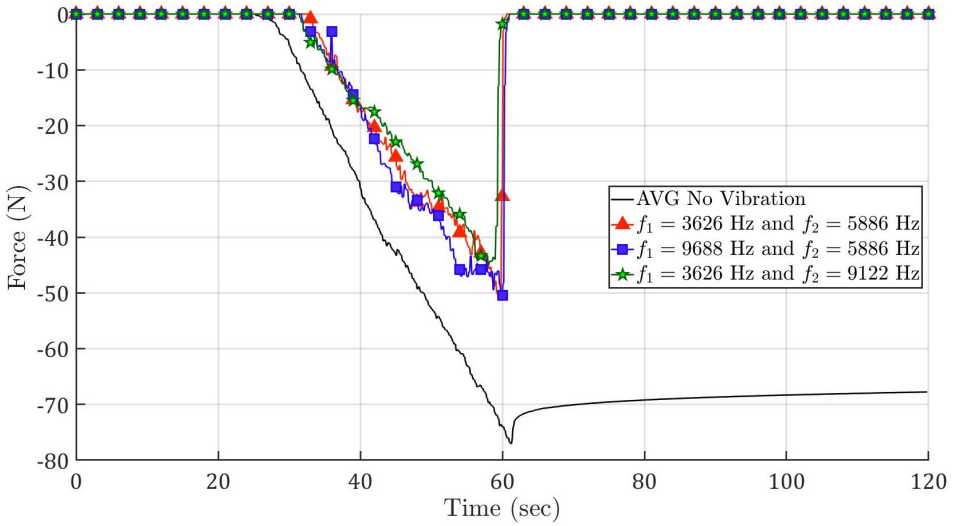

(A) Chaotic probe motion

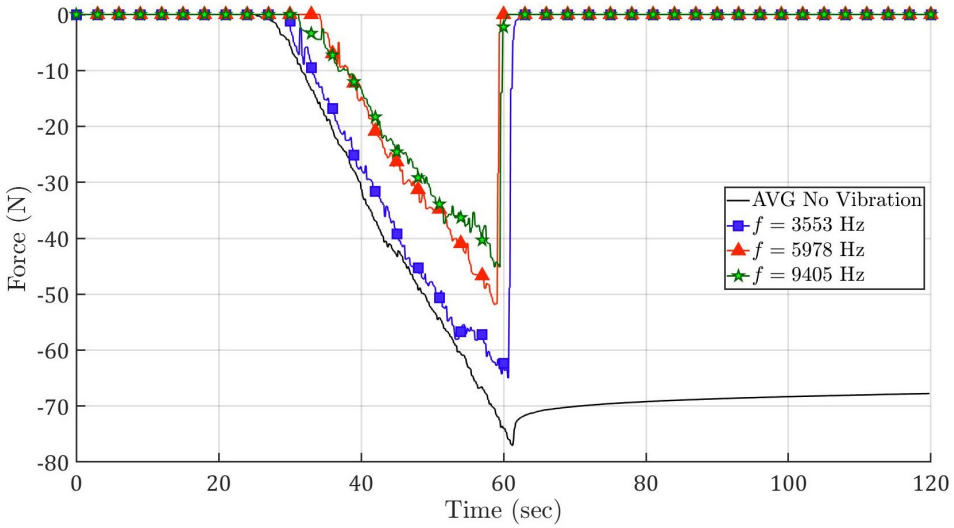

(B) Whirling probe motion

FIGURE 5.16: Penetration force with bi-directional modes of vibration

Probe Motion	f_1 (Hz)	f_2 (Hz)	F_{max}^{a} (N)	R^{b}(%)	$t_r{}^{c}$(sec)
No Vibration	0	0	77	–	–
Whirling	3553	3553	65	15%	1.5
Whirling	5978	5978	52	32%	0.7
Whirling	9405	9405	45	42%	1.0
Chaotic	3553	5978	51	33%	0.8
Chaotic	9405	5978	50	35%	0.8
Chaotic	3553	9405	45	42%	2.0

[a] Maximum Penetration Force in Newton
[b] Percentage of Maximum Force Reduction
[c] Release Time in seconds

TABLE 5.4: Penetration forces in bi-directional excitation

5.4 Conclusions

We developed a vibro probe to investigate how bending vibrations impact the penetration force into granular materials. This probe exploits bending resonance modes instead of the usual longitudinal vibrations and introduces a new method to improve penetration into granular materials. The probe was equipped with four piezo-electric patches to generate bending vibrations, and we identified its resonance modes through modal analysis. Subsequently, we performed preliminary penetration tests to identify the most effective bending vibration resonance modes for soil fluidization. Then, we conducted main penetration tests to observe the impact of the identified efficient vibration resonances on penetration force. The key findings are as follows:

- **Initial Penetration Tests:**

  It was noted that for the efficient transfer of vibration energy to soil particles and facilitation of penetration, both displacement and acceleration of vibration of the probe tip are crucial. Resonance frequencies below 3000 Hz and above 10000 Hz were found to be ineffective due to low acceleration and displacement vibration amplitudes, respectively. In contrast, resonance modes within the 3000-10000 Hz range exhibited effectiveness, as these frequencies fall within a range where both acceleration and displacement vibration amplitudes are comparatively high compared to the entire frequency spectrum.

- **Main Penetration Tests (Unidirectional Bending Vibrations):**

  In the main penetration tests involving unidirectional bending vibrations, frequencies of 5978 Hz and 9405 Hz led to significant reductions in the maximum penetration force by 28% and 21%, respectively. Furthermore, at the end of the penetration

process, penetration forces reached zero within 1.4 sec and 4.4 sec for the resonance modes of 5978 Hz and 9405 Hz, respectively. During this release period, the deflected shape of the frame returned to its original state by pushing the probe slightly into the fluidized soil sample, and the force in the force sensor reached zero. This indicated that the combined weight of the probe and the linear actuator was sufficient for the slight penetration and instant release of stresses in the structure in the presence of the bending vibrations. Conversely, for the non-vibrating probe, the force sensor only exhibited a 12% reduction in peak force over approximately 59 sec. This happened because the deflected structure pushed the probe into the soil to release stresses. However, without bending vibrations, this force was not enough to penetrate the probe slightly into the soil and instantly release stresses in the structure. At a frequency of 3553 Hz, the reduction in the maximum penetration force was less pronounced, but the release time was 2.3 sec.

- **Main Penetration Tests (Bidirectional Bending Excitation):** Bidirectional bending vibrations led to chaotic vibrations when the frequencies differed or whirling motion when they were at the same frequency with a 90-degree phase difference. Significantly, bidirectional excitation demonstrated superior improvements in reducing penetration force compared to unidirectional excitation, as the vibration fluidized the soil in two perpendicular directions. For example, employing a whirling motion with a vibration mode at 9405 Hz in two directions with a 90-degree phase difference resulted in a 42% decrease in the maximum penetration force compared to a non-vibrating probe, and the release time was reduced to 1 second. In terms of release time, the whirling motion at a frequency of 5978 Hz exhibited the fastest duration of 0.7 seconds, with a 32% reduction in the maximum penetration force.

In summary, our results highlight the potential of unidirectional and bidirectional bending vibrations to reduce the required penetration force and, therefore, can offer a promising solution in the reduction of the size of soil drilling equipment for remote areas. To meet this objective, future research needs to investigate the effects of bending vibrations across diverse soil types, particle sizes, and more challenging subsurface conditions, including those with heterogeneous regolith and higher relative density or rocky substrates. This exploration should aim to assess and improve the applicability of bending vibrations and design more advanced tools that harness these vibrations to assist in soil drilling across various environments.

Chapter 6

Conclusions, Future Directions, and Practical Applications

6.1 Conclusions

For extraterrestrial soil subsurface investigation, this research provides an analytical tool for designing a compact subsonic projectile probe and also experimentally proves an innovative solution to access deeper soil layers in space with lighter rigs. The study is structured around three key objectives defined in Chapter 1, and here are the insights from each step to meet these objectives:

- **Analytical Tools for High-Speed Probe Design (Objective 1):**

  Firstly, the subsonic projectile probe, based on a validated analytical model, offers a reliable means of predicting penetration depth and stresses on compact probes under perpendicular subsonic impact. Non-linear cavity expansion approximations have been developed using the Mohr-Coulomb failure criterion to simulate rigid projectile penetration into geological targets. Two models were used: the locked hydrostat and linear pressure-volumetric strain assumptions. The locked hydrostat model, modified in this study, accounts for situations where cavity pressure is insufficient to completely compact material near the cavity wall. The linear volumetric strain model estimates higher stresses on the projectile, especially in porous materials. Therefore, it is most effective for providing a lower bound for penetration depth in dense soils and regolith. In contrast, the locked hydrostat model, including the modified version presented in this study, estimates relatively lower stresses at the cavity wall and can more accurately predict the final penetration depth. Therefore, these models are valuable tools for designing and evaluating subsonic portable probe penetration and can serve as benchmarks for more complex methods. The locked hydrostat model predicts penetration depth more accurately, providing a more precise estimation of stress levels on the projectile probe, which is useful for probe structure design. In contrast, the linear pressure-volumetric strain model predicts lower penetration

depth and higher stress bounds, making it suitable for more conservative probe designs.

High-Frequency Vibro-Probes for Enhanced Penetration (Objective 2):

Secondly, the introduction of high-frequency bending vibrations through vibro probes presents a promising strategy to enhance penetration in granular media. Discrete Element Method (DEM) simulations have been used to analyze the effects of probe lateral vibrations on reducing regolith resistance forces. The simulations show that increasing the vibration amplitude or frequency reduces the required penetration force, although the rate of reduction decreases with higher frequencies. Vibration is more effective at lower penetration rates, where the kinetic energy of the probe's vertical motion is much lower than that of the vibration. The nose geometry of the probe significantly influences the penetration rate achievable at a constant overhead weight.

- **Experimental Validation of Bending Vibration-Enhanced Penetration (Objective 3):**

  Finally, the experimental investigation confirms that the implementation of bending vibrations significantly enhances the penetration capabilities of probes in granular materials. We developed two vibro probes to examine the effects of bending vibrations on penetration force in granular materials. One probe had a hex cross-section and was equipped with two piezoelectric patches to generate bending vibrations in a single direction. The other probe had a circular cross-section and was equipped with four piezoelectric patches to generate bending vibrations in two perpendicular directions. We identified their resonance modes through modal tests and analysis. Subsequently, we conducted preliminary penetration tests to determine the most effective bending vibration resonance modes for soil fluidization. Following this, we performed main penetration tests to observe the impact of these optimal vibration resonances on the penetration force for each probe. The main findings are summarized below:

  - **Initial Penetration Tests:**

    Our preliminary penetration tests for both the hex and circular probes confirmed the importance of both vibration displacement and acceleration amplitude for efficient energy transfer to soil particles and enhanced penetration. For the hex probe, effective resonance modes for sand fluidization were identified within the 3.5-11 kHz frequency range, exhibiting significantly higher displacement and acceleration levels. Below 3.5 kHz, resonance bending modes had limited impact on soil resistance, while above 11 kHz, the reduction in penetration force was minimal. Similarly, for the circular probe, resonance frequencies below 3000 Hz and above 10000 Hz were ineffective due to low acceleration

and displacement amplitudes, respectively. Resonance modes within the 3000-10000 Hz range were effective, as these frequencies had comparatively high acceleration and displacement amplitudes across the frequency spectrum.

– **Main Penetration Tests (Unidirectional Bending Vibrations):**
For the hex probe, the 6731 Hz mode had the most significant effect, reducing the maximum penetration force from 94.1 N to 68.6 N, outperforming the 3937 Hz and 9823 Hz modes. Additionally, after the probe stopped penetrating, all three modes (3937 Hz, 6731 Hz, and 9823 Hz) enabled a rapid drop in penetration force within 2.0, 1.2, and 1.6 seconds, respectively. This indicated that the combined weight of the probe and the linear actuator was sufficient for slight penetration and instant stress release in the structure when efficient bending vibration resonances were present. In contrast, for the non-vibrating probe, the force sensor showed a very gradual reduction in force because the probe and linear actuator remained under compression between the soil sample and the lever mechanism attached to the force sensor when the linear actuator stopped.
Similarly, for the circular probe, in the main penetration tests involving unidirectional bending vibrations, frequencies of 5978 Hz and 9405 Hz led to significant reductions in the maximum penetration force by 28% and 21%, respectively. Furthermore, at the end of the penetration process, penetration forces reached zero within 1.4 seconds and 4.4 seconds for the resonance modes of 5978 Hz and 9405 Hz, respectively. During this release period, the deflected shape of the frame returned to its original state as the probe began to sink into the fluidized soil sample, and the force in the force sensor reached zero. Conversely, for the non-vibrating probe, the force sensor only exhibited a 12% reduction in peak force over approximately 59 seconds. At a frequency of 3553 Hz, the reduction in the maximum penetration force was less pronounced, but the release time was 2.3 seconds.
Comparing the two probes, the circular probe exhibits greater efficiency in penetration, requiring lower forces compared to the hex probe. Even in unidirectional excitations, the circular probe is more effective in minimizing the maximum penetration force. This can be attributed to its circular shape, which promotes more even stress distribution in the soil.

– **Main Penetration Tests (Bidirectional Bending Excitation):**
Bidirectional tests were conducted exclusively with the circular probe, which was equipped with two sets of piezoelectric patches to generate bidirectional vibration excitations. When the excitation frequencies differed, the bidirectional bending vibrations caused chaotic movements in the probe's structure and tip. When the frequencies matched with a 90-degree phase difference, a whirling motion occurred. Notably, bidirectional excitation showed significantly better performance in reducing penetration force compared to unidirectional excitation, as the vibrations fluidized the soil in two perpendicular directions. For instance,

using a whirling motion with a vibration mode at 9405 Hz in two directions with a 90-degree phase difference led to a 42% reduction in maximum penetration force compared to a non-vibrating probe, with the release time reduced to 1 second. Additionally, the whirling motion at 5978 Hz achieved the quickest release time of 0.7 seconds, reducing the maximum penetration force by 32%.

In summary, this study offers practical solutions for overcoming payload limitations in soil drilling in remote areas, with a focus on enhancing efficiency in subsurface exploration. The validated models and experimental evidence for the subsonic projectile probe and vibro probes offer viable options to tackle the unique challenges of soil drilling in remote and extraterrestrial environments. Therefore, the analytical solution becomes instrumental in designing a subsonic projectile probe capable of penetrating deeper into the sublayers of soil in space. After the initial penetration by impact, bending vibrations can facilitate further penetrations. Alternatively, we can disregard the projectile probe, and a robotic probe designed to land on the surface can exploit bending vibrations for smoother penetrations.

6.2 Future Directions

To advance the technology readiness level (TRL) of our drilling techniques and tools, comprehensive testing and research in various aspects are essential. These include testing in analogs for harsh lunar environments, improving regolith simulants, field testing on Earth, and integrating advanced sensing technologies. Each of these areas plays a critical role in ensuring the functionality, reliability, and efficiency of our drilling systems for future space missions.

6.2.1 Sensitivity Analysis and Validation of the Analytical Model

Future work should include sensitivity analyses to better understand the influence of key parameters on model predictions, as discussed in Chapter 2. Since soil properties such as density, stiffness, Young's modulus, friction angle, and cohesion are interrelated through the relative density of the target material, the model should be tested across a range of relative densities for various soil types. This is especially important when applying the model to different geomaterials, including lunar regolith simulants. In addition, the effect of sliding friction at the probe–soil interface must be considered, as it can significantly influence resistance forces during penetration. Measuring acceleration throughout the penetration process remains critical for validating the model's predictions and identifying key dynamic phases of probe motion. It also helps determine which assumptions within the model are most appropriate for predicting probe velocity in each phase and can guide future improvements to the model.

6.2.2 Systematic Experimental Planning and Calibration Approaches

To better understand the influence of individual variables in Chapter 3, a more structured approach to planning experiments and simulations is recommended. This would help

separate the effects of each parameter and provide a clearer picture of their roles in soil–probe interactions. As highlighted in the literature, simplified physical tests—such as angle of repose and hopper discharge—are commonly used to calibrate DEM models due to their simplicity and effectiveness in capturing bulk behavior (Coetzee, 2017; Markauskas and Kačianauskas, 2011). Combining these tests helps reduce the chances of non-unique calibration results, where different parameter sets produce similar outcomes (Li, Feng, and Zou, 2013; Combarros, Feise, Zetzener, and Kwade, 2014).

Using multiple calibration methods—such as ring shear cell tests (Simons, Weiler, Strege, Bensmann, Schilling, and Kwade, 2015) and soil–tool interaction tests (Asaf, Rubinstein, and Shmulevich, 2007)—can further narrow down the parameter ranges and increase model accuracy. These methods allow for evaluation of critical parameters such as particle-particle and particle-wall friction, rolling resistance, and particle stiffness. In addition, modern DEM software like the EDEM Calibration Kit provides built-in calibration tools and standardized test setups to streamline this process (Altair Engineering, 2020).

To simulate the bending resonance mode of the probe, incorporating FEM is essential. However, this approach can become highly complex and computationally expensive due to the need to model both high-frequency vibrations and long-duration penetration processes. Despite these challenges, coupling FEM with DEM remains valuable—particularly when replicating lunar conditions, which are difficult to reproduce through physical experiments on Earth. This combined modeling strategy enables a more realistic representation of probe behavior and soil interaction, capturing dynamic effects that rigid body assumptions cannot account for.

6.2.3 Repeatability and Statistical Validation

As discussed in Chapter 4 and Chapter 5, consistent penetration resistance trends were observed in our experiments, largely due to the proper soil sample preparation methods outlined in those sections. This approach resulted in a maximum deviation of only 4% in peak force for the circular probe. Additionally, two sets of penetration tests conducted with the same bending vibration modes in orthogonal directions showed close agreement in key parameters such as peak penetration force and the time required for the force to drop to zero, further confirming the repeatability of the method.

Although the results are consistent under controlled laboratory conditions, future tests should include additional repetitions—particularly when larger soil samples are required or when tests are conducted under less controlled field conditions—to strengthen the conclusions. Furthermore, current comparisons are primarily based on two parameters: peak penetration resistance and the time required for the force to drop to zero. Future studies should similarly focus on multiple parameters, such as overall penetration force reduction and the time required to reach a certain depth under a given load, and include repeated tests to ensure reliability and account for variability.

6.2.4 Moon Environment Simulation Tests

It is essential to perform extensive testing under a variety of conditions to advance the TRL of our drilling techniques and tools. This includes vacuum testing to simulate the absence of atmosphere found on the Moon and other celestial bodies, as well as high and low-temperature testing to ensure the tools can withstand the extreme temperature fluctuations experienced on the Moon. Additionally, low gravity testing is necessary to replicate the Moon's lower gravitational field and assess the tool's performance in reduced gravity. These tests are critical for identifying and addressing potential issues that could arise during actual missions, such as tool malfunctions, and performance degradation. Conducting these tests ensures that our drilling techniques and tools are robust and reliable for lunar exploration.

6.2.5 Enhanced Regolith Simulants

In our penetration tests on fine-cutting limestone, we used sub-angular granular materials to mimic the jagged and irregular features of lunar regolith. This choice aimed to create a more accurate simulant of the lunar surface. However, it is necessary to investigate further the specific challenges posed by the angular nature of lunar regolith particles. These particles have sharp edges and irregular shapes, which can lead to interlocking arrangements, increasing bonding and internal friction within the lunar soil. This enhanced bonding can affect the performance of drilling or penetration tools. Understanding these properties and challenges is vital for developing tools that can effectively interact with the unique characteristics of the lunar surface. Therefore, future research should focus on using more precise lunar regolith simulants to avoid unforeseen issues similar to those encountered by the Mole during the Insight mission.

6.2.6 Field Testing on Earth

Conducting field tests in Earth environments that simulate extraterrestrial conditions can provide valuable insights into tool performance and reliability. These tests are not only crucial for space missions but also for improving Earth soil drilling applications. Field testing helps evaluate and improve the effects of bending vibrations across various soil types, particle sizes, and challenging geological conditions, including heterogeneous regolith and rocky substrates. Understanding these factors is essential for assessing the feasibility of bending vibrations and for designing advanced tools capable of navigating diverse soils and subsurface environments both on Earth and in other remote and challenging settings.

6.2.7 Auger Drilling Techniques

The current study primarily concentrated on utilizing bending vibrations for vibration-assisted penetrations, where the probe is pushed into the surface. However, rotation also plays a crucial role in penetrating soil layers, especially in challenging terrains, and is influential in bringing soil to the surface through the auger flute design. Therefore, for

future work, the next stage is to investigate the effects of bending vibrations on reducing the required torque and force for the augered soil drilling technique. Understanding how bending vibrations can complement rotational movements will be key in optimizing the efficiency and effectiveness of auger-based drilling systems.

6.2.8 Integration of Advanced Robotics and Sensing Technologies

After exploring the impacts of rotations, it is crucial to integrate linear and rotational drilling techniques into a compact rig, as illustrated in Figure 6.1. This figure depicts a supporting structure housing linear actuators, power supply, amplifiers, and the drilling rig. The supporting structure can either be a stationary platform deployed by a rover or a mobile rover itself, containing all necessary components. We can design our drilling tool similar to the Inchworm Boring Robot (IBR) and Inchworm drill (ID) developed by Dewei, Weiwei, Shengyuan, Yi, and Huazhi (2015) and Zhang, Li, Jiang, Ji, and Deng (2019). This design involves two augers—one right-hand and one left-hand—connected by two centrally located gear motors. These motors rotate the augers in opposite directions, allowing the probe to either penetrate or retract from the soil. Piezoelectric patches must be designed for attachment inside the auger walls to generate bending resonance vibrations that fluidize the soil and assist in the penetration process. At the penetration's outset, the linear actuator within the supporting structure initiates the probe's descent into the soil regolith (Figure 6.1a). As the first auger is sufficiently buried beneath the surface (Figure 6.1b), its corresponding gear motor activates to rotate the auger to facilitate further penetration. Similarly, once the second auger is sufficiently penetrated, its gear motor initiates rotation in the direction opposite to the first auger to further assist in the penetration process. Once the drilling auger is fully extended beyond the supporting structure, it detaches from the linear actuator, and the drilling continues using only the inchworm-inspired mechanism described in Figure 1.2 in Chapter 1. The system is tethered to the supporting structure by a flexible cable, which not only facilitates the retraction of the probe from the soil and supplies power to the gear motors and piezoelectric patches (Figure 6.1c) but also transmits commands and returns data from the probe. Additionally, this cable can include a thermal measurement function, similar to that in the HP^3 instrument (Spohn, Hudson, Marteau, Golombek, Grott, Wippermann, Ali, Schmelzbach, Kedar, Hurst, et al., 2022), which embeds multiple temperature sensors at specific intervals along its length. This setup allows for precise temperature monitoring at various depths and facilitates the determination of the thermal properties of the regolith.

Moreover, The drilling rig can be equipped with advanced sensing technologies such as ultrasonic/sonic testing and fiber optic sensors for comprehensive soil analysis. First, ultrasonic receivers are securely placed on the surface near the probe borehole. Also, it can be securely mounted in a borehole at specific intervals (Figure 6.2). Vibrations generated by the probe in bending resonance modes are powerful enough to act as the source for the ultrasonic/sonic transmitter. An accelerometer positioned inside the probe's tip is beneficial for recording acceleration and developing a precise transfer function that relates the applied voltage to the probe tip's acceleration within the regolith. This

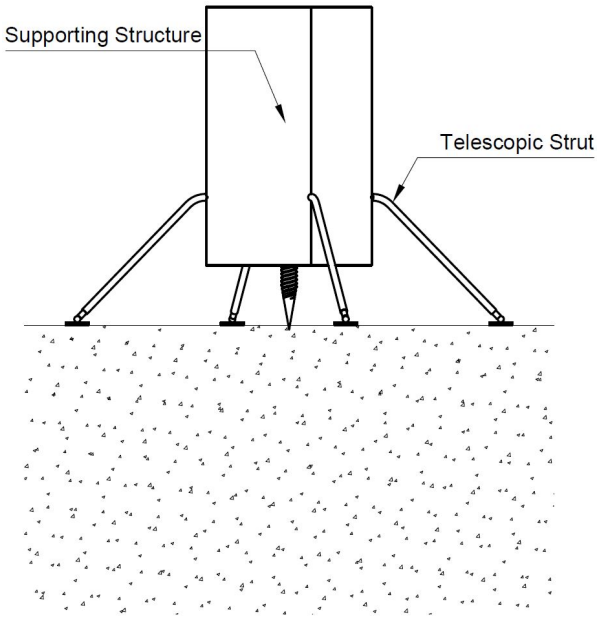

(A) Initial penetration by linear actuator.

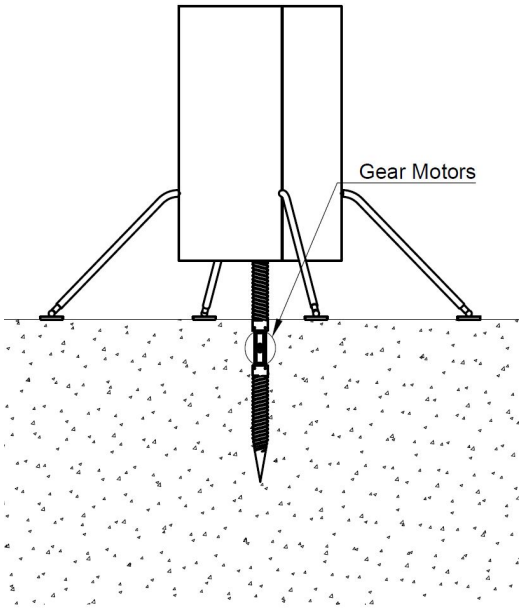

(B) First auger activation assisting penetration.

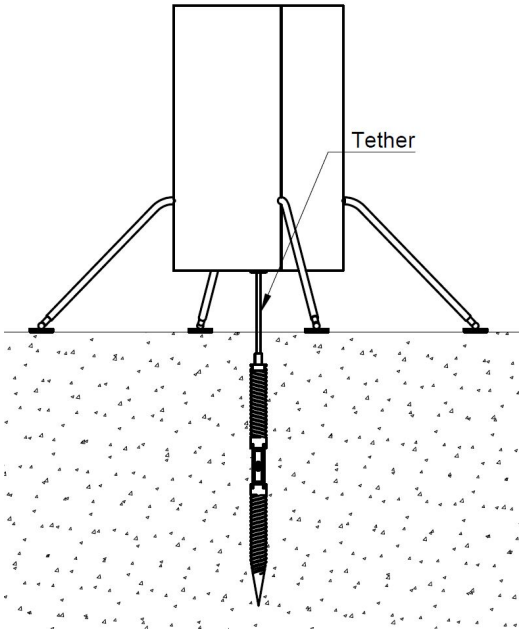

(C) Dual auger rotations for deeper penetration.

FIGURE 6.1: Phases of Soil Penetration Enhanced by Bending Resonance Vibrations

setup allows for the real-time measurement of soil properties by analyzing the velocity and attenuation of the waves using an advanced signal interpretation method such as an inverse multiphase poromechanical approach (Liu, Maghoul, Shalaby, and Thomson, 2023). These technologies can provide critical insights into the regolith's density, porosity, and mechanical properties, enhancing the information gathered from thermal measurements via the tether cable. Alternatively, fiber optic sensors can be installed in trenches or, ideally, within a borehole adjacent to the probe (Figure 6.2). These sensors are highly sensitive, immune to electromagnetic interference, and effective over long distances and in harsh conditions (Ma, Pei, Zhu, Shi, and Yin, 2023). Placing fiber optic sensors inside a borehole is particularly advantageous as it allows for continuous soil temperature, seismic monitoring, and the assessment of regolith behavior under seismic stress. Additionally, incorporating Fiber Optic Raman Spectroscopy, connected through the tether cable extending from the supporting structure to the probe, further enhances this system. This spectroscopy technique enables the detection of chemical compositions within the regolith, providing vital data on its molecular structure and complementing the physical and mechanical analyses previously conducted. Furthermore, when only the upper auger is operational, we can activate the CPT test at the cone of the probe at the lower auger for detailed soil resistance profiling, enabling precise assessment of soil stratigraphy and stiffness, which is critical for understanding soil bearing capacity and structural integrity.

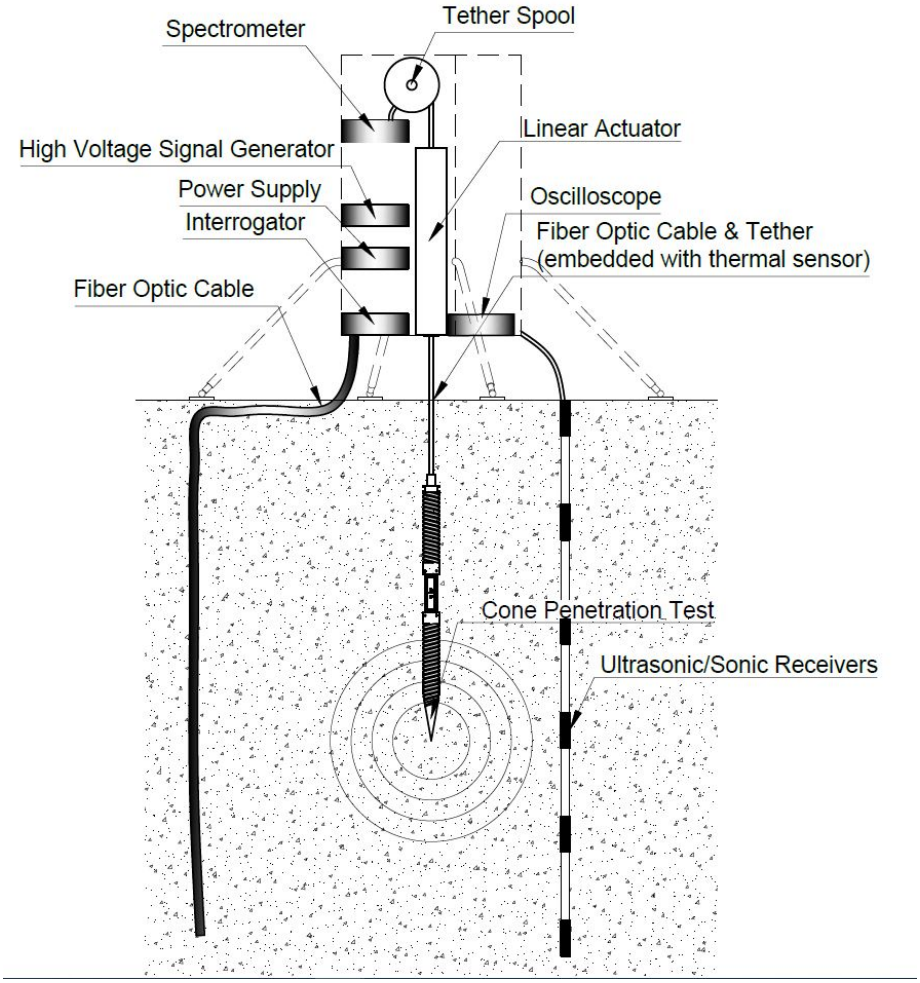

FIGURE 6.2: Illustration of the drilling rig's instrumentation.

6.3 Practical Applications

Soil drilling finds applications in diverse environments, each presenting unique challenges that demand more portable and adaptable drilling solutions. Whether it's exploring the lunar subsurface and beyond or conducting subsurface investigations on Earth, the need for compact and maneuverable drilling rigs becomes crucial. Here are two distinct scenarios showcasing the diverse requirements for more portable soil drilling:

- **Soil Drilling in Space:**

  Despite it being nearly 50 years since the last human landing on another planet (Apollo 17 in 1972), there is a renewed interest in lunar exploration. Various space agencies and private companies are gearing up for lunar exploration activities. NASA's Artemis program, for instance, aims to establish sustainable lunar exploration by 2028, involving the creation of a human base camp, the development of technologies for In-Situ Resource Utilization (ISRU), and addressing challenges such as energy, water, oxygen, and material resources harvesting (Royal Museums Greenwich). The overarching objective is to pave the way for crewed trips to Mars in the

2030s. ISRU technologies are crucial for extracting and processing local materials into fuel, water, metals, and oxygen, thereby reducing dependence on Earth-based resources.

Understanding the mechanical behavior and mineralogy of the lunar regolith is crucial for designing structures for human settlement on the Moon and beyond. Our innovative vibro soil drilling technology plays a pivotal role in shrinking the size of drilling rigs for space applications, allowing the creation of more portable soil rigs capable of accessing the Moon's sublayers and beyond. The Moon and Mars have been focal points for mining and subsurface investigation missions, experiencing a renewed interest due to their potential to support human settlements and future space missions.

- **Soil Drilling on Earth:**

  Soil drilling rigs are vital for subsurface investigations, but their size can present significant challenges for various applications, especially in remote or inaccessible areas like mountainous regions or jungles. Disassembling the rig into smaller parts and transporting them by helicopter is one potential solution, but this approach can be both time-consuming and costly. Additionally, the large size of the equipment can make it challenging to find suitable and stable ground to install it. In some cases, significant excavation and leveling may be necessary to create a stable base for the drilling rig. As the drilling rig's size increases, so does the difficulty of preparing a suitable bed, which can add significant time and cost to the overall drilling project. Therefore, it is crucial to carefully assess the terrain and ground conditions before selecting the drilling equipment and preparing the bed for installation to ensure efficient and safe drilling operations.

  In addition, employing large and heavy drilling equipment in confined spaces with restricted access, such as dams, power plants, or existing structures, can give rise to safety issues and potential harm to the structure. The structure of the dam may be delicate and vulnerable to harm from heavy equipment or drilling operations. Consequently, specialized drilling tools and techniques are imperative to ensure the safety of workers and prevent structural damage. Additionally, the size of the structure may restrict the movement of soil drilling rigs into the building, necessitating specific arrangements such as disassembling the rig or using a smaller rig that can fit through narrow spaces.

  Soil drilling becomes essential during the installation of vertical geothermal heat exchangers. Geothermal systems offer practical heating and cooling solutions for properties, with vertical closed-loop configurations being the most efficient. These systems are advantageous because they don't rely on nearby water sources and cause minimal damage to yards. However, the high cost and challenges associated with borehole drilling have led to the popularity of alternative methods such as electrical, wind, or solar solutions. One significant concern with soil drilling equipment is the potential mess it can create in residential yards. It is crucial for the drilling rig to be

compact enough to fit into limited spaces in residential areas. Additionally, noise and vibrations during the drilling process can cause discomfort for residents. Therefore, smaller and more maneuverable drilling rigs are preferred in residential areas to navigate tight spaces and minimize disruptions to driveways and yards.

In summary, the challenges of heavy big soil drilling rigs are numerous and varied, including transportation, access to limited spaces, safety hazards, and disruptions to residential communities. Therefore, the use of more maneuverable rigs for geotechnical construction services reduces costs and facilitates subsurface tests in remote areas with limited accessibility and narrow spaces for heavy equipment to operate. Moreover, further reductions in the size of drilling tools with our vibro solid drilling technique would be beneficial to prevent any damage and even deploy small drilling rigs inside buildings, such as basements, near other pieces of equipment of a geothermal heat exchanger.

Bibliography

Alaei Varnosfaderani, Mahdi, Maghoul, Pooneh, and Wu, Nan (Aug. 2021). *PESCE: Penetration Estimation of subsonic rigid projectile probes into granular materials using the Spherical Cavity Expansion theory*. DOI: 10.5281/zenodo.5202859. URL: https://doi.org/10.5281/zenodo.5202859.

Alaei Varnosfaderani, Mahdi, Maghoul, Pooneh, and Wu, Nan (2022). "Penetration Analysis of High-Frequency Vibro-Based Probes in Granular Media Using the Discrete Element Method". In: *Earth and Space 2022*, pp. 176–183.

Alkalla, Mohamed, Pang, Xavier, Pitcher, Craig, and Gao, Yang (2021). "DROD: A hybrid biomimetic undulatory and reciprocatory drill: Quantitative analysis and numerical study". In: *Acta Astronautica*.

Alkalla, Mohamed G, Gao, Yang, and Bouton, Arthur (2019). "Customizable and Optimized Drill Bits Bio–inspired from Wood–Wasp Ovipositor Morphology for Extraterrestrial Surfaces". In: *2019 IEEE/ASME International Conference on Advanced Intelligent Mechatronics (AIM)*. IEEE, pp. 430–435.

Allen, William A, Mayfield, Earle B, and Morrison, Harvey L (1957). "Dynamics of a projectile penetrating sand. Part II". In: *Journal of Applied Physics* 28.11, pp. 1331–1335.

Altair Engineering (2020). *Faster calibration with the Altair EDEM Calibration Kit - Blog*. URL: https://blog.s-t.com.tr/2020/07/03/altair-edem-calibration-kit-ile-daha-hizli-kalibrasyon/ (visited on 04/12/2021).

Altieri, Francesca, Frigeri, Alessandro, Lavagna, Michèle, Le Gall, Alice, Nikiforov, Sergey Yuryevich, Stoker, Carol, Ciarletti, Valérie, De Sanctis, Maria Cristina, Josset, Jean-Luc, Mitrofanov, Igor, et al. (2023). "Investigating the Oxia Planum subsurface with the ExoMars rover and drill". In: *Advances in Space Research* 71.11, pp. 4895–4903.

Anwer Khan, M (2015). "Mechanics of projectile penetration into non-cohesive soil targets". In: *International Journal of Civil Engineering* 13.1, pp. 28–39.

APC International, Ltd (2021). *Physical and piezoelectric properties of APC materials*. URL: https://www.americanpiezo.com/apc-materials/physical-piezoelectric-properties.html (visited on 12/30/2022).

Asaf, Z, Rubinstein, D, and Shmulevich, I (2007). "Determination of discrete element model parameters required for soil tillage". In: *Soil and Tillage Research* 92.1-2, pp. 227–242.

Badescu, Mircea, Bar-Cohen, Yoseph, Sherrit, Stewart, Bao, Xiaoqi, Chang, Zensheu, Donnelly, Chris, and Aldrich, Jack (2012). "Percussive augmenter of rotary drills (PARoD)". In: *Sensors and Smart Structures Technologies for Civil, Mechanical, and Aerospace Systems 2012*. Vol. 8345. International Society for Optics and Photonics, 83450J.

Bai, Deen, Li, Yuntao, Quan, Qiquan, Tang, Dewei, and Deng, Zongquan (2023). "Development of a rotary-percussive ultrasonic drill using a bolt-clamped type piezoelectric actuator". In: *Advances in Space Research* 71.12, pp. 5360–5368.

Bao, Xiaoqi, Bar-Cohen, Yoseph, Chang, Zensheu, Dolgin, Benjamin P, Sherrit, Stewart, Pal, Dharmendra S, Du, Shu, and Peterson, Thomas (2003). "Modeling and computer simulation of ultrasonic/sonic driller/corer (USDC)". In: *IEEE transactions on ultrasonics, ferroelectrics, and frequency control* 50.9, pp. 1147–1160.

Bar-Cohen, Yoseph, Badescu, Mircea, Bao, Xiaoqi, Sherrit, Stewart, Zacny, Kris, Sadick, Shazad, and Ji, Jerri (2010). "Deep drilling and sampling via compact low-mass rotary-hammer auto-gopher". In: *Earth and Space 2010: Engineering, Science, Construction, and Operations in Challenging Environments*, pp. 1021–1030.

Bar-Cohen, Yoseph, Sherrit, Stewart, Dolgin, Benjamin P, Bridges, Nathan, Bao, Xiaoqi, Chang, Zensheu, Yen, Albert, Saunders, Ronald S, Pal, Dharmendra, Kroh, Jason, et al. (2001). "Ultrasonic/sonic driller/corer (USDC) as a sampler for planetary exploration". In: *2001 IEEE Aerospace Conference Proceedings (Cat. No. 01TH8542)*. Vol. 1. IEEE, pp. 1–263.

Basilevsky, AT, Ivanov, BA, Ivanov, AV, and Head, JW (2013). "Clarification of sources of material returned by Luna 24 spacecraft based on analysis of new images of the landing site taken by lunar reconnaissance orbiter". In: *Geochemistry International* 51, pp. 456–472.

Baumgartner, Werner, Fidler, Florian, Weth, Agnes, Habbecke, Martin, Jakob, Peter, Butenweg, Christoph, and Böhme, Wolfgang (2008). "Investigating the locomotion of the sandfish in desert sand using NMR-imaging". In: *PloS one* 3.10, e3309.

Benaroya, Haym (2017). "Lunar habitats: A brief overview of issues and concepts". In: *REACH* 7, pp. 14–33.

Bishop, RF, Hill, Rodney, and Mott, NF (1945). "The theory of indentation and hardness tests". In: *Proceedings of the Physical Society (1926-1948)* 57.3, p. 147.

Bolton, Malcolm D, Gui, Meen-Wah, Garnier, J, Corte, Jean François, Bagge, Gunnar, Laue, Jan, and Renzi, R (1999). "Centrifuge cone penetration tests in sand". In: *Géotechnique* 49.4, pp. 543–552.

Bonitz, Robert G, Shiraishi, Lori, Robinson, Matthew, Arvidson, Raymond E, Chu, PC, Wilson, JJ, Davis, KR, Paulsen, G, Kusack, AG, Archer, Doug, et al. (2008). "NASA Mars 2007 Phoenix lander robotic arm and icy soil acquisition device". In: *Journal of Geophysical Research: Planets* 113.E3.

Bower, Allan F (2009). *Applied mechanics of solids*. CRC press.

Cantwell, Brian (2014). *Equations of motion in cylindrical and spherical coordinates*. `https://web.stanford.edu/~cantwell/AA200_Course_Material/AA200_Course_Notes/AA200_Appendix_1_Eqns_in_cyl_sph_coords_Cantwell.pdf`.

Cardoni, Andrea, Harkness, Patrick, and Lucas, Margaret (2010). "Ultrasonic rock sampling using longitudinal-torsional vibrations". In: *Physics Procedia* 3.1, pp. 125–134.

Carrier III, W David (1974). "Apollo drill core depth relationships". In: *The moon* 10.2, pp. 183–194.

Chen, SL and Abousleiman, YN (2012). "Exact undrained elasto-plastic solution for cylindrical cavity expansion in modified Cam Clay soil". In: *Géotechnique* 62.5, pp. 447–456.

Chen, SL and Abousleiman, YN (2013). "Exact drained solution for cylindrical cavity expansion in modified Cam Clay soil". In: *Géotechnique* 63.6, pp. 510–517.

Coetzee, CJ (2017). "Calibration of the discrete element method". In: *Powder Technology* 310, pp. 104–142.

Collins, AL, Addiss, JW, Walley, SM, Promratana, K, Bobaru, F, Proud, WG, and Williamson, DM (2011). "The effect of rod nose shape on the internal flow fields during the ballistic penetration of sand". In: *International Journal of Impact Engineering* 38.12, pp. 951–963.

Colwell, JE, Batiste, S, Horányi, M, Robertson, S, and Sture, Steve (2007). "Lunar surface: Dust dynamics and regolith mechanics". In: *Reviews of Geophysics* 45.2.

Combarros, M, Feise, HJ, Zetzener, H, and Kwade, A (2014). "Segregation of particulate solids: Experiments and DEM simulations". In: *Particuology* 12, pp. 25–32.

Cooper, William L and Breaux, Bradley A (2010). "Grain fracture in rapid particulate media deformation and a particulate media research roadmap from the PMEE workshops". In: *International journal of fracture* 162.1-2, pp. 137–150.

Curious Droid (2017). *Apollo, the Lunar Dust and NASA's Dirty Problem - YouTube*. `https://www.youtube.com/watch?v=EFqpgmZAZgo`. Accessed: 2020-10-29.

Dewei, Tang, Weiwei, Zhang, Shengyuan, Jiang, Yi, Shen, and Huazhi, Chen (2015). "Development of an Inchworm Boring Robot (IBR) for planetary subsurface exploration". In: *2015 IEEE International Conference on Robotics and Biomimetics (ROBIO)*. IEEE, pp. 2109–2114.

Dimitriadis, EK, Fuller, CR, and Rogers, CA (1991). "Piezoelectric actuators for distributed vibration excitation of thin plates". In.

Dosch, Jeffrey J, Inman, Daniel J, and Garcia, Ephrahim (1992). "A self-sensing piezoelectric actuator for collocated control". In: *Journal of Intelligent material systems and Structures* 3.1, pp. 166–185.

Dunn, Marcia (2021). *RIP: Mars digger bites the dust after 2 years on red planet*. URL: https://apnews.com/article/mars-digger-dead-nasa-07a241714b85f9633ce1c8baf084d16e (visited on 05/25/2021).

Ellery, Alex (2020). "Sustainable in-situ resource utilization on the moon". In: *Planetary and Space Science* 184, p. 104870. DOI: 10.1016/j.pss.2020.104870. URL: https://doi.org/10.1016/j.pss.2020.104870.

European Space Agency (2021). *First deep drilling success for ExoMars*. URL: https://www.esa.int/Science_Exploration/Human_and_Robotic_Exploration/Exploration/ExoMars/First_deep_drilling_success_for_ExoMars.

Ferrari, M, De Angelis, S, De Sanctis, MC, Frigeri, A, Altieri, F, Ammannito, E, Formisano, M, and Vinogradoff, V (2023). "Constraining the Rosalind Franklin Rover/Ma_MISS Instrument Capability in the Detection of Organics". In: *Astrobiology* 23.6, pp. 691–704.

Firstbrook, David, Harkness, Patrick, and Gao, Yang (2014). "A novel study on high-powered ultrasonic penetrators in granular material". In: *AIAA SPACE 2014 Conference and Exposition*, p. 4265.

Firstbrook, David, Worrall, Kevin, Harkness, Patrick, Flessa, Thaleia, McGookin, Euan, and Thomson, Douglas (2018). "Ultrasonic Auger for Narrow-Gauge Borehole Drilling". In: *2018 IEEE International Ultrasonics Symposium (IUS)*. IEEE, pp. 1–4.

Firstbrook, David, Worrall, Kevin, Timoney, Ryan, and Harkness, Patrick (2018). "Ultrasonically Assisted Hammer-Action Penetrators in Planetary Regolith". In: *Earth and Space 2018: Engineering for Extreme Environments*. American Society of Civil Engineers Reston, VA, pp. 359–368.

Firstbrook, David, Worrall, Kevin, Timoney, Ryan, Suñol, Francesc, Gao, Yang, and Harkness, Patrick (2017). "An experimental study of ultrasonic vibration and the penetration of granular material". In: *Proceedings of the Royal Society A: Mathematical, Physical and Engineering Sciences* 473.2198, p. 20160673.

Forrestal, Michael J et al. (1986). "Penetration into dry porous rock". In: *International Journal of Solids and Structures* 22.12, pp. 1485–1500.

Forrestal, MJ and Luk, VK (1988). "Dynamic spherical cavity-expansion in a compressible elastic-plastic solid". In.

Forrestal, MJ and Luk, VK (1992). "Penetration into soil targets". In: *International Journal of Impact Engineering* 12.3, pp. 427–444.

Forrestal, MJ, Norwood, FR, and Longcope, DB (1981). "Penetration into targets described by locked hydrostats and shear strength". In: *International Journal of Solids and Structures* 17.9, pp. 915–924.

Forrestal, MJ and Tzou, DY (1997). "A spherical cavity-expansion penetration model for concrete targets". In: *International Journal of Solids and Structures* 34.31-32, pp. 4127–4146.

Foust, Jeff (October 27, 2019). *InSight heat flow probe suffers setback*. `https://spacenews.com/insight-heat-flow-probe-suffers-setback/`. accessed: 18.07.2020.

Gale, Manuel, Buettner, Kevin, Mehta, Ranjan, Liever, Peter A, and Curtis, Jennifer (2017). "Gas-granular flow solver for plume surface interaction and cratering simulations". In: *23rd AIAA Computational Fluid Dynamics Conference*, p. 4503.

Gao, Yang, Ellery, Alex, Jaddou, Mustafa, Vincent, Julian, and Eckersley, Steven (2007). "Planetary micro-penetrator concept study with biomimetric drill and sampler design". In: *IEEE Transactions on Aerospace and Electronic Systems* 43.3, pp. 875–885.

Gao, Yang, Phipps, Andy, Taylor, Mark, Crawford, Ian A, Ball, Andrew J, Wilson, Lionel, Parker, Dave, Sweeting, Martin, Silva Curiel, Alex da, Davies, Phil, et al. (2008). "Lunar science with affordable small spacecraft technologies: MoonLITE and Moonraker". In: *Planetary and Space Science* 56.3-4, pp. 368–377.

Goldman, Samuel, Flashner, Henryk, and Yang, Bingen (2022). "An Approach to Modeling Percussive Drilling Systems". In: *Journal of Vibration and Acoustics* 144.5, p. 051015.

Golombek, Matthew, Grott, Matthias, Kargl, Günter, Andrade, J, Marshall, J, Warner, N, Teanby, Nick A, Ansan, Véronique, Hauber, Ernst, Voigt, Joana, et al. (2018). "Geology and physical properties investigations by the InSight lander". In: *Space Science Reviews* 214.5, p. 84.

Gouache, T, Gao, Y, Frame, T, Coste, P, and Gourinat, Yves (2011). "Identification of the forces between regolith and a reciprocating drill-head: Perspectives for the exploration of Martian regolith". In: *Proceedings of the 62nd International Astronautical Congress*. IAC-11.

Gouache, Thibault P, Gao, Yang, Coste, Pierre, and Gourinat, Yves (2011). "First experimental investigation of dual-reciprocating drilling in planetary regoliths: Proposition of penetration mechanics". In: *Planetary and Space Science* 59.13, pp. 1529–1541.

Gromov, VV, Misckevich, AV, Yudkin, EN, Kochan, H, Coste, P, and Re, E (1997). "The mobile penetrometer, a" mole" for sub-surface soil investigation". In: *7th European Space Mechanisms and Tribology Symposium*. Vol. 410, p. 151.

Guzman, Ivan L, Iskander, Magued, Bless, Stephan, and Qi, Changguang (2014). "Terminal depth of penetration of spherical projectiles in transparent granular media". In: *Granular Matter* 16.6, pp. 829–842.

He, Tao, Wen, He-Ming, and Guo, Xiao-Jun (2011). "A spherical cavity expansion model for penetration of ogival-nosed projectiles into concrete targets with shear-dilatancy". In: *Acta Mechanica Sinica* 27.6, pp. 1001–1012.

Heiken, Grant H, Vaniman, David T, and French, Bevan M (1991). *Lunar Sourcebook, a user's guide to the Moon*.

Holtz, Robert D, Kovacs, William D, and Sheahan, Thomas C (1981). *An introduction to geotechnical engineering*. Vol. 733. Prentice-hall Englewood Cliffs, NJ.

Hopkins, HG (1960). "Dynamic expansion of spherical cavities in metals". In: *Progress in solid mechanics* 1.3, pp. 5–16.

Houston, WN, Mitchell, JK, and Carrier III, WD (1974). "Lunar soil density and porosity". In: *Lunar and Planetary Science Conference Proceedings*. Vol. 5, pp. 2361–2364.

Isaka, Keita, Tsumura, Kazuki, Watanabe, Tomoki, Toyama, Wataru, Sugesawa, Makoto, Yamada, Yasuyuki, Yoshida, Hiroshi, and Nakamura, Taro (2019). "Development of underwater drilling robot based on earthworm locomotion". In: *Ieee Access* 7, pp. 103127–103141.

Jung, Joe, Longcope, Donald B, and Tabbara, Mazen R (1999). *Modeling of Oblique Penetration into Geologic Targets Using Cavity Expansion Penetrator Loading with Target free-Surface Effects*. Tech. rep. Sandia National Laboratories (SNL), Albuquerque, NM, and Livermore, CA.

Khosravi, A, Martinez, A, DeJong, JT, and Wilson, D (2018). "Discrete element simulations of bio-inspired self-burrowing probes in sands of varying density". In: *Proceedings of the Biomediated and Bioinspired Geotechnical (B2G) Conference, Atlanta, GA*, pp. 12–13.

Klosky, J Ledlie, Sture, Stein, Ko, Hon-Yim, and Barnes, Frank (2000). "Geotechnical behavior of JSC-1 lunar soil simulant". In: *Journal of Aerospace Engineering* 13.4, pp. 133–138.

Kobrick, Ryan Lauren (2010). "Characterization and measurement standardization of lunar dust abrasion for spacecraft design and operations". PhD thesis. University of Colorado at Boulder.

Kotov, Vasiliy L, Linnik, Elena Yu, and Sabaeva, Tatiana A (2021). "Analyzing the Problem of a Spherical Cavity Expansion in a Medium with Mohr-Coulomb-Tresca's Plasticity Condition". In: *Dynamics, Strength of Materials and Durability in Multiscale Mechanics* 137, p. 67.

Labuz, Joseph F and Zang, Arno (2012). "Mohr–Coulomb failure criterion". In: *The ISRM Suggested Methods for Rock Characterization, Testing and Monitoring: 2007-2014*. Springer, pp. 227–231.

Li, Qiang, Feng, Mingxia, and Zou, Zongshu (2013). "Validation and calibration approach for discrete element simulation of burden charging in pre-reduction shaft furnace of COREX process". In: *ISIJ international* 53.8, pp. 1365–1371.

Li, Xuan and Harkness, Patrick (2023). "Rock drilling performance of rotary ultrasonic tools incorporating PZT piezoceramic and Mn: PIN-PMN-PT piezocrystal". In: *Sensors and Actuators A: Physical* 364, p. 114849.

Liu, Bangyuan, Ozkan-Aydin, Yasemin, Goldman, Daniel I, and Hammond, Frank L (2019). "Kirigami skin improves soft earthworm robot anchoring and locomotion under cohesive soil". In: *2019 2nd IEEE International Conference on Soft Robotics (RoboSoft)*. IEEE, pp. 828–833.

Liu, Hongwei, Maghoul, Pooneh, Shalaby, Ahmed, and Thomson, Douglas (2023). "Ultrasonic characterization of frozen soils using a multiphase poromechanical approach". In: *Computers and Geotechnics* 153, p. 105068.

Lo, Wei-Cheng, Yang, Chi-Chin, Hsu, Shao-Yiu, Chen, Chu-Hui, Yeh, Chao-Lung, and Hilpert, Markus (2017). "The dynamic response of the water retention curve in unsaturated soils during drainage to acoustic excitations". In: *Water Resources Research* 53.1, pp. 712–725.

Longcope, DB and Forrestal, MJ (1983). "Penetration of targets described by a Mohr-Coulomb failure criterion with a tension cutoff". In.

Longcope Jr, Donald B (1990). "The prediction of loads on penetrators into rock via the spherical cavity expansion approximation". In: *Sandia National Laboratories Report SAND87-0959*.

Luk, VK and Forrestal, MJ (1987). "Penetration into semi-infinite reinforced-concrete targets with spherical and ogival nose projectiles". In: *International Journal of Impact Engineering* 6.4, pp. 291–301.

Ma, Jiaxiao, Pei, Huafu, Zhu, Honghu, Shi, Bin, and Yin, Jianhua (2023). "A review of previous studies on the applications of fiber optic sensing technologies in geotechnical monitoring". In: *Rock Mechanics Bulletin* 2.1, p. 100021.

Macek, Richard W and Duffey, Thomas A (2000). "Finite cavity expansion method for near-surface effects and layering during earth penetration". In: *International journal of impact engineering* 24.3, pp. 239–258.

Maladen, Ryan D, Ding, Yang, Li, Chen, and Goldman, Daniel I (2009). "Undulatory swimming in sand: subsurface locomotion of the sandfish lizard". In: *science* 325.5938, pp. 314–318.

Markauskas, Darius and Kačianauskas, Rimantas (2011). "Investigation of rice grain flow by multi-sphere particle model with rolling resistance". In: *Granular Matter* 13.2, pp. 143–148.

Martinez, Alejandro, DeJong, Jason T, Jaeger, Robert A, and Khosravi, Ali (2020). "Evaluation of self-penetration potential of a bio-inspired site characterization probe by cavity expansion analysis". In: *Canadian Geotechnical Journal* 57.5, pp. 706–716.

Mizushina, Asuka, Omori, Hayato, Kitamoto, Hiroyuki, Nakamura, Taro, Osumi, Hisashi, and Kubota, Takashi (2013). "A discharging mechanism for a lunar subsurface explorer with the peristaltic crawling mechanism". In: *2013 6th International Conference on Recent Advances in Space Technologies (RAST)*. IEEE, pp. 955–960.

Mo, Pin-Qiang and Yu, Hai-Sui (2018). "Drained cavity expansion analysis with a unified state parameter model for clay and sand". In: *Canadian Geotechnical Journal* 55.7, pp. 1029–1040.

Mo, PQ and Yu, HS (2017). "Undrained cavity expansion analysis with a unified state parameter model for clay and sand". In: *Géotechnique* 67.6, pp. 503–515.

Munguira, A, Hueso, R, Sánchez-Lavega, A, Torre-Juarez, M de la, Martínez, GM, Newman, CE, Sebastian, E, Lepinette, A, Vicente-Retortillo, A, Chide, B, et al. (2023). "Near surface atmospheric temperatures at Jezero from Mars 2020 MEDA measurements". In: *Journal of Geophysical Research: Planets* 128.3, e2022JE007559.

Naclerio, Nicholas D, Karsai, Andras, Murray-Cooper, Mason, Ozkan-Aydin, Yasemin, Aydin, Enes, Goldman, Daniel I, and Hawkes, Elliot W (2021). "Controlling subterranean forces enables a fast, steerable, burrowing soft robot". In: *Science Robotics* 6.55, eabe2922.

Nakatake, Toyoharu, Konno, Masashi, Mizushina, Asuka, Yamada, Yasuyuki, Nakamura, Taro, and Kubota, Takashi (2016). "Soil circulating system for a lunar subsurface explorer robot using a peristaltic crawling mechanism". In: *2016 IEEE International Conference on Advanced Intelligent Mechatronics (AIM)*. IEEE, pp. 407–412.

NASA (2020). *NASA's lunar exploration program overview*. URL: `https://www.nasa.gov/wp-content/uploads/2020/12/artemis_plan-20200921.pdf`.

NASA (2023). *Lunar-A*. URL: `https://nssdc.gsfc.nasa.gov/nmc/spacecraft/display.action?id=LUNAR-A`.

Olaf, Krömer, Marco, Scharringhausen, Fittock, Mark, Georgios, Tsakyridis, Torben, Wippermann, Lars, Witte, Matthias, Grott, Jörg, Knollenberg, Tilman, Spohn, Christian,

Krause, et al. (2019). "Design details of the HP3 mole onboard the InSight mission". In: *Acta Astronautica* 164, pp. 152–167.

Omidvar, Mehdi, Bless, Stephan, and Iskander, Magued (2019). "Recent insights into penetration of sand and similar granular materials". In: *Shock Phenomena in Granular and Porous Materials*. Springer, pp. 137–163.

Omidvar, Mehdi, Iskander, Magued, and Bless, Stephan (2014). "Response of granular media to rapid penetration". In: *International Journal of Impact Engineering* 66, pp. 60–82.

Omidvar, Mehdi, Malioche, Jeanne Doreau, Bless, Stephan, and Iskander, Magued (2015). "Phenomenology of rapid projectile penetration into granular soils". In: *International Journal of Impact Engineering* 85, pp. 146–160.

Omori, Hayato, Murakami, Taro, Nagai, Hiroaki, Nakamura, Taro, and Kubota, Takashi (2012). "Development of a novel bio-inspired planetary subsurface explorer: Initial experimental study by prototype excavator with propulsion and excavation units". In: *IEEE/ASME Transactions on Mechatronics* 18.2, pp. 459–470.

Paul, Harrison, Balaban, Vojtech, Parker, Brent, Spray, John, Ellery, Alex, and Megill, William (2021). "MAPLE: A Versatile Penetrator Platform for Lunar Exploration". In: Canadian Lunar Workshop 2021. URL: `https://virtual.oxfordabstracts.com/#/event/2156/submission/24`.

Paulsen, Gale, Mank, Zachary, Wang, Alexander, Chow, Paul, Hyman, Cody, Thomas, Thomas, Lee, Allen, Zacny, Kris, Smith, James, Quinn, Jacqueline, et al. (2018). "The regolith and ice drill for exploration of new terrains (TRIDENT); a one-meter drill for the lunar resource prospector mission". In: *44th Aerospace Mechanisms Symposium*. NASA Kennedy Space Center Ohio Cleveland, p. 13.

Pitcher, Craig, Alkalla, Mohamed, Pang, Xavier, and Gao, Yang (2020). "Development of the Third Generation of the Dual-Reciprocating Drill". In: *Biomimetics* 5.3, p. 38.

Pitcher, Craig and Gao, Yang (2015). "Analysis of drill head designs for dual-reciprocating drilling technique in planetary regoliths". In: *Advances in Space Research* 56.8, pp. 1765–1776.

Pitcher, Craig and Gao, Yang (2017). "First implementation of burrowing motions in dual-reciprocating drilling using an integrated actuation mechanism". In: *Advances in Space Research* 59.5, pp. 1368–1380.

Prince, Jill L, Desai, Prasun N, Queen, Eric M, and Grover, Myron R (2011). "Mars phoenix entry, descent, and landing simulation design and modeling analysis". In: *Journal of Spacecraft and Rockets* 48.5, pp. 756–764.

Pritchard, Philip J and Mitchell, John W (2016). *Fox and McDonald's introduction to fluid mechanics*. John Wiley & Sons.

Quinn, JW, Captain, JE, Eichenbaum, AS, Aguilar-Ayala, R, Kleinhenz, JE, Zacny, KA, Chu, PC, and Vendiola, VR (2023). "Polar resources ice mining experiment-1 (PRIME-1) NASA's first polar drilling and volatiles detection mission". In: *Space Resources Roundtable XXIII Meeting*.

Rezich, Erin, Harrigan, Kerri, Thomas, Fransua, and Ludwiczak, Damian (2021). "Ultrasonically assisted Blade Technologies for lunar excavation". In: *Earth and Space 2021*, pp. 555–563.

Richter, L, Coste, P, Gromov, V, and Grzesik, A (2004). "The mole with sampling mechanism (MSM)–Technology development and payload of beagle 2 mars lander". In: *Proceedings, 8th ESA Workshop on Advanced Space Technologies for Robotics and Automation (ASTRA 2004), Noordwijk, The Netherlands, November*, pp. 2–4.

Richter, L, Coste, P, Gromov, VV, Kochan, H, Nadalini, R, Ng, TC, Pinna, S, Richter, H-E, and Yung, Kai Leung (2002). "Development and testing of subsurface sampling devices for the Beagle 2 lander". In: *Planetary and Space Science* 50.9, pp. 903–913.

Richter, L, Kochan, H, Gromov, V, and Coste, P (2000). "The Development of the" Mole with Sampling Mechanism" Subsurface Sampler". In: *Proceedings, 6th ESA Workshop on Advanced Space Technologies for Robotics and Automation (ASTRA 2000), Noordwijk, The Netherlands, December*, pp. 5–7.

Royal Museums Greenwich (n.d.). *NASA's Artemis Moon Missions: all you need to know*. URL: `https://www.rmg.co.uk/stories/topics/nasa-moon-mission-artemis-program-launch-date`.

Ruiz-Suárez, JC (2013). "Penetration of projectiles into granular targets". In: *Reports on Progress in Physics* 76.6, p. 066601.

Sherbrooke, Wade C and Nagle, Raymond B (1996). "Phrynosoma intraepidermal receptor: a dorsal intraepidermal mechanoreceptor in horned lizards (Phrynosoma; Phrynosomatidae; Reptilia)". In: *Journal of morphology* 228.2, pp. 145–154.

Sherrit, S, Bao, X, Chang, Z, Dolgin, BP, Bar-Cohen, Y, Pal, D, Kroh, J, and Peterson, T (2000). "Modeling of the ultrasonic/sonic driller/corer: USDC". In: *2000 IEEE Ultrasonics Symposium. Proceedings. An International Symposium (Cat. No. 00CH37121)*. Vol. 1. IEEE, pp. 691–694.

Sherrit, Stewart, Domm, Lukas, Bao, Xiaoqi, Bar-Cohen, Yoseph, Chang, Zensheu, and Badescu, Mircea (2012). "Single piezo-actuator rotary-hammering (SPaRH) drill". In: *Sensors and Smart Structures Technologies for Civil, Mechanical, and Aerospace Systems 2012*. Vol. 8345. International Society for Optics and Photonics, 83452B.

Shiraishi, Hiroaki, Tanaka, Satoshi, Fujimura, Akio, and Hayakawa, Hajime (2008). "The present status of the Japanese Penetrator Mission: LUNAR-A". In: *Advances in Space Research* 42.2, pp. 386–393.

Simons, Tom AH, Weiler, Rouven, Strege, Stefan, Bensmann, Sven, Schilling, Martin, and Kwade, Arno (2015). "A ring shear tester as calibration experiment for DEM simulations in agitated mixers–a sensitivity study". In: *Procedia engineering* 102, pp. 741–748.

Slaughter, William S (2012). *The linearized theory of elasticity*. Springer Science & Business Media.

Slyuta, Evgeny (2021). "The Luna program". In: *Sample return missions*. Elsevier, pp. 37–78.

Spohn, Tilman, Grott, M, Knollenberg, J, Zoest, Tim van, Kargl, G, Smrekar, SE, Banerdt, WB, and Hudson, TL (2012). "InSight: measuring the martian heat flow using the heat flow and physical properties package (HP3)". In: *International Workshop on Instrumentation for Planetary Missions*. Vol. 1683, p. 1124.

Spohn, Tilman, Hudson, Troy L, Marteau, Eloïse, Golombek, Matthew, Grott, Matthias, Wippermann, Torben, Ali, Khaled S, Schmelzbach, Cédric, Kedar, Sharon, Hurst, Kenneth, et al. (2022). "The InSight HP3 penetrator (Mole) on Mars: Soil properties derived from the penetration attempts and related activities". In: *Space Science Reviews* 218.8, p. 72.

Stoker, Carol R, Glass, Brian J, Stucky, Thomas R, Dave, Arwen I, Kobayashi, Linda T, Quinn, Richard C, Moreno-Paz, Mercedes, Sánchez-García, Laura, Mora, Maria F, Kehl, Florian, et al. (2023). "A mission simulating the search for life on Mars with automated drilling, sample handling, and life detection instruments performed in the hyperarid core of the Atacama Desert, Chile". In: *Astrobiology* 23.12, pp. 1284–1302.

Stoker, CR, Gonzales, A, and Zavaleta, JR (2007). "Moon/Mars underground mole". In: *Proc. 2007 NASA Science Technology Conf*. Vol. 6, pp. 1–7.

Stronge, William James (2018). *Impact mechanics*. Cambridge university press.

Tadami, Naoaki, Nagai, Mamoru, Nakatake, Toyoharu, Fujiwara, A, Yamada, Yasuyuki, Nakamura, Taro, Yoshida, Hiroshi, Sawada, Hirotaka, and Kubota, Takashi (2017). "Curved excavation by a sub-seafloor excavation robot". In: *2017 IEEE/RSJ International Conference on Intelligent Robots and Systems (IROS)*. IEEE, pp. 4950–4956.

Turtle, EP, Pierazzo, E, Collins, GS, Osinski, GR, Melosh, HJ, Morgan, JV, and Reimold, WU (2005). "Impact structures: What does crater diameter mean". In: *Large meteorite impacts III* 384, pp. 1–24.

Vago, Jorge L, Westall, Frances, Coates, Andrew J, Jaumann, Ralf, Korablev, Oleg, Ciarletti, Valérie, Mitrofanov, Igor, Josset, Jean-Luc, De Sanctis, Maria Cristina, Bibring, Jean-Pierre, et al. (2017). "Habitability on early Mars and the search for biosignatures with the ExoMars Rover". In: *Astrobiology* 17.6-7, pp. 471–510.

Wang, Tongzhao, Li, Xuan, Quan, Qiquan, Harkness, Patrick, and Deng, Zongquan (2024). "Passive Versus Active Control of Weight-on-Bit for an Ultrasonic Percussive Drill". In: *IEEE/ASME Transactions on Mechatronics*.

Wang, Yinchao, Quan, Qiquan, Yu, Hongying, Bai, Deen, Li, He, and Deng, Zongquan (2018). "Rotary-percussive ultrasonic drill: An effective subsurface penetrating tool for minor planet exploration". In: *IEEE Access* 6, pp. 37796–37806.

Warren, Thomas L and Forrestal, Michael J (1998). "Effects of strain hardening and strain-rate sensitivity on the penetration of aluminum targets with spherical-nosed rods". In: *International journal of solids and structures* 35.28-29, pp. 3737–3753.

Warren, Thomas L and Tabbara, Mazen R (1997). *Spherical cavity-expansion forcing function in PRONTO 3D for application to penetration problems*. Tech. rep. Sandia National Labs., Albuquerque, NM (United States).

Warren, Thomas L and Tabbara, Mazen R (2000). "Simulations of the penetration of 6061-T6511 aluminum targets by spherical-nosed VAR 4340 steel projectiles". In: *International journal of solids and structures* 37.32, pp. 4419–4435.

Wikipedia contributors (2021). *Heat Flow and Physical Properties Package — Wikipedia, The Free Encyclopedia*. [Online; accessed 25-May-2021]. URL: https://en.wikipedia.org/w/index.php?title=Heat_Flow_and_Physical_Properties_Package&oldid=1021526870.

Wikipedia contributors (2022). *Mars 2020 - Wikipedia*. URL: https://en.wikipedia.org/wiki/Mars_2020.

Wikipedia contributors (2023a). *Beagle 2 — Wikipedia, The Free Encyclopedia*. [Online; accessed 7-January-2024]. URL: https://en.wikipedia.org/w/index.php?title=Beagle_2&oldid=1189135517.

Wikipedia contributors (2023b). *MoonLITE*. [Online; accessed 2-August-2024]. URL: https://en.wikipedia.org/wiki/MoonLITE.

Wikipedia contributors (2024). *Rosalind Franklin (rover) — Wikipedia, The Free Encyclopedia*. https://en.wikipedia.org/w/index.php?title=Rosalind_Franklin_(rover)&oldid=1197889752. [Online; accessed 24-January-2024].

William, Sheehan and Jim, Bell (2021). *A Phoenix Rises from the Ashes: A look back at one of Tucson's most astonishing space missions in an excerpt from the upcoming book 'Discovering Mars'*. [Online; accessed 14-January-2024]. URL: https://www.jpl.nasa.gov/missions/phoenix.

Williams, J-P, Paige, DA, Greenhagen, BT, and Sefton-Nash, E (2017). "The global surface temperatures of the Moon as measured by the Diviner Lunar Radiometer Experiment". In: *Icarus* 283, pp. 300–325.

Wippermann, Torben, Hudson, Troy L, Spohn, Tilman, Witte, Lars, Scharringhausen, Marco, Tsakyridis, G, Fittock, Mark, Krömer, Olaf, Hense, Simon, Grott, Matthias, et al. (2020). "Penetration and performance testing of the HP^3 Mole for the InSight Mars mission". In: *Planetary and Space Science* 181, p. 104780.

Yong, PANG, ZHANG, Tao, Hongyu, WEI, Ting, ZENG, ZHANG, Yinliang, Guidong, MO, Kun, XU, Shen, YIN, Guoxin, WANG, ZHANG, Xingwang, et al. (2023). "Influence of lunar regolith compressibility on sampling performance of thick wall spiral drills". In: *Chinese Journal of Aeronautics* 36.2, pp. 350–362.

Young, CW (1997). *Penetration equations*. Tech. rep. Sandia National Labs., Albuquerque, NM (United States).

Yu, Hai-Sui (2000). *Cavity expansion methods in geomechanics*. Springer Science & Business Media.

Yu, HS and Houlsby, GT (1991). "Finite cavity expansion in dilatant soils: loading analysis". In: *Geotechnique* 41.2, pp. 173–183.

Zacny, K, Bar-Cohen, Y, Brennan, M, Briggs, G, Cooper, G, Davis, K, Dolgin, B, Glaser, D, Glass, B, Gorevan, S, et al. (2008). "Drilling systems for extraterrestrial subsurface exploration". In: *Astrobiology* 8.3, pp. 665–706.

Zacny, Kris (2012). "Lunar drilling, excavation and mining in support of science, exploration, construction, and in situ resource utilization (ISRU)". In: *Moon: Prospective Energy and Material Resources*. Springer, pp. 235–265.

Zhang, Weiwei, Li, Lifang, Jiang, Shengyuan, Ji, Jie, and Deng, Zongquan (2019). "Inchworm drilling system for planetary subsurface exploration". In: *IEEE/ASME Transactions on Mechatronics* 25.2, pp. 837–847.

Zhang, Yinliang, Zhang, Tao, Wei, Hongyu, Liu, Jiabin, Wang, Wei, Yuan, Xinyue, Pang, Yong, Guan, Yisheng, Hou, Xuyan, and Xu, Kun (2022). "Advances in extraterrestrial drilling technology to discover the secrets hidden inside celestial bodies". In: *Space Science Reviews* 218.6, p. 47.

Zukas, Jonas (2004). *Introduction to hydrocodes*. Elsevier.

Appendix A

probe-coupling-actuators configuration used in Chapter 4

Figure A.1 shows the detail drawing of hex probe-coupling-actuators configuration.

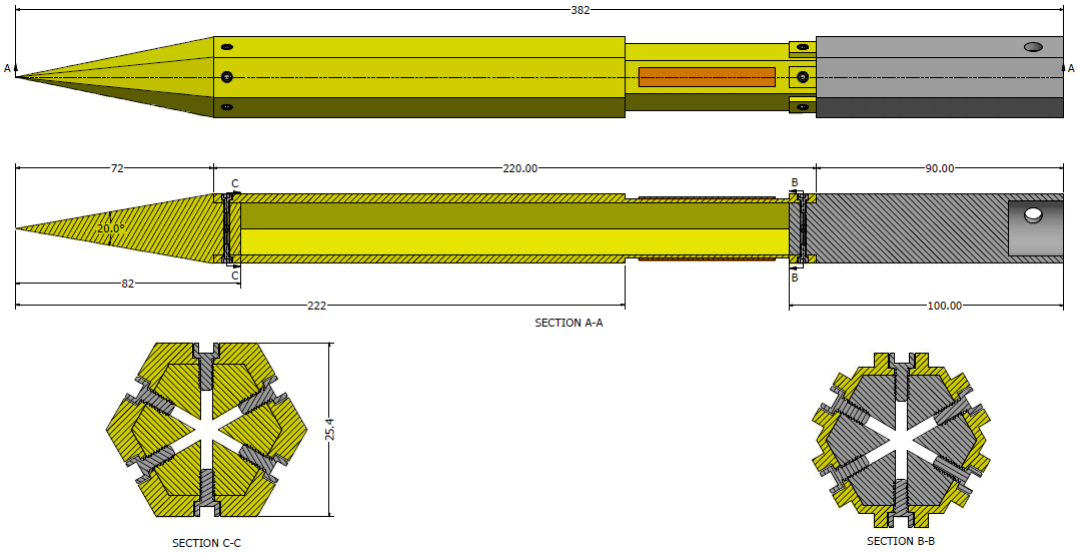

FIGURE A.1: Hex probe detail drawing (all dimensions are in mm)

Appendix B

probe-coupling-actuators configuration used in Chapter 5

Figure B.1 shows the detail drawing of circular probe-coupling-actuators configuration.

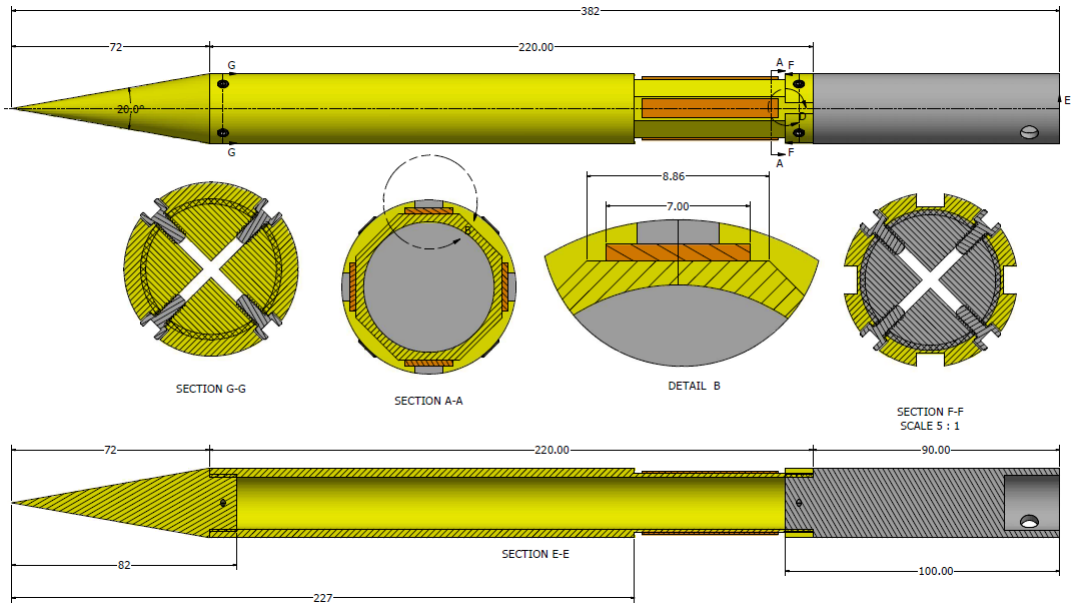

FIGURE B.1: Circular probe detail drawing (all dimensions are in mm)